Mechanism of receptor assembly via the pleiotropic adipokine Leptin

Alexandra Tsirigotaki[1,2], Ann Dansercoer[1,2], Koen H.G. Verschueren[1,2], Iva Marković[1,2], Christoph Pollmann[3], Maximillian Hafer[3], Jan Felix[1,2], Catherine Birck[4], Wouter Van Putte[5], Dominiek Catteeuw[6,7,#], Jan Tavernier[6,7,‡], J. Fernando Bazan[2,8], Jacob Piehler[3], Savvas N. Savvides[1,2*] & Kenneth Verstraete[1,2*]

[1] Unit for Structural Biology, Department of Biochemistry and Microbiology, Ghent University, Ghent, Belgium.
[2] Unit for Structural Biology, VIB-UGent Center for Inflammation Research, Ghent, Belgium.
[3] Department of Biology/Chemistry and Center of Cellular Nanoanalytics, Osnabrück University, Osnabrück, Germany.
[4] Integrated Structural Biology Platform, Centre for Integrative Biology (CBI), Institut de Génétique et de Biologie Moléculaire et Cellulaire (IGBMC), CNRS UMR 7104, INSERM U1258, University of Strasbourg, Illkirch, France.
[5] PUXANO, PXN BioLabs. BlueChem Incubator, Antwerp, Belgium.
[6] VIB-UGent Center for Medical Biotechnology, Ghent, Belgium.
[7] Department of Biomolecular Medicine, Ghent University, Ghent, Belgium.
[8] ħ Bioconsulting llc, Stillwater, MN, USA.
[#] Current address: Department of Biochemistry and Microbiology, Ghent University, Ghent, Belgium.
[‡] Current address: Orionis Biosciences, Ghent, Belgium.
* Corresponding authors: e-mail to savvas.savvides@ugent.be, kenneth.verstraete@ugent.be.

Abstract

The adipokine Leptin activates its receptor LEP-R in the hypothalamus to regulate body weight and exerts additional pleiotropic functions in immunity, fertility, and cancer. However, the structure and mechanism of Leptin-mediated LEP-R assemblies has remained unclear. Intriguingly, the signaling-competent isoform of LEP-R is only lowly abundant amid several inactive short LEP-R isoforms contributing to a mechanistic conundrum. Here, we show by X-ray crystallography and cryo-EM that Leptin induces unprecedented type I cytokine receptor assemblies featuring 3:3 stoichiometry and demonstrate such Leptin-induced trimerization of LEP-R on living cells via single molecule microscopy. In mediating these assemblies, Leptin undergoes drastic restructuring that activates its site III for binding to the Ig-domain of an adjacent LEP-R. These interactions are abolished by mutations linked to obesity. Collectively, our study provides the structural and mechanistic framework for how the 3:3 stoichiometry of the evolutionarily conserved Leptin:LEP-R complex might support signaling-competent complexes comprising distinct LEP-R isoforms.

Main

Introduction

Leptin, a four-helix-bundle hormone[1], activates LEP-R, a member of the gp130 family, to relay signals about energy deposit levels in the white adipose tissue to the hypothalamus and assumes pleiotropic roles in immunity, fertility, and cancer[2-4]. Dysregulation of Leptin-mediated STAT-3 signaling via the long LEP-R isoform is linked to obesity[5,6].

LEP-R stands out among the many gp130 family cytokine receptors in two main ways. Firstly, it displays six isoforms[7,8] with drastically differing activity profiles. Secondly, all six

isoforms share a common, highly glycosylated[9] extracellular domain (ECD) that displays a unique combination of structural domains. At its N-terminus LEP-R_{ECD} features an cytokine-receptor homology (CRH) 1 module (LEP-R_{CRH1}) with an N-terminal extension (NTD), followed by an Immunoglobulin-like domain (LEP-R_{Ig}), which is essential for Leptin-induced receptor oligomerization, and a CRH2 module (LEP-R_{CRH2}) responsible for high-affinity Leptin binding[10-12]. At its C-terminus the ectodomain carries two Fibronectin III-like (FnIII) domains (LEP-R_{FNIII}) proximal to the cell membrane (**Fig. 1a**) that are critical for LEP-R-mediated STAT signaling[13].

Intriguingly, whereas leptin-mediated activation of LEP-R transduces signaling via Janus kinase/Signal Transducer and Activator of Transcription (JAK/STAT), only the longest of six LEP-R isoforms, LEP-Rb (**Fig. 1a**) is signaling-competent[7,8]. LEP-Rb is specifically expressed in the brain hypothalamus and mediates Leptin-dependent STAT-3 signaling[13] to balance energy expenditure and food intake. Short LEP-R isoforms (LEP-Ra,c,d,f) carrying a truncated intracellular region beyond the box 1 motif are widely expressed but STAT-3 signaling deficient[8]. Such LEP-R isoforms may facilitate the transport of Leptin across the blood-brain barrier[14] or provide a source for soluble LEP-R via ectodomain shedding[15]. The co-existence of signaling competent and signaling-deficient or inactive LEP-R isoforms all featuring common leptin-binding LEP-R_{ECD} has created a mechanistic conundrum that has been challenging to resolve considering the prevailing models of cytokine-mediated receptor activation within the gp130 family of receptors.

A plethora of mutagenesis data over the last two decades had led to a molecular mechanism whereby Leptin employs two distinct functional sites, termed sites II and III, to establish LEP-R signaling complexes at the cell surface[2]. Furthermore, the receptor signaling assembly mediated by Leptin has been proposed to adopt a 2:2 stoichiometry, in line with the generally accepted dimeric mode of JAK activation[16,17], and based on structural paradigms derived from the related G-CSF assembly and structural models obtained from negative-stain electron microscopy (EM)[18] and Small-angle X-ray Scattering (SAXS)[11]. However, functional complementation of LEP-R variants deficient in JAK2-binding and phosphorylation indicates that Leptin:LEP-R signaling assemblies may contain more than two LEP-R chains[10] which prompted a proposal for a 2:4 Leptin:LEP-R assembly[12]. Furthermore, minimal signaling repression of LEP-Rb by LEP-Ra[19] and evidence of heteromeric complexes comprising LEP-Rb and LEP-Ra at the cell surface[20] suggest that Leptin-driven LEP-R complexes do not need to comprise exclusively the signaling-competent LEP-Rb isoform.

We here present the structural and mechanistic basis for the assembly of Leptin-mediated LEP-R signaling complexes revealing an unprecedented assembly displaying 3:3 stoichiometry. Together with a range of complementary studies that include single-molecule microscopy, our surprising structural findings provide the long-sought framework for further interrogation of Leptin-mediated signaling in physiology and disease, including how the lowly abundant signaling-competent isoforms of LEP-R can productively participate in signaling assemblies amid several highly abundant inactive LEP-R isoforms. Thus, our study provides a possible solution to the mechanistic conundrum underlying Leptin-mediated activation of LEP-R.

Results

Structural basis of high-affinity binding of Leptin to LEP-R

To provide a structural snapshot of the Leptin:LEP-R encounter complex via site II, we focused on complexes of Leptin with the LEP-R_{CRH2} fragment required for high-affinity binding with Leptin[21,22] (**Extended Data Fig. 1a-c**). Ensuing crystal structures for glycan-trimmed mouse (m) and human (h) Leptin:LEP-R_{CRH2} complexes (**Extended Data Fig. 1a, Table 1**) at 1.95 Å and 3.69 Å resolution, respectively, demonstrate that mouse and human complexes are similar (**Extended Data Fig. 1a**; root mean square deviation (r.m.s.d.) = 0.39Å, 161 Cα atoms), consistent with their high sequence identity (85%) (**Supplementary Fig. 1a**). Leptin utilizes αA and αC helices to bind the LEP-R_{CRH2} loop regions near the hinge of the CRH2 module (**Fig. 1b-c**), reminiscent of the site II interaction for homologous cytokines[2]. Notably, the loops connecting the αA-αB and αC-αD helices of both human and mouse Leptin are not resolved, in agreement with their dynamic nature in solution[23].

The crystal structure for the mLeptin:mLEP-R_{CRH2} assembly provides a detailed description of the interface responsible for high-affinity binding. LEP-R_{CRH2} and Leptin employ evolutionarily conserved residues to interact (**Supplementary Fig. 1b**) via hydrogen bonds and van der Waals contacts that bury approximately 1,600 $Å^2$ of surface area (**Fig. 1b-c, Supplementary Fig. 2**). This interface is highly hydrated with six water molecules directly bridging Leptin and LEP-R (**Fig. 1b-c, Supplementary Fig. 2**).

Most binding interactions are contributed by the first subdomain of LEP-R_{CRH2} while the hinge and second subdomain of LEP-R_{CRH2} interact exclusively with αA of Leptin (**Fig. 1b, Supplementary Fig. 2**). At the heart of the interface, mLEP-R residues Leu469, Tyr470, Leu503 and Leu504 harbor at the hydrophobic junction of α-helices A-C of mLeptin (residues Val27, Leu34, Leu107, Leu110) (**Fig. 1b**). Below the hydrophobic junction, hydrogen bonding dominates the interface, primarily via LEP-R_{CRH2} main chain – Leptin side chain contacts and/or bridging water molecules (**Fig. 1c, Supplementary Fig. 2**). mLeptin residues Arg41, Gln96 and Asn103 act as hydrogen bond hubs, with each participating in at least three different hydrogen bonds (**Fig. 1c, Supplementary Fig. 2**). The complex is further stabilized by a salt bridge between Glu102 of mLeptin and Arg466 of mLEP-R.

This observed site II corroborates previous structure-function studies of the Leptin:receptor interaction site II[21,22,24-26]. In particular, mutations towards reduced affinity (mLeptin residues Asp30, Thr33, Lys36, Thr37, Arg41, Gln96, Asn103, Asp106, Leu107)[22], and impaired signaling (mLeptin residues Arg41, Gln96 and Leu107; mLEP-R_{CRH2} residues 501-504)[21,22,25], all map at the resolved site II interface (**Supplementary Fig. 2**).

Leptin nucleates 3:3 assemblies with LEP-R_{IgCRH2}

Leptin-dependent oligomerization of LEP-R via the Ig domain of LEP-R is required for singaling[10]. To provide structural insights into this process, we initially focused on Leptin:LEP-R_{IgCRH2} complexes (**Extended Data Fig. 1d-g)**.

Minimally glycosylated Leptin:LEP-R_{IgCRH2} complexes were prepared for crystallographic studies and diffraction quality crystals were obtained for mLeptin:mLEP-R_{IgCRH2} (**Table 1**). The crystallographic asymmetric unit of the resulting structure to 2.9 Å resolution in trigonal space group *H*32 contains one copy of the mLeptin:mLEP-R_{IgCRH2}

complex that recapitulates the high-affinity complex seen in the mLeptin:mLEP-R_{CRH2} crystal structure (r.m.s.d. = 0.4 Å for 252 aligned Cα atoms), with the mLEP-R_{Ig} domain emanating away from the LEP-R_{CRH2} module (**Extended Data Fig. 1d**). Application of the three-fold crystallographic symmetry generates a closed, ring-like Leptin:LEP-R_{IgCRH2} assembly with an unprecedented 3:3 stoichiometry (**Fig. 1d-e)** in the Type 1 cytokine receptor family[27]. In this assembly, the LEP-R_{CRH2}-bound Leptin exposes its site III epitope to bind the LEP-R_{Ig} domain from an adjacent Leptin:LEP-R_{IgCRH2} complex leading to a cross-over complex with 3-fold symmetry (C3).

LEP-R_{Ig} adopts a distinct orientation relative to LEP-R_{CRH2}, as compared to the IL-6Rβ and GCSF receptor homologues (**Extended Data Fig. 2a**). This distinct geometry is characterized by a short linker at the LEP-$R_{Ig\text{-}CRH2}$ boundary and stabilized by hydrophobic interactions between the Ig and CRH2 regions (**Extended Data Fig. 1d).** The LEP-R_{IgCRH2} fragment, as well as the Leptin:LEP-R_{CRH2} and Leptin:LEP-R_{Ig} interaction modes agree well with structural models predicted by AlphaFold[28], indicating that the experimentally determined assembly is supported by co-evolutionary relationships across the respective protein interfaces (**Extended Data Fig. 2c-f**).

Notably, in the crystal two 3:3 Leptin:LEP-R_{IgCRH2} complexes are packed in a head-to-head orientation via reciprocal hydrophobic contacts of juxtaposing LEP-R_{Ig} domains (**Extended Data Fig. 1e**). This head-to-head self-association is artifactual in nature, as the presence of the N-terminal LEP-$R_{NTD\text{-}CRH1}$ domains upstream of LEP-R_{Ig} would abolish these reciprocal LEP-R_{Ig} contacts. Corroborating this, in the absence of the N-terminal LEP-R domains, this head-to-head interface also stabilizes non-covalent Leptin:LEP-R_{IgCRH2} complexes in solution in an apparent 6:6 stoichiometry (**Extended Data Fig. 1f-g**), and these are reduced to 3:3 assemblies in the context of full-length mLEP-R_{ECD} (**Extended Data Fig. 3)**.

In an analogous fashion, we found that truncated hLeptin:hLEP-R_{IgCRH2} complexes form 6:6 assemblies in solution that are site III-dependent as the hLeptin variant that carries the ^{141}ST^{142}/AA (Leptin$_{a1}$) mutations[22] was unable to form such complexes (**Extended Data Fig. 1f**).

Leptin's plasticity enables site III binding

Leptin binds the Ig-domain of LEP-R via a composite binding interface (**Fig. 1f-g)** that buries 1,600 Å^2 of solvent accessible surface area.

The N-terminal tip of α-helix D which gains an extra turn upon binding LEP-R_{Ig} contains the highly conserved and functionally important residue Tyr140 (**Fig. 1f-g, Supplementary Fig. 1b**). Aromatic residues at this position comprise a blueprint of cytokine:Ig interactions in the gp130 family (**Extended Data Fig. 2b**). LEP-R_{Ig} accommodates Tyr140 in the heart of a surface cavity decorated with aromatic mLEP-R residues Phe403, Tyr405, Tyr409 and Tyr420 (**Fig. 1g)**. In addition, the hydroxyl group of Ser141 at Leptin's tip of α-helix D forms strong hydrogen bonds with the hydroxyl group of mLEP-R-Tyr409 and carbonyl group of mLEP-R-His418, all ubiquitously conserved and important in signaling[12,22]. This provides a structural rationale for the antagonistic ^{141}ST^{142}/AA (Leptin$_{a1}$) variant[22] that carries mutations at the tip of α-helix D. Another signaling crucial residue, mLEP-R-Leu370

(ref. [12]), packs against Val144-Val145 in α-helix D and Val51 and Val57 of the A-B loop of Leptin forming a hydrophobic network (**Fig. 1h**).

Leptin's A-B loop becomes ordered in the LEP-R_{Ig}-bound state (**Fig. 1b,d**, **Fig. 2**) and contributes 53% of Leptin's site III interface area. It seals the interface by lining most of the rim of the LEP-R_{Ig} cavity, engaging in van der Waals contacts and hydrogen bonds (**Fig. 1f,h, Supplementary Fig. 2f**). Part of Leptin's C-D loop rearranges into an amphipathic two-turn α-helix, referred to as α-helix E (ref [1]) that interacts with the β8 – β9 loop of LEP-R_{Ig} through van der Waals contacts and a hydrogen bond between mLeptin-Ser138 and mLEP-R-His418 (**Fig. 1f,g**).

A surface-exposed αB-αD hydrophobic hub (**Fig. 2a-b**) becomes occupied by the A-B loop via residues Val57, Leu60, Phe62, Ile63, Ile69 (**Fig. 2c**) in the Ig-bound state. This creates an extensive network of hydrophobic interactions that also stabilizes αE via residues Leu131 and Val134. Here, residues Phe62 and Ile63 are critical for bridging the A-B loop, the four-helix bundle core and αE (**Fig. 2C**), thereby stabilizing the composite site III interface on Leptin. This is reflected in the antagonistic properties of a previously reported ^{62}FI^{63}/AA Leptin variant[29], that we now show can be attributed to compromising the binding conformation of site III to mediate the Leptin:LEP-R interaction interface.

Collectively, the drastic restructuring of Leptin's flexible A-B and C-D loops to enable LEP-R_{Ig} binding via site III is expected to be associated with an entropic penalty. This entropic cost might be compensated in part by the transient formation of α-helix E in the unbound state, and by the transient anchoring of the loops onto the hydrophobic hub formed by α-helices B-D[23], similarly to the crystallographic packing of hLeptin in the unbound state (**Fig. 2a**)[1].

Site III drives 3:3 Leptin:LEP-R_{ECD} complexes and signaling

To investigate the stoichiometry of complexes of Leptin and variants thereof in complex with full-length LEP-R_{ECD}, we employed SEC-MALLS and analytical ultracentrifugation (AUC) sedimentation velocity experiments (**Fig. 3a-c, Extended Data Fig. 3**). The biological activity of Leptin variants was interrogated in a STAT3 responsive luciferase reporter assay in HEK293T cells (**Fig. 3d**).

To facilitate the molecular mass determination of Leptin:LEP-R_{ECD} complexes via SEC-MALLS and AUC we initially worked with glycan-trimmed mLEP-R_{ECD}. We found that glycan-trimmed mLEP-R_{ECD} is monomeric in solution (**Fig. 3a-b**, c(s) ~ 4.4 S consistent with monomer) and forms 3:3 complexes with mLeptin (**Fig. 3a-b,** c(s) ~ 10.11 S consistent with 3:3 complex), in a reversible and concentration-dependent manner (**Extended Data Fig. 3a, Fig. 3c).** From hydrodynamic scale relationships in AUC, minor peaks detected in the range of s-values ~ 6 – 8 S are consistent with dimeric species or higher oligomeric species that can dissociate and re-associate during the sedimentation process. The 1:1 to 3:3 mLeptin:mLEP-R_{ECD} transition is of low affinity in solution (K_D = 0.76 - 1.2 μM; **Fig. 3c**) and independent of the membrane proximal FNIII domains (**Extended Data Fig. 3c**). The formation of 3:3 complexes in solution and at the cell surface is site III-dependent as $Leptin_{a1/a2}$ antagonists (^{141}ST^{142}/AA and ^{60}LDFI^{63}/AAAA respectively) bind to the receptor with a 1:1 stoichiometry but are impaired towards forming higher-order oligomers (**Fig. 3a-b,** c(s) ~ 4.9 S consistent with 1:1 complex) and receptor activation (**Fig. 3d**). In addition, mLEP-R_{ECD} bearing the

pathogenic A407E mutation at site III remains largely monomeric upon Leptin addition (**Extended Data Fig. 3b**). In contrast, mutating a previously proposed LEP-R binding site on Leptin[12], termed 'Site I', located in the C-terminal region of α-helix D does not disturb the 3:3 assembly and this mutant also remains signaling competent (**Fig. 3a,d**).

We also interrogated complex formation of glycosylated mLEP-R_{ECD} in solution using SEC-MALLS and found that the mLEP-R_{ECD} oligomerizes in a Leptin-dependent manner at similar concentrations as its glycan-trimmed counterpart, albeit with a lower - approximately 2:2 - apparent stoichiometry (**Extended Data Fig. 3d**). In contrast, glycosylation of the mLEP-$R_{ECD\text{-}\Delta FNIII}$ segment has no effect on the oligomerization towards a 3:3 mLeptin:mLEP-$R_{ECD\text{-}\Delta FNIII}$ complex in solution (**Extended Data Fig. 3c,e**). These data suggest that glycosylation at the membrane-proximal LEP-R_{FNIII} domains – which carries 5 potential N-linked glycosylation sites – may destabilize the 3:3 mLeptin:mLEP-R_{ECD} complex in solution, possibly via steric hindrance.

We were unable to demonstrate the formation of higher-order hLeptin:hLEP-R_{ECD} complexes with glycosylated hLEP-R_{ECD} in solution as only 1:1 hLeptin:hLEP-R_{ECD} complexes are observed via SEC-MALLS (**Extended Data Fig. 3f**). Glycan-trimmed hLEP-R_{ECD} precipitates upon Leptin addition, preventing further analysis. Strikingly, although we found that hLeptin does not support stable clustering in solution with hLEP-R_{ECD} and mLEP-R_{ECD}, mLeptin does form 3:3 complexes in solution with glycosylated hLEP-R_{ECD} (**Extended Data Fig. 3g-h**). Ensuing efforts to "murinize" hLeptin proved unsuccessful (**Extended Data Fig. 3i**). Nevertheless, hLeptin induces site III-dependent receptor activation in cells with similar EC_{50} values as mLeptin, and hLeptin and mLeptin exhibit full species cross-reactivity (**Fig. 3d, Extended Data Fig. 3k**). Moreover, site III-dependent activation via Leptin appears significantly more efficient than activation by an agonistic anti-hLEP-R_{ECD} antibody[30] that dimerizes the hLEP-R in a Leptin-independent fashion (**Extended Data Fig. 3j,k**).

Collectively, these studies show that 3:3 Leptin:LEP-R_{ECD} complexes in solution and signaling complexes are driven by the same interaction interfaces as in the crystallographically distilled 3:3 assembly. Site III-dependent 3:3 complexes in solution form with an affinity in the low micromolar range. At the membrane, the clustering of 1:1 Leptin:LEP-R complexes towards transmembrane higher-order signaling assemblies is expected to be facilitated by the reduced dimensionality of the membrane, as well as by possible additional contacts with the membrane, and interactions between the TM-helices and intracellular regions of adjacent LEP-R chains.

Structure of the complete Leptin:LEP-R_{ECD} assembly

To obtain additional structural and mechanistic insights, the glycosylated Leptin:LEP-R_{ECD} assembly was characterized using single-particle cryo-EM analysis. Dilution of a concentrated mLeptin:mLEP-R_{ECD} complex sample just prior to cryo-EM grid preparation revealed distinct oligomeric states demonstrating that mLeptin:mLEP-R_{ECD} can assemble into complexes of up to 3:3 stoichiometry (**Fig. 4a**, **Extended Data Fig. 4a**). All three observed states appeared to populate preferred orientations, preventing high-resolution 3D reconstruction. Anisotropic, cryo-EM reconstruction applied to an apparent intermediate complex ($FSC_{0.143}$ resolution = 4.43 Å) revealed an open assembly in which mLeptin bridges two mLEP-R_{ECD} chains via sites

II and III to elicit contacts between the membrane-proximal LEP-R_{FNIII} domains (**Fig. 4b, Extended Data Fig. 4b, Table 2**). The architecture of this intermediate assembly is compatible with a transition towards a closed 3:3 complex. Notably, the cryo-EM map of this complex lacks evidence for a second Leptin molecule at the CRH2' site which may be linked to the apparent increased structural heterogeneity in this region and/or partial complex dissociation under these experimental conditions.

To facilitate cryo-EM analysis of the 3:3 mLeptin:mLEP-R_{ECD} complex, a trimerizing GCN4 isoleucine-zipper motif[31,32] (tGCN4) was fused to the C-terminus of mLEP-R_{ECD} (**Extended Data Fig. 5a**). Non-stabilized glycan-trimmed mLeptin:mLEP-R_{ECD} complexes are structurally similar to the tGCN4-stabilized assembly in solution as probed by SAXS (**Extended Data Fig. 5b**), confirming that the tGCN4-fusion stabilizes spontaneously formed complexes.

Reconstructions in C1 symmetry to an $FSC_{0.143}$ resolution of 4.60 Å for the glycosylated mLeptin:mLEP-$R_{ECD\text{-}tGCN4}$ complex (**Extended Data Fig. 5c**) show an extended, pseudo-C3-symmetric assembly in which three Leptin:LEP-R_{ECD} complexes interact via site III mediated interfaces as seen in the 3:3 Leptin:LEP-R_{IgCRH2} crystal structure (**Fig. 5a-c, Extended Data Fig. 6a,b**). To resolve this pseudo C3-symmetric assembly at higher resolution, we applied symmetry expansion in combination with local refinement. This approach drastically improved the map quality ($FSC_{0.143}$ = 4.02 Å, **Fig. 5d,e and Extended Data Fig. 5d**) and demonstrates that CRH2:Leptin:Ig' subcomplexes form well-defined structural units within the ring-like core region of the complex.

The N-terminal LEP-R_{CRH1} domains appear as largely disordered. The membrane-proximal regions of the adjacent mLEP-R chains arrange in a non-symmetric manner whereby two receptor legs interact via the tips of their LEP-R_{FnIII} modules, and with the LEP-R_{FnIII} module of the 3rd receptor leg being less defined (**Fig. 5a,b, Extended Data Fig. 6c**). The LEP-R_{FnIII} modules adopt a bent and compact conformation as seen in gp130[33] and in our crystal structure for mLEP-R_{FnIII} in complex with the anti-mLEP-R nanobody VHH-4.80 at 1.75 Å resolution (**Table 1, Extended Data Fig. 7a**).

Cryo-EM analysis of the corresponding hLeptin:hLEP-$R_{ECD\text{-}tGCN4}$ complex (**Extended Data Fig. 8**) results in a reconstruction to an $FSC_{0.143}$ resolution of 5.62 Å that shows two hLeptin:hLEP-R_{ECD} subcomplexes forming a site III-mediated assembly as seen for the mLeptin:mLEP-$R_{ECD\text{-}tGCN4}$ complex, while the density for a third Leptin:LEP-R subunit is not well-defined indicating structural heterogeneity (**Fig. 5f, Extended Data Fig. 6d,e**). Ensuing subclassification shows that the third hLeptin:LEP-R_{ECD} subcomplex can adopt two conformations towards closed and open trimeric assemblies (**Fig. 5g, Extended Data Fig. 8b**). This observation may be linked to the apparent weaker site III interaction for the human compared to the mouse complex.

In conclusion, our cryo-EM analysis establishes that both mouse and human Leptin have the potential to oligomerize LEP-R via the crystallographically observed site II and site III interactions to elicit contacts between the membrane-proximal LEP-R_{FnIII} modules. The orientation of the membrane-proximal LEP-R_{FnIII} modules – which are required for LEP-Rb-mediated signaling[13] - is likely also restrained by a disulfide bridge between mLEP-R residues Cys602 and Cys672 across the CRH2 and FnIII interface (**Extended Data Fig. 7b**). We note that the structural plasticity observed in our cryo-EM samples might be exaggerated compared

to the corresponding transmembrane complexes, as these would be expected to be further restrained by anchorage to the transmembrane helices and possible interactions between the LEP-R_{FnIII} modules and the outer plasma membrane region. It remains to be seen whether this plasticity is mechanistically linked to JAK/STAT activation.

The conformation of LEP-R_{ECD} as observed in the cryo-EM map corresponds remarkably well to a predicted structural model via AlphaFold (**Extended Data Fig. 6f**). Given the close similarity of human and mouse Leptin:LEP-R hexameric assemblies, we sought to assess the possible evolutionary persistence of such assembly modes by employing AlphaFold-Multimer[34,35] to predict 3:3 complexes for a series of Leptin:LEP-R complexes in jawed vertebrates where cognate 4-helix bundle cytokines and their receptors can be detected[36]. The corresponding 3:3 Leptin:LEP-R_{IgCRH2} model complexes strongly converge on hexameric solutions that closely superpose with the 3:3 mLeptin:mLEP-R_{IgCRH2} crystallographic assembly (**Extended Data Fig. 2g**). This suggests that the ability of Leptin to nucleate complexes with LEP-R_{ECD} with 3:3 stoichiometry can be traced to the earliest Leptin signaling systems in jawed vertebrates.

Leptin induces LEP-R trimerization at the cell surface

Recent experimental advances in multicolor single-molecule imaging have enabled to quantify receptor stoichiometries of signaling complexes in the plasma membrane of live cells[37]. These techniques revealed that the subunits of type I/II cytokine receptors are monomeric in the resting state and associate into well-defined dimeric or tetrameric signaling complexes largely matching the complexes observed in *vitro*[37-41]. Given the 3:3 Leptin-LEP-R stoichiometry that we consistently identified in *vitro*, we sought to investigate receptor assembly in the plasma membrane of living cells. To this end, we conducted triple-color single-molecule imaging by total internal reflection fluorescence microscopy (smTIRFM)[37] using N-terminally ALFA-tagged mLEP-Ra and mLEP-Rb labelled via nanobodies in three different colors (**Fig. 6a**).

Interactions between LEP-R subunits were quantified by dual- and triple-color single molecule co-tracking as schematically depicted in **Fig. 6b,c** and **Extended Data Fig. 9a**). As expected, no co-diffusion of LEP-R was observed in the resting state, confirming receptor monomers in the absence of Leptin (**Fig. 6d-e, Extended Data Fig. 9b,c, Supplementary Movie 1**). However, upon ligand stimulation, substantial three-color (3C) co-diffusion was observed for LEP-R, but not TpoR, which we used as a control for a strictly homodimeric class I cytokine receptor [40] (**Fig. 6d,e, Extended Data Fig. 9b,c, Supplementary Movie 1**). Likewise, dimerization of LEP-R via an engineered cross-linker did not yield substantial 3C co-diffusion (**Fig. 6e**), corroborating that the higher stoichiometry of Leptin-induced LEP-R complexes is based on ligand-mediated interactions.

To interpret the observed 3C co-diffusion, we engineered a constitutively trimerized mLEP-R variant by fusing a trimerization domain ("Foldon" from T4 fibritin) downstream of the transmembrane domain (**Supplementary Movie 2**). Compared to the maximum 3C co-diffusion observed for this construct, we observed mean levels of ~40% and 50% for mLeptin:mLEP-Ra and mLeptin:mLEP-Rb, respectively. These substantial 3C co-diffusion levels were accompanied by high dual-color (2C) co-diffusion (**Extended Data Fig. 9b**), which can be explained by a stochastic labeling within trimers (**Fig. 6c**). Importantly, 2C and 3C co-diffusion were not detectable upon stimulation with $Leptin_{a2}$, highlighting the key role

of site III for the formation of LEP-R complexes in the plasma membrane. Changes in the diffusion properties upon stimulation with Leptin, however, were rather moderate, with the decrease in the diffusion constants and the increase in the immobile fraction being similar as observed for receptor dimerization (**Extended Data Fig. 9d,e**).

In conjunction with the relatively homogeneous fluorescence intensity of Leptin-induced LEP-R oligomers (**Supplementary Movie 1**), their largely uncompromised mobility highlights the lack of higher order clustering, which would be accompanied by a strong reduction in the diffusion constant and a substantial increase of immobile molecules. By contrast, the very moderate changes in mobility are very much in line with what has been previously observed for dimerization of class I/II cytokine receptor families[37,39-43]. Rather, the co-tracking data strongly support our hypothesis that Leptin induces LEP-R trimers at the cell surface, which is also now illustrated structurally to near-atomic resolution by the plethora of structural and biophysical data we have presented. However, our observations are also in line with a mixture of LEP-R dimers and trimers at the cell surface.

Discussion

Nearly three decennia since the discovery of Leptin, we provide here the structural basis of the Leptin:LEP-R assembly towards signaling, revealing a surprising hexameric circular assembly obeying 3:3 stoichiometry. This establishes an unprecedented cytokine-driven assembly mode within the Type I cytokine receptor family that diverges from previous mechanistic proposals for the assembly of the Leptin:LEP-R complex via a closed 2:2 complex similar to the G-CSF:G-CSF-R system as inferred from structural studies at low-resolution[11,18].

The evolutionarily conserved Leptin:LEP-R assembly mechanism presented here is mediated via the conserved and functionally validated sites II and IIII that spatially couple the tips of at least two membrane-proximal LEP-R_{FNIII} domains and depends on the dramatic restructuring on Leptin's loop regions. The interaction of the LEP-R_{FNIII} domains is likely the key for triggering signaling by bringing the transmembrane helices, the intracellular region and consequently the associated JAK kinases to close proximity of each other for cross-activation[16].

The effect of several pathological single nucleotide polymorphisms (SNPs) in Leptin and LEP-R associated with severe obesity can now be discussed in light of our structural data (**Supplementary Table 1, Extended Data Fig. 7c-f**). The pathogenic LEP-R A409E (Ala407 in mouse), and Leptin S141C and V145E mutations localize at the site III interface (**Fig. 1g; Extended Data Fig. 7d**) and thereby prevent the formation of higher-order LEP-R complexes. In vitro studies on LEP-R A409E and Leptin V145E show that these mutants indeed retain site II affinity but are signaling deficient (**Supplementary Table 1)**. Two other confirmed pathogenic mutations in Leptin, D100Y and N103K, map on the site II interface (**Fig. 1c; Extended Data Fig. 7e**) and show an abolished LEP-R binding phenotype[44-46]. The C604S mutation in hLEP-R would disturb the disulfide bridge between residues Cys604 and Cys674 (**Extended Data Fig. 7b,c,f**) that likely plays a key role to project the membrane-proximal FnIII-modules in a signaling competent conformation. Thus, our structural observations corroborate pathological mutations in leptin and LEP-R and help to rationalize the antagonistic properties of leptin site III antagonists. We anticipate that these structural and mechanistic

insights might guide personal medicine approaches to treat leptin disfunction and inform the engineering of leptin variants with superior agonistic or antagonistic properties.

Corroborating our structural findings, we could confirm Leptin-induced formation of trimeric LEP-R complexes in the plasma membrane of living cells, rather than the canonical dimeric receptor assemblies. This different mode of ligand engagement as compared to the paradigmatic receptors for Epo and growth hormone probably allows a more flexible stoichiometry at the cell membrane, that may also include open 2:2 Leptin:LEP-R complexes (**Fig. 6f**). In this regard, a soluble 1:1 Leptin:LEP-R_{ECD} complex might also bind to an open Leptin:LEP-R complex with 2:2 stoichiometry at the cell surface. This may be biologically relevant as circulating leptin exists both in a free form and in complex with the soluble LEP-R ectodomain[47].

Leptin functions as a lipostat to maintain a stable body weight and LEP-R responsive hypothalamic neurons are proposed to directly sense leptin's serum concentration at the median eminence[48,49]. Interestingly, under normal phycological conditions leptin's serum concentration only varies 2 to 3-fold according to a circadian rhythm[50]. The assembly of up to three LEP-R receptors may affect leptin's dose response relationship due an increased cooperativity. Indeed, this may be crucial to tightly regulate LEP-R signaling over the narrow physiological concentration range of leptin.

In addition, considering the broad spectrum of LEP-R splice variants, the implications of such higher-order and potentially variable receptor stoichiometries for intracellular JAK kinase activation and STAT3 signaling are intriguing. As the widely expressed[8] short LEP-R isoforms share an identical extracellular Leptin-binding region with LEP-Rb, these have the potential to form Leptin-dependent heteromeric complexes with LEP-Rb (**Fig. 6f**). Such Leptin-stabilized heteromeric LEP-R complexes at the cell surface have indeed been reported and may represent a major complex species at the cell surface [20]. However, although the short LEP-R isoforms contain the box 1 motif, the functional relevance of JAK recruitment by the short LEP-R isoforms [8,14,51,52] is unclear. Notably, LEP-Ra appears to show weak JAK2 binding and phosphorylation capacity[53], dependent on Box1. LEP-Ra was however shown incapable to transactivate LEP-Rb towards STAT3 signaling in heterodimeric complexes as probed by chimeric LEP-Ra/b-IL5R receptors [54]. Nevertheless, the possibility to form trimeric complexes comprising long and short receptor isoforms may provide a mechanism for modulating leptin responsiveness of hypothalamic neurons depending on the relative ratio of LEP-R isoforms[51].

Collectively, the structural insights reported here, which are supported by the large body of mutagenesis data on Leptin and LEP-R, provide the structural and mechanistic framework to further dissect Leptin-mediated signaling via the JAK-STAT axis in physiology and disease.

ACKNOWLEDGEMENTS

We thank the staff of beamlines P12, P13 and P14 (Petra III, Deutsches Elektronen-Synchrotron), and Proxima 2A (SOLEIL) for technical support and beamtime allocation. We are grateful to the staff of the VIB-VUB facility for Bio Electron Cryogenic Microscopy (BECM, Brussels, Belgium), the staff of the Laboratory of Cell Biology & Histology (CBH) and the Antwerp Centre for Advanced Microscopy (ACAM) (UAntwerpen, Antwerp, Belgium), and the electron Bio-Imaging Centre (eBIC) at the

Diamond Light Source (Didcot, UK) for technical support and infrastructural access, and H. Kenneweg for production of labeled nanobodies. The pGL3-rPAPluc plasmid containing the luciferase gene was a kind gift of Dr. Frank Peelman (VIB-UGent, Ghent, Belgium).
This work was supported by grants from the Research Foundation – Flanders (grant G0G0619N to K.V.) and the VIB (to S.N.S.). This work benefited from access to the Integrated Structural Biology platform of the Strasbourg Instruct-ERIC centre IGBMC-CBI. Financial support was provided by FRISBI (ANR-10-INBS-0005 to C.B.), Instruct-ERIC (PID 15107 to K.V.) , iNext-Discovery (project number 17947 to K.V. and funded by the Horizon 2020 program of the European Commission) and by the DFG (SFB 944, projects P8 and Z, to J.P.)

AUTHOR CONTRIBUTIONS

A.T. prepared constructs, performed protein expression and purification with contributions from A.D. and K.V. A.T., K.H.G.V. and K.V. determined and analyzed crystallographic structures with contributions from S.N.S. K.V. collected and analyzed cryo-EM data, with contributions from J.F., W.V.P., and S.N.S. A.T. performed BLI, and SEC-MALLS experiments. SAXS data were analyzed by K.V. and A.T. I.M. performed cellular assays. M.H. and C.P. performed smTIRFM experiments and data analysis. J.F.B. carried out evolutionary structural analyses and J.P. supervised the smTIRFM experiments. C.B. performed SV–AUC experiments and analyzed data. D.C. and J.T. contributed critical reagents. A.T., K.V. and S.N.S. wrote the manuscript with contributions and approval from all authors. K.V. and S.N.S. conceived and supervised the project and procured funding.

DECLARATION OF INTERESTS

WVP is the founder and chief executive officer of PUXANO. All other authors declare no competing interests.

Tables

Table 1 Crystallographic data and refinement, and SAXS data analysis

A. X-ray data analysis

	mLEP:mLEP-R_{CRH2} **PDB ID 7z3p**	hLEP:hLEP-R_{CRH2} **PDB ID 7z3q**	mLEP:mLEP-R_{IgCRH2} **PDB ID 7z3r**	mLEP-RFNIII:VHH-4.80 **PDB ID 8av2**
Data collection				
Space group	*P21212*	*C222*	*H32*	*P212121*
Cell dimensions				
a, *b*, *c* (Å)	96.73, 52.82, 89.06	156.20, 156.64, 95.55	132.68, 132.68, 249.19	53.19, 85.88, 144.69
α, β, γ (°)	90.00, 90.00, 90.00	90.00, 90.00, 90.00	90.00, 90.00, 120.00	90.00, 90.00, 90.00
Resolution (Å)	50.00-1.94 (2.06-1.94)	90.00-3.60 (3.82-3.60)	104.34-2.95 (3.13-2.95)	90.00-1.75 (1.86-1.75)
R_{meas} (%)	12.7 (240.4)	30.2 (180.0)	15.1 (340.6)	16.4 (206.6)
I / σI	16.08(1.07)	6.38 (0.96)	19.18 (1.03)	10.48 (0.86)
Completeness (%)	99.2 (95.4)	99.9 (99.9)	100.0 (100.0)	100.0 (99.9)
Redundancy	13.2 (13.0)	9.8 (10.1)	20.4 (20.6)	11.9 (11.5)
Refinement				
Resolution (Å)	46.35-1.94	60.57-3.62	66.34-2.95	25.42-1.75
No. reflections	34,115	13,623	18,073	67,651
R_{work} / R_{free}	19.10 / 22.10	27.50 / 30.53	22.27 / 25.12	19.34 / 23.33
No. atoms				
Protein	2,485	7,100	3,542	5,117
Carbohydrate	-	-	-	57.38
Ligand/ion	8	0	14	120
Water	154	2	7	514
B-factors				
Protein	54.98	185.05	111.97	37.48
Carbohydrate	-	-	-	57.38
Ligand/ion	58.45	-	155.82	70.69
Water	54.75	110.00	92.30	43.33
R.m.s. deviations				
Bond lengths (Å)	0.008	0.005	0.006	0.008
Bond angles (°)	0.97	0.74	0.86	0.93

*Each dataset was collected from a single crystal. Values in parentheses are for highest-resolution shell.

B. Radius of gyration (R_g) and molecular weight analysis via SAXS

Sample	**Concentration (mg/mL)**	**R_g (nm) [Guinier]**	Estimated MW (kDa) **BSA**	**VC**	**MoW**	Theoretical MW (kDa)
mLEP-R_{ECD}	3.8	9.1	192	170	153	94
mLeptin:mLEP-R_{ECD}	4.4	8.2	365	428	541	331
mLeptin:mLEP-$R_{ECD\text{-}tGCN4}$	3.4	8.0	399	450	552	341

Table 2| Cryo-EM data collection, refinement, and validation statistics

	mLeptin: mLEP-RECD (open 1:2 complex)	**mLeptin: mLEP-RECD-tGCN4** (closed 3:3 complex)	**mLeptin: mLEP-RECD-tGCN4** (closed 3:3 complex, local refinement)	**mLeptin: mLEP-RECD-tGCN4** (closed 3:3 complex, local refinement, symmetry expansion)	**hLeptin: hLEP-RECD-tGCN4** (open 2:2 complex)	**hLeptin: hLEP-RECD-tGCN4** (closed 3:3 complex)	**hLeptin: hLEP-RECD-tGCN4** (open 3:3 complex)
	EMD-15677 PDB 8avb	EMD-15678 PDB 8avc	EMD-15679 PDB 8avd	EMD-15899 PDB 8b7q	EMD-15680 PDB 8ave	EMD-15681 PDB 8avf	EMD-15683 PDB 8avo
Data collection and processing							
Magnification	60,000	105,000	105,000	105,000	60,000	60,000	60,000
Voltage (kV)	300	300	300	300	300	300	300
Electron exposure ($e^-/Å^2$)	61.8	45	45	45	62.4	62.4	62.4
Defocus range (μm)	0.8 – 3.0	1.2 – 2.5	1.2 – 2.5	1.2 – 2.5	0.8 – 3.0	0.8 – 3.0	0.8 – 3.0
Pixel size (Å)	0.76	0.829	0.829	0.829	0.76	0.76	0.76
Symmetry imposed	C1	C1	C1	C1	C1	C1	C1
Initial particle images (no.)	383,786	172,563	172,563	172,563	206,218	206,218	206,218
Final particle images (no.)	28,296	37,530	54,708	54,708 (x3)	91,899	29,899	30,353
Map resolution (Å)	4.43	4.60	4.42	4.02	5.62	6.45	6.84
FSC threshold	0.143	0.143	0.143	0.143	0.143	0.143	0.143
Map resolution range (Å)	17.6 – 4.0	11.7 – 4.3	13.2 – 3.8	7.5 – 3.3	12.2 – 5.0	15.5 – 5.9	14.7 – 5.9
Refinement							
Initial model used (PDB code, AlphaFold model)	7z3r, 8av2, AF-P48356-F1-model_v1	7z3r, 8av2, AF-P48356-F1-model_v1	7z3r	7z3r	7z3q, AF-P48357-F1-model_v2, AF- P41159-F1-model_v2	7z3q, AF-P48357-F1-model_v2, AF- P41159-F1-model_v2	7z3q, AF-P48357-F1-model_v2, AF- P41159-F1-model_v2
Model resolution (Å)	8.55	7.21	6.53	4.13	7.51	9.57	8.65
FSC threshold	0.5	0.5	0.5	0.5	0.5	0.5	0.5
Model resolution range (Å)	∞ - 8.55	∞ - 7.21	∞ - 6.53	∞ - 4.13	∞ - 7.51	∞ - 9.57	∞ - 8.65
Map sharpening *B* factor ($Å^2$)	-137.8	-141.7	-100.9	-106.3	-378.9	-419.2	-517.2
Model composition							
Non-hydrogen atoms	10,592	17,508	12,780	3,511	11,874	17,811	17,811
Protein residues	1,326	2,199	1,617	441	1,484	2,226	2,226
B factors ($Å^{-2}$)							
Protein	509.52	275.28	240.46	101.61	281.58	387.95	92.4
R.m.s. deviations							
Bond lengths (Å)	0.005	0.004	0.005	0.002	0.006	0.005	0..003
Bond angles (°)	0.823	0.804	1.096	0.614	1.267	1.067	0.688
Validation							
MolProbity score	2.06	2.08	2.07	1.88	2.01	1.84	1.85
Clashscore	17.42	17.96	15.24	4.41	18.97	6.20	4.59
Poor rotamers (%)	0.00	0.0	0.0	2.94	0.00	2.51	3.63
Ramachandran plot							
Favored (%)	95.45	95.37	94.37	95.61	96.48	96.81	96.88
Allowed (%)	4.40	4.31	5.25	3.93	3.12	2.72	3.12
Disallowed (%)	0.15	0.32	0.38	0.46	0.41	0.47	0.00

Figures

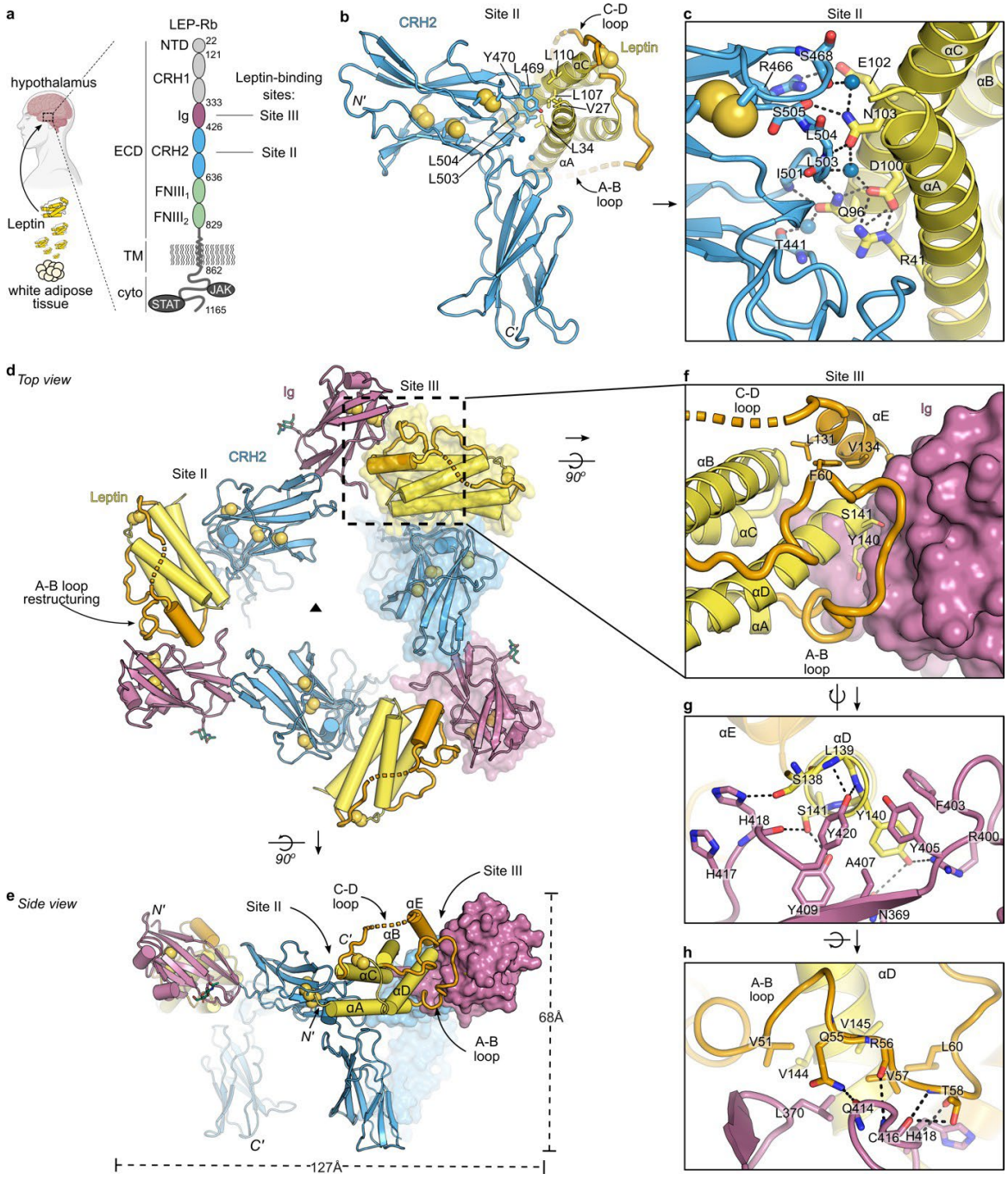

Fig. 1: Structural basis of Leptin site II and site III binding to LEP-R to form assemblies with 3:3 stoichiometry. a, Domain organization of Leptin and the JAK/STAT signaling-competent long LEP-R isoform that is overexpressed in the hypothalamus. Leptin interacts with the LEP-R_{CRH2} (blue) and LEP-R_{Ig} (violet) domains via sites II and III to initiate signaling. The image was created with BioRender.com and Inkscape.org. **b,** Crystal structure of the glycan-trimmed mLeptin:mLEP-R_{CRH2} assembly featuring the site II interface. Interface residues involved in hydrophobic interactions are shown as sticks. Disulfide bonds are shown as yellow spheres. **c,** Focused view of the mLeptin:mLEP-R_{CRH2} site II interface featuring hydrogen bonds (dashed lines). Bridging water molecules are shown as blue spheres. **d-e,** Crystal structure of the glycan-trimmed mLeptin:mLEP-R_{IgCRH2} assembly from a top and side view. The asymmetric unit, highlighted as surface, comprises the high-affinity binary complex featuring the interaction site II. Adjacent

copies of the binary complex assemble into a 3:3 complex mediated by interaction site III. **f,** The composite site III interface of Leptin with LEP-R_{Ig}. Leptin docks onto a surface cavity of LEP-R_{Ig} with the tip of α-helix D (blueprint Leptin site III residues in yellow sticks), and with the otherwise disordered A-B loop and α-helix E of the C-D loop that become ordered and internally stabilized with hydrophobic contacts (via residues shown as orange sticks). **g-h,** Site III interactions featuring Leptin's α-helix D (panel g) and A-B loop (panel h) with LEP-R_{Ig}. In all cases, sequence numbering corresponds to the Uniprot annotated sequences.

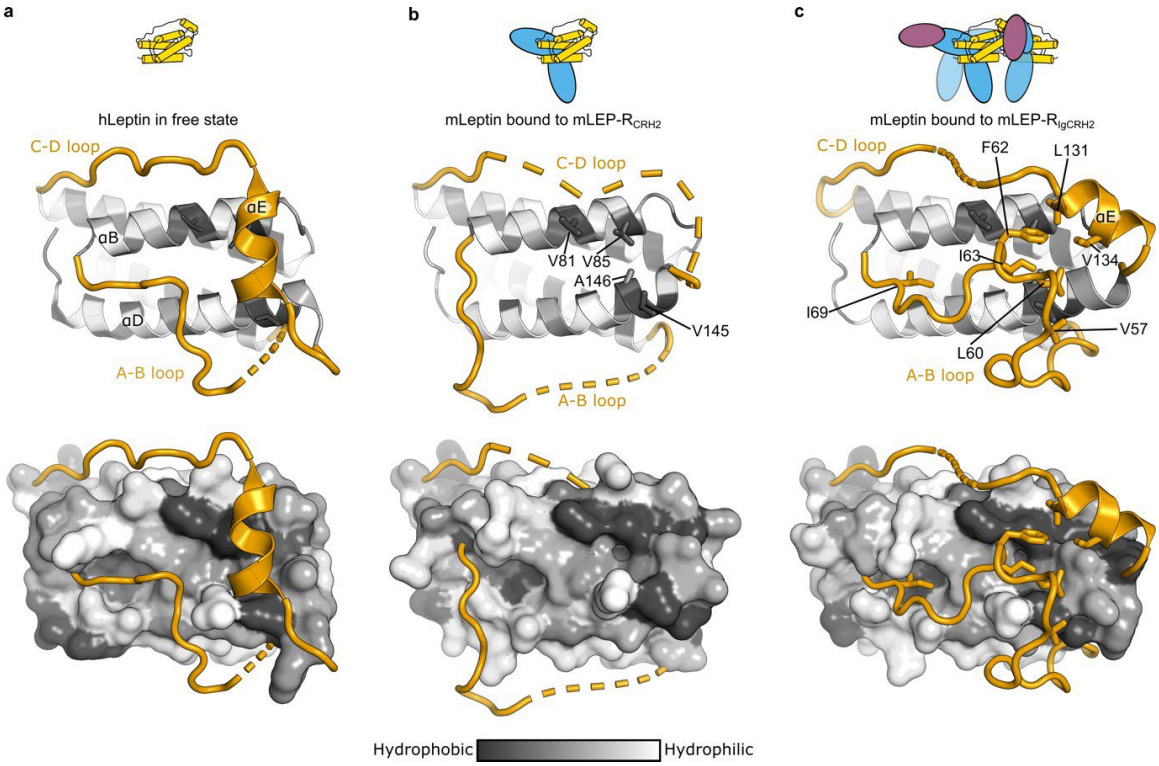

Fig. 2: Conformational plasticity in the loops of Leptin. a-c, The A-B and C-D loops of Leptin (orange) are shown relatively to the main four-helix-bundle body coloured according to the Eisenberg hydrophobicity-gradient scale at the free [1] (panel **a**; pdb: 1ax8; hLeptin), mLEP-R$_{CRH2}$-bound (panel **b**; pdb: 7z3p), and mLEP-R$_{Ig}$-bound state (panel **c**; pdb: 7z3r). A hydrophobic hub is formed at the surface of helices αB and αD of the four-helix-bundle by the indicated residues in grey. At the free state, the α-helix E was stabilized on this hub due to crystal packing. When not bound to LEP-R$_{Ig}$, the long loops of Leptin are dynamic and may transiently interact with the same hub. At the LEP-R$_{Ig}$-bound state, the hydrophobic hub is occupied by the A-B loop which in turn stabilizes the α-helix E in a V-configuration. This loop restructuring activates the site III on Leptin.

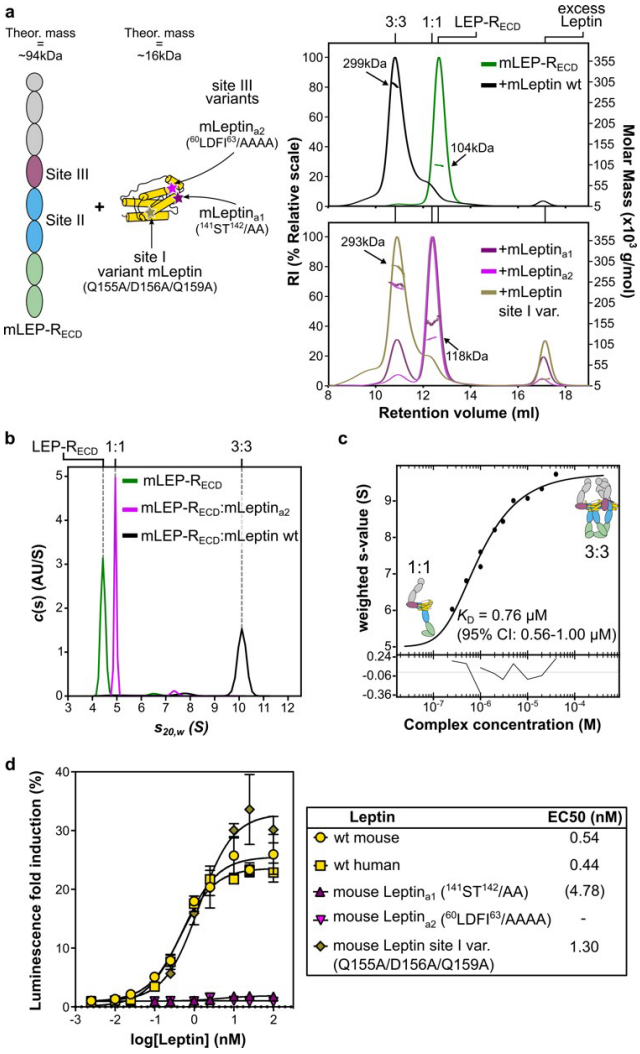

Fig. 3: Leptin-dependent receptor oligomerization in solution and in living cells. a, Molar mass determination of 40 µM glycan-trimmed mLEP-R_{ECD} alone or in complex with mLeptin variants by SEC-MALLS (Superdex 200 increase column). RI: Refractive index. Similar results were obtained from at least *n=4* independent experiments for the top panel, whereas *n=1* for the bottom panel. **b,** Sedimentation coefficient distributions c(s) of 40 µM glycan-trimmed mLEP-R_{ECD} alone or mixed at 1:1 molar ratio with mLeptin (wild type; wt) or mLeptin$_{a2}$ by AUC sedimentation velocity. **c,** Isotherm of the signal-weight-average s-values (*sw*) derived from the *c*(s) distributions presented in **Extended Data Fig. 3a**, and best-fit isotherm of a monomer-trimer self-association model with refined K_D indicated. *n=2* independent experiments. **d,** mLEP-Rb receptor activation by Leptin and variants probed by a STAT3 responsive luciferase reporter transiently transfected in HEK293T cells. Leptin$_{a1}$ only partially activates the receptor, in agreement with residual 3:3 oligomerization shown in panel a. *n=3* independent experiments with 3 technical replicates each. Here, mean values and standard deviations from a representative independent experiment are shown.

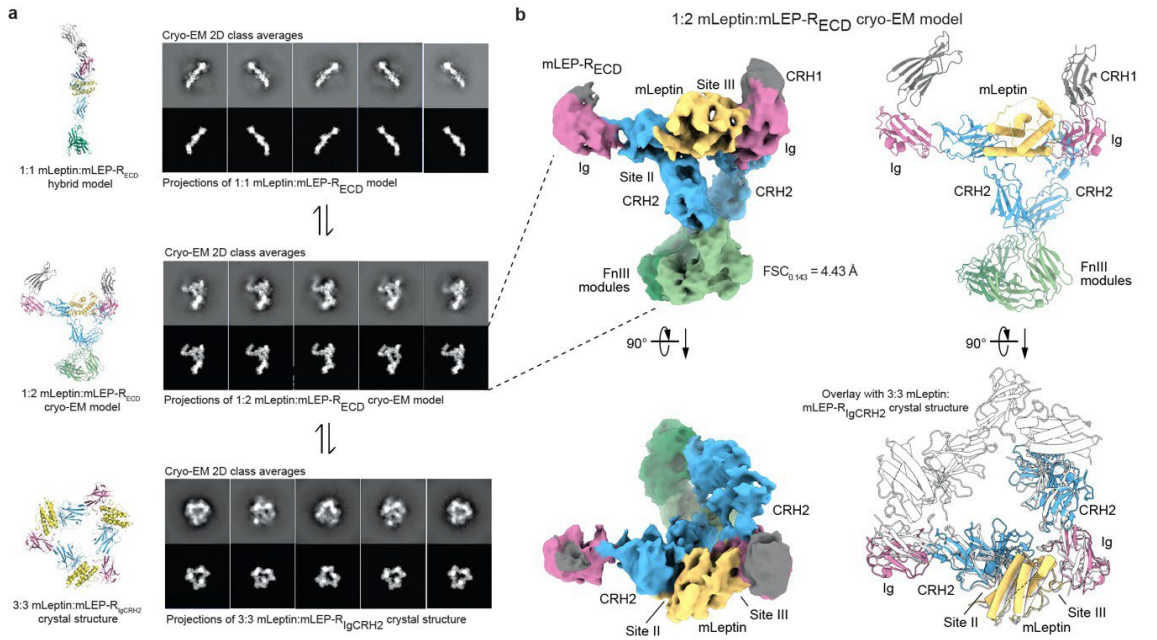

Fig. 4: Structural characterization of mLeptin:mLEP-R$_{ECD}$ complexes via cryo-EM reveals trimeric and intermediate assemblies. a, Cryo-EM 2D class averages for the mLeptin:mLEP-R$_{ECD}$ complex matched to projections of a hybrid structural model for the 1:1 mLeptin:mLEP-R$_{ECD}$ model based on the AlphaFold prediction for mLEP-R$_{ECD}$ and the mLeptin:mLEP-R$_{CRH2}$ crystal structure (top), projections of the 1:2 mLeptin:mLEP-R$_{ECD}$ cryo-EM model (middle) and projections of the determined 3:3 mLeptin:mLEP-R$_{IgCRH2}$ crystal structure (bottom). **b,** Cryo-EM map and real-space refined atomic model for the glycosylated 1:2 mLeptin:mLEP-R$_{ECD}$ complex. The sharpened map is contoured at 0.39 V and colored per zone with mLeptin in yellow, the CRH1-module in grey, the Ig-domain in magenta, the CRH2 module in blue and the FnIII modules in green.

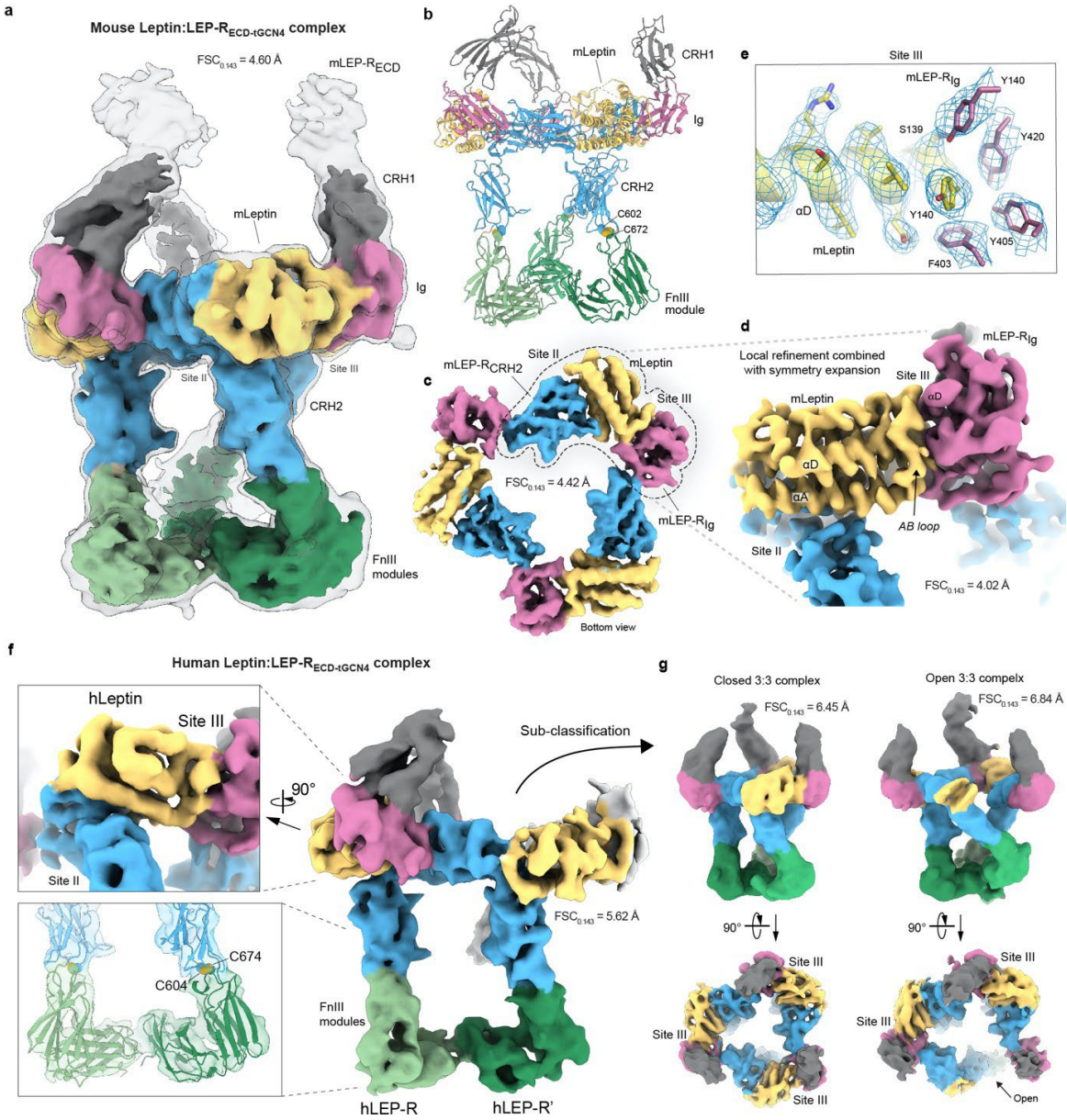

Fig. 5: Structural basis of trimerized mouse and human LEP-R mediated by Leptin. a,b, Cryo-EM maps and real-space refined atomic model for the glycosylated mLeptin:mLEP-R$_{ECD-tGCN4}$ assembly. The sharpened map is contoured at 0.178 V. The non-sharpened map is shown as a transparent volume contoured at 0.09 V. **c,** Sharpened cryo-EM map for the mLeptin:mLEP-R$_{ECD-tGCN4}$ assembly following local refinement around the mLeptin:mLEP-R$_{IgCRH2}$ core region. The map is contoured at 0.313 V and displayed as a carved volume around mLeptin, the Ig-domain and the first domain of the CRH2-module with a carve radius of 4 Å. **d,** Sharpened cryo-EM map following symmetry expansion of the particle set in combination with local refinement around one IgCRH2:Leptin:Ig' subcomplex. The map is contoured at 0.139 V. **e**, Sharpened map with DeepEMhancer following local refinement as in panel f. The map is centered around mLeptin-Y140 and contoured at 0.130 V and carved around the shown residues with a radius of 2.3 Å. **f,** Sharpened cryoEM map and real-space refined atomic model for the hLeptin:hLEP-R$_{ECD-tGCN4}$ complex contoured at 0.55 V. The map is colored via the same coloring scheme as for the mouse complex shown in panel a. **g**, Cryo-EM maps for the hLeptin:hLEP-R$_{ECD-tGCN4}$ complex following further 3D-subclassification. The top panel shows the non-sharpened cryo-EM maps contoured at 0.287 V and 0.245 V, respectively. The lower panel shows the corresponding sharpened maps in contoured at 0.45 V and 0.408 V.

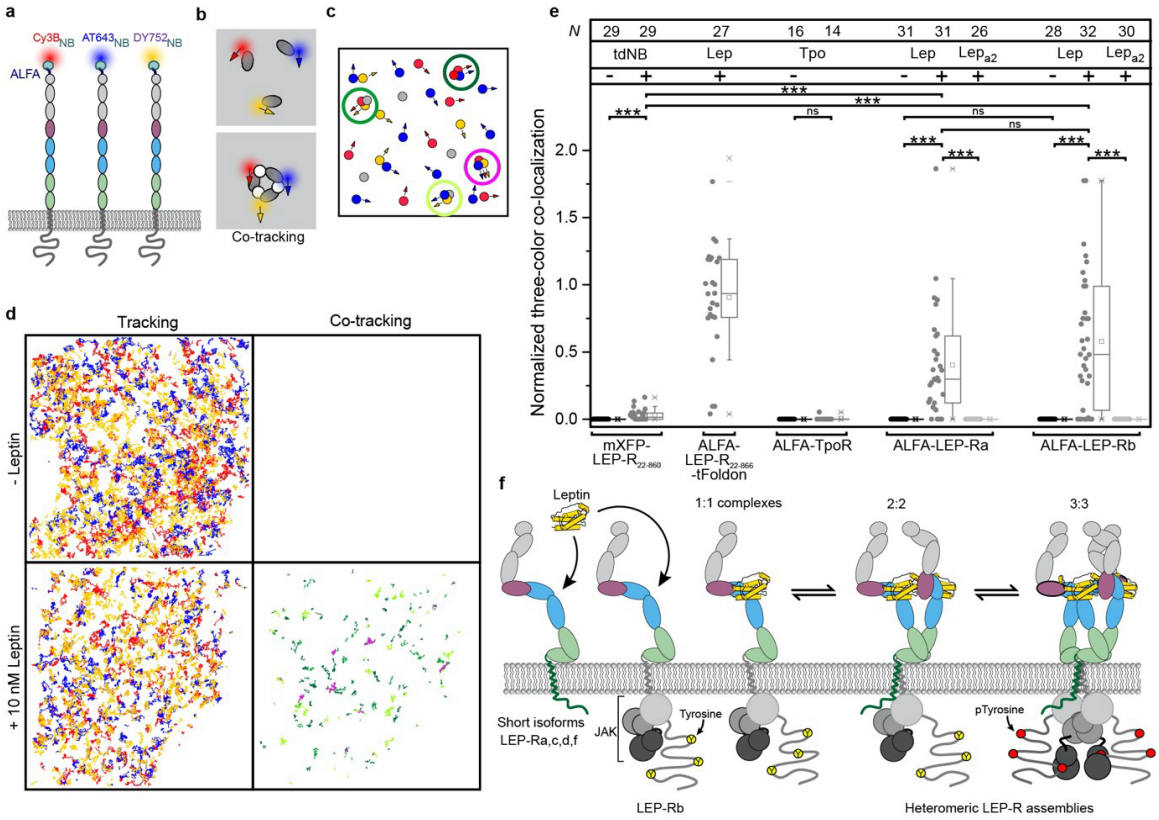

Fig. 6: Leptin-induced assembly of LEP-R trimers at the cell surface. a, Quantifying receptor assembly in the plasma membrane of live cells by triple-color single molecule co-tracking. mLEP-R with N-terminal ALFA-tag at the surface of HeLa cells were stochastically labeled with the indicated dyes conjugated to anti-ALFA-tag nanobodies. **b**, Trimeric receptors are identified by triple-color co-localization and co-tracking analysis. **c**, Detection of trimers is limited by the random and incomplete receptor labeling as well as co-tracking fidelity. Therefore, relatively high levels of receptor dimers (green circles) are expected in addition to triple-color trimers (magenta circles). **d**, Representative triple-color co-tracking analysis of mLEP-Rb in the absence (top) and presence (bottom) of mLeptin. Single molecule trajectories (left) and co-trajectories (right) with dual- and triple-color co-trajectories identified in green and magenta, respectively. **e,** Relative number of triple-color co-trajectories observed for unstimulated and stimulated receptors, normalized to the ALFA-LEP-R$_{222-866}$-tFoldon stimulated with mLeptin. tdNB, dimerizer based on a tandem anti-GFP nanobody. The total number of cells (N) analyzed over n=2 independent experiments for all LepR experiments, and n=1 control experiment for TpoR, is indicated in the top row. Statistics were performed using two-sided two-sample Kolmogorov-Smirnov test (not significant: ns; ***P $\leq$ 0.001). Exact P-values for each comparison are given in the source data file. Box and whisker plots show the five number summaries of the data: minimum, first quartile, median, third quartile, and maximum values. Outliers are indicated with an asterisk. **f,** Possible Leptin-mediated LEP-R assemblies at the cell surface comprising different stoichiometries of LEP-R isoforms. Red dots indicate pTyr in the active signaling complex.

References

1 Zhang, F. *et al.* Crystal structure of the obese protein leptin-E100. *Nature* **387**, 206-209, doi:10.1038/387206a0 (1997).

2 Wauman, J., Zabeau, L. & Tavernier, J. The Leptin Receptor Complex: Heavier Than Expected? *Frontiers in endocrinology* **8**, 30, doi:10.3389/fendo.2017.00030 (2017).

3 de Candia, P. *et al.* The pleiotropic roles of leptin in metabolism, immunity, and cancer. *The Journal of experimental medicine* **218**, doi:10.1084/jem.20191593 (2021).

4 Friedman, J. M. Leptin and the endocrine control of energy balance. *Nat Metab* **1**, 754-764, doi:10.1038/s42255-019-0095-y (2019).

5 Salum, K. C. R. *et al.* When Leptin Is Not There: A Review of What Nonsyndromic Monogenic Obesity Cases Tell Us and the Benefits of Exogenous Leptin. *Frontiers in endocrinology* **12**, 722441, doi:10.3389/fendo.2021.722441 (2021).

6 Farooqi, I. S. *et al.* Clinical and molecular genetic spectrum of congenital deficiency of the leptin receptor. *The New England journal of medicine* **356**, 237-247, doi:10.1056/NEJMoa063988 (2007).

7 Gorska, E. *et al.* Leptin receptors. *European journal of medical research* **15 Suppl 2**, 50-54, doi:10.1186/2047-783x-15-s2-50 (2010).

8 Fei, H. *et al.* Anatomic localization of alternatively spliced leptin receptors (Ob-R) in mouse brain and other tissues. *Proceedings of the National Academy of Sciences of the United States of America* **94**, 7001-7005, doi:10.1073/pnas.94.13.7001 (1997).

9 Haniu, M. *et al.* Human leptin receptor. Determination of disulfide structure and N-glycosylation sites of the extracellular domain. *The Journal of biological chemistry* **273**, 28691-28699, doi:10.1074/jbc.273.44.28691 (1998).

10 Zabeau, L. *et al.* Functional analysis of leptin receptor activation using a Janus kinase/signal transducer and activator of transcription complementation assay. *Molecular endocrinology (Baltimore, Md.)* **18**, 150-161, doi:10.1210/me.2003-0078 (2004).

11 Moharana, K. *et al.* Structural and mechanistic paradigm of leptin receptor activation revealed by complexes with wild-type and antagonist leptins. *Structure (London, England : 1993)* **22**, 866-877, doi:10.1016/j.str.2014.04.012 (2014).

12 Peelman, F. *et al.* Mapping of binding site III in the leptin receptor and modeling of a hexameric leptin.leptin receptor complex. *The Journal of biological chemistry* **281**, 15496-15504, doi:10.1074/jbc.M512622200 (2006).

13 Zabeau, L. *et al.* Leptin receptor activation depends on critical cysteine residues in its fibronectin type III subdomains. *The Journal of biological chemistry* **280**, 22632-22640, doi:10.1074/jbc.M413308200 (2005).

14 Tu, H., Hsuchou, H., Kastin, A. J., Wu, X. & Pan, W. Unique leptin trafficking by a tailless receptor. *FASEB journal : official publication of the Federation of American Societies for Experimental Biology* **24**, 2281-2291, doi:10.1096/fj.09-143487 (2010).

15 Ge, H., Huang, L., Pourbahrami, T. & Li, C. Generation of soluble leptin receptor by ectodomain shedding of membrane-spanning receptors in vitro and in vivo. *The Journal of biological chemistry* **277**, 45898-45903, doi:10.1074/jbc.M205825200 (2002).

16 Ferrao, R. D., Wallweber, H. J. & Lupardus, P. J. Receptor-mediated dimerization of JAK2 FERM domains is required for JAK2 activation. *eLife* **7**, doi:10.7554/eLife.38089 (2018).

17 Glassman, C. R. *et al.* Structure of a Janus kinase cytokine receptor complex reveals the basis for dimeric activation. *Science (New York, N.Y.)* **376**, 163-169, doi:10.1126/science.abn8933 (2022).

18 Mancour, L. V. *et al.* Ligand-induced architecture of the leptin receptor signaling complex. *Molecular cell* **48**, 655-661, doi:10.1016/j.molcel.2012.09.003 (2012).

19 White, D. W., Kuropatwinski, K. K., Devos, R., Baumann, H. & Tartaglia, L. A. Leptin receptor (OB-R) signaling. Cytoplasmic domain mutational analysis and evidence for receptor homo-oligomerization. *The Journal of biological chemistry* **272**, 4065-4071, doi:10.1074/jbc.272.7.4065 (1997).

20 Bacart, J. *et al.* Evidence for leptin receptor isoforms heteromerization at the cell surface. *FEBS letters* **584**, 2213-2217, doi:10.1016/j.febslet.2010.03.033 (2010).

21 Iserentant, H. *et al.* Mapping of the interface between leptin and the leptin receptor CRH2 domain. *Journal of cell science* **118**, 2519-2527, doi:10.1242/jcs.02386 (2005).

22 Peelman, F. *et al.* Mapping of the leptin binding sites and design of a leptin antagonist. *The Journal of biological chemistry* **279**, 41038-41046, doi:10.1074/jbc.M404962200 (2004).

23 Danielsson, J. *et al.* The Pierced Lasso Topology Leptin has a Bolt on Dynamic Domain Composed by the Disordered Loops I and III. *Journal of molecular biology* **432**, 3050-3063, doi:10.1016/j.jmb.2020.01.035 (2020).

24 Niv-Spector, L. *et al.* Mapping leptin-interacting sites in recombinant leptin-binding domain (LBD) subcloned from chicken leptin receptor. *The Biochemical journal* **390**, 475-484, doi:10.1042/BJ20050233 (2005).

25 Verploegen, S. A., Plaetinck, G., Devos, R., Van der Heyden, J. & Guisez, Y. A human leptin mutant induces weight gain in normal mice. *FEBS letters* **405**, 237-240, doi:10.1016/s0014-5793(97)00192-0 (1997).

26 Carpenter, B. *et al.* Structure of the human obesity receptor leptin-binding domain reveals the mechanism of leptin antagonism by a monoclonal antibody. *Structure (London, England : 1993)* **20**, 487-497, doi:10.1016/j.str.2012.01.019 (2012).

27 Spangler, J. B., Moraga, I., Mendoza, J. L. & Garcia, K. C. Insights into cytokine-receptor interactions from cytokine engineering. *Annual review of immunology* **33**, 139-167, doi:10.1146/annurev-immunol-032713-120211 (2015).

28 Varadi, M. *et al.* AlphaFold Protein Structure Database: massively expanding the structural coverage of protein-sequence space with high-accuracy models. *Nucleic acids research* **50**, D439-D444, doi:10.1093/nar/gkab1061 (2022).

29 Niv-Spector, L. *et al.* Identification of the hydrophobic strand in the A-B loop of leptin as major binding site III: implications for large-scale preparation of potent recombinant human and ovine leptin antagonists. *The Biochemical journal* **391**, 221-230, doi:10.1042/BJ20050457 (2005).

30 Gromada, J. S., P.; Altarejos, J.; Murphy, A. J. A leptin receptor agonist antibody for use in treating a metabolic dysfunction or hypoleptinemia. (2019).

31 Harbury, P. B., Kim, P. S. & Alber, T. Crystal structure of an isoleucine-zipper trimer. *Nature* **371**, 80-83, doi:10.1038/371080a0 (1994).

32 Walls, A. C. *et al.* Cryo-electron microscopy structure of a coronavirus spike glycoprotein trimer. *Nature* **531**, 114-117, doi:10.1038/nature16988 (2016).

33 Xu, Y. *et al.* Crystal structure of the entire ectodomain of gp130: insights into the molecular assembly of the tall cytokine receptor complexes. *The Journal of biological chemistry* **285**, 21214-21218, doi:10.1074/jbc.C110.129502 (2010).

34 Mirdita, M. *et al.* ColabFold: making protein folding accessible to all. *Nature methods* **19**, 679-682, doi:10.1038/s41592-022-01488-1 (2022).

35 Evans, R. *et al.* Protein complex prediction with AlphaFold-Multimer. *bioRxiv, preprint* doi:10.1101/2021.10.04.463034 (2022).

36 Liongue, C., Sertori, R. & Ward, A. C. Evolution of Cytokine Receptor Signaling. *Journal of immunology (Baltimore, Md. : 1950)* **197**, 11-18, doi:10.4049/jimmunol.1600372 (2016).

37 Sotolongo Bellon, J. *et al.* Four-color single-molecule imaging with engineered tags resolves the molecular architecture of signaling complexes in the plasma membrane. *Cell reports methods* **2**, 100165, doi:10.1016/j.crmeth.2022.100165 (2022).

38 Morris, R., Kershaw, N. J. & Babon, J. J. The molecular details of cytokine signaling via the JAK/STAT pathway. *Protein science : a publication of the Protein Society* **27**, 1984-2009, doi:10.1002/pro.3519 (2018).

39 Richter, D. *et al.* Ligand-induced type II interleukin-4 receptor dimers are sustained by rapid re-association within plasma membrane microcompartments. *Nature communications* **8**, 15976, doi:10.1038/ncomms15976 (2017).

40 Wilmes, S. *et al.* Mechanism of homodimeric cytokine receptor activation and dysregulation by oncogenic mutations. *Science (New York, N.Y.)* **367**, 643-652, doi:10.1126/science.aaw3242 (2020).

41 Martinez-Fabregas, J. *et al.* Kinetics of cytokine receptor trafficking determine signaling and functional selectivity. *Elife* **8**, e49314, doi:10.7554/eLife.49314 (2019).

42 Wilmes, S. *et al.* Receptor dimerization dynamics as a regulatory valve for plasticity of type I interferon signaling. *The Journal of cell biology* **209**, 579-593, doi:10.1083/jcb.201412049 (2015).

43 Gorby, C. *et al.* Engineered IL-10 variants elicit potent immunomodulatory effects at low ligand doses. *Science signaling* **13**, doi:10.1126/scisignal.abc0653 (2020).

44 Mazen, I., El-Gammal, M., Abdel-Hamid, M. & Amr, K. A novel homozygous missense mutation of the leptin gene (N103K) in an obese Egyptian patient. *Molecular genetics and metabolism* **97**, 305-308, doi:10.1016/j.ymgme.2009.04.002 (2009).

45 Wabitsch, M. *et al.* Biologically inactive leptin and early-onset extreme obesity. *The New England journal of medicine* **372**, 48-54, doi:10.1056/NEJMoa1406653 (2015).

46 Wabitsch, M. *et al.* Measurement of immunofunctional leptin to detect and monitor patients with functional leptin deficiency. *European journal of endocrinology* **176**, 315-322, doi:10.1530/EJE-16-0821 (2017).

47 Zastrow, O. *et al.* The soluble leptin receptor is crucial for leptin action: evidence from clinical and experimental data. *Int J Obes Relat Metab Disord* **27**, 1472-1478, doi:10.1038/sj.ijo.0802432 (2003).

48 Djogo, T. *et al.* Adult NG2-Glia Are Required for Median Eminence-Mediated Leptin Sensing and Body Weight Control. *Cell Metab* **23**, 797-810, doi:10.1016/j.cmet.2016.04.013 (2016).

49 Butiaeva, L. I. *et al.* Leptin receptor-expressing pericytes mediate access of hypothalamic feeding centers to circulating leptin. *Cell Metab* **33**, 1433-1448 e1435, doi:10.1016/j.cmet.2021.05.017 (2021).

50 Langendonk, J. G. *et al.* Circadian rhythm of plasma leptin levels in upper and lower body obese women: influence of body fat distribution and weight loss. *J Clin Endocrinol Metab* **83**, 1706-1712, doi:10.1210/jcem.83.5.4717 (1998).

51 Li, Z., Ceccarini, G., Eisenstein, M., Tan, K. & Friedman, J. M. Phenotypic effects of an induced mutation of the ObRa isoform of the leptin receptor. *Molecular metabolism* **2**, 364-375, doi:10.1016/j.molmet.2013.07.007 (2013).

52 Bjorbaek, C. *et al.* Expression of leptin receptor isoforms in rat brain microvessels. *Endocrinology* **139**, 3485-3491, doi:10.1210/endo.139.8.6154 (1998).

53 Bjorbaek, C., Uotani, S., da Silva, B. & Flier, J. S. Divergent signaling capacities of the long and short isoforms of the leptin receptor. *The Journal of biological chemistry* **272**, 32686-32695, doi:10.1074/jbc.272.51.32686 (1997).

54 Bahrenberg, G. *et al.* Identification of the critical sequence elements in the cytoplasmic domain of leptin receptor isoforms required for Janus kinase/signal transducer and activator of transcription activation by receptor heterodimers. *Molecular endocrinology (Baltimore, Md.)* **16**, 859-872, doi:10.1210/mend.16.4.0800 (2002).

METHODS

Protein expression in FreeStyle 293-F cells and purification from conditioned media

Human or murine LEP-R_{ECD}, segments or variants thereof as well as human or murine Leptin and their variants (**Supplementary Table 2**) were produced in FreeStyle 293-F cells (Cat. # R79007, Thermo Scientific) in suspension. Cells with density of approximately $1x10^6$ cells ml^{-1}, grown in FreeStyle™ 293 Expression Medium (Gibco), were transfected with 1 μg ml^{-1} DNA using 2-fold excess of linear polyethylenimine (PEI; Polysciences), pre-incubated for 15 min in Optimem medium (Gibco). Transfected cell cultures were supplemented with 1% Penicillin-Streptomycin. Ex-Cell® 293 Serum-Free Medium was added approximately 24 hours post-transfection to a final volume of 20%. Conditioned media containing the secreted recombinant protein were collected 4 days post transfection with centrifugation at 300 xg for 15 min and were filtrated with PES filters (0.22 μm, Millipore).

His_6-tag containing proteins were purified using metal ion affinity chromatography (IMAC; His-Trap FF, Cytiva). The column-captured material was washed sequentially with 1xPhosphate Buffer Saline (PBS; Sigma Aldrich), 1xPBS with 10mM Imidazole and eluted in 1xPBS supplemented with 250 mM Imidazole. The eluent was subjected to two rounds of SEC in 20 mM Hepes pH 7.4, 150 mM NaCl (HBS) using Superdex 200 increase 10/300 GL or Superdex 200 HiLoad 16/600 GL columns for LEP-R and Superdex 75 increase 10/300 GL for Leptin. For glycan-trimmed receptors, the IMAC-eluted material was concentrated to a maximal concentration of 1.5 mg ml^{-1} and incubated overnight with EndoH (1:50) at 4°C prior to SEC. For structural analysis (X-ray, SAXS) the His_6-tag was removed with incubation with 1:40 Caspase-3 or TEV proteases, depending on the construct (**Supplementary Table 2**) in addition to EndoH. Protein samples were concentrated using centrifugal filters (Amicon). Leptin:LEP-R complexes were subsequently formed *in vitro* from the individually purified components at the desired concentrations. Exceptions comprise the mLeptin:mLEP-R_{CRH2} and hLeptin:hLEP-R_{CRH2} complexes used for crystallographic studies that were produced by co-transfection of Leptin and LEP-R_{CRH2} in 1:1 DNA ratio.

Leptin expression in *E. coli*, and refolding and purification from inclusion bodies

Expression of Leptin and variants thereof in *E. coli* facilitated high yield production of active, monomeric Leptin. BL21(DE3) cells were transformed with a pET15b vector encoding human or mouse Leptin, using Carbenicillin for selection. Cell cultures in LB (0.5 Lt; 37°C) were inoculated with overnight pre-cultures (1:100 back-dilution) and gene expression was induced at OD_{600}=0.6 – 0.8 with 0.25 mM IPTG. Cells were harvested 3 to 5 hours post-induction by centrifugation (6,000 x g, 15 min, 4°C), resuspended in 50 mM Tris pH 8.0, 200 mM NaCl and lysed with a high-pressure homogenizer (Emulsiflex C3, Avestin). Inclusion bodies were harvested by centrifugation at 25,000 x g at 4°C for 20 min and were instantly frozen in liquid nitrogen. Inclusion bodies were resuspended in 6M Guanidine-HCl, 0.1M Tris pH 8.0 and homogenized with a Dounce homogenizer. The denatured sample was reduced with 5 mM DTT at 65°C for 10 min. Membranes and debris were removed by centrifugation at 47,000 xg for 30 min at 4°C. The supernatant was refolded at 4°C with pre-chilled 0.1 M Tris pH 8.0, 10 mM reduced GSH, 1 mM oxidized GSSG mixture at 1 ml min^{-1} to a final Guanidine-HCl concentration of 0.1 M. Typically this also secured Leptin concentration of less than 0.1 mg

ml^{-1} to minimize aggregation. Refolding was allowed overnight at 4ºC with gentle stirring. Large aggregates were removed by centrifugation at 4,000 x g at 4ºC for 15min and filtration (0.22 μm, Millipore). Refolded Leptin was then purified with IMAC (His-Trap FF, Cytiva) at 4ºC, pre-equilibrated with 0.1 M Tris pH 8.0. Two washing steps were performed with 0.1 M Tris pH 8.0 and 0.1 M Tris pH 8.0, 10 mM Imidazole respectively prior to elution in 0.1M Tris pH 8.0, 250mM Imidazole. The eluent was concentrated and injected onto a HiLoad 16/600 Superdex 75 (Cytiva) column pre-equilibrated in HBS. Peak fractions corresponding to the monomeric refolded Leptin were polished with an additional SEC (HiLoad Superdex 75 or Superdex 75 increase).

Preparation of protein complexes for crystallization

hLeptin:hLEP-R_{CRH2} complex

A codon-optimized cDNA fragment encoding the hLEP-R_{CRH2} receptor fragment (Uniprot ID P48357, residues 428-635) carrying the N516Q and C604S mutations was cloned into the pCAGGS vector in frame with the mouse Igh secretion signal (Uniprot ID Q32NZ5, residues 1-19) and an N-terminal TEV-cleavable hexahistidine-tag. A codon-optimized cDNA fragment encoding hLeptin (Uniprot ID P41159, residues 22-167) was cloned in the pTwist-CMV-BetaGlobin vector (Twist BioScience) in frame with the mouse Igh secretion signal (Uniprot ID Q32NZ5, residues 1-19) and an N-terminal TEV-cleavable hexahistidine-tag. hLEP-R_{CRH2}-N516Q/C604S and hLeptin were co-expressed in FreeStyle 293-F suspension cultures via PEI-mediated transient transfection in the presence of 20 μM kifunensine (Dextra Laboratories). The hLeptin:hLEP-R_{CRH2} complex was purified from the clarified conditioned medium via IMAC and SEC. N-linked glycans were trimmed by overnight incubation with EndoH using a 1:50 ratio (w/w) followed by SEC as a final polishing step using a Superdex 75 Increase column with HBS pH 7.4 as running buffer. The hLeptin:hLEP-R_{CRH2} complex (6 mg/mL) was subjected to crystallization trials using a Mosquito liquid handling robot (TTP Labtech) in sitting drop format. Crystals were obtained in condition F1 of the Index screen HT screen (0.2 M L-proline, 0.1 M HEPES pH 7.5, 10% PEG-3350) and cryo-protected with mother liquor supplemented with 20% PEG-400.

mLeptin:mLEP-R_{CRH2} complex

A codon-optimized cDNA fragment encoding the mLEP-R_{CRH2} receptor fragment (Uniprot ID P48356, residues 426 - 633) carrying the N514Q and C602S mutations was cloned into the pCAGGS vector in frame with the mouse Igh secretion signal and an N-terminal TEV-cleavable hexahistidine-tag. A codon-optimized cDNA fragment encoding mLeptin (Uniprot ID P41160, residues 22 – 167) was cloned in the pTwist-CMV-BetaGlobin vector in frame with the mouse Igh secretion signal and an N-terminal hexahistidine-tag. mLEP-R_{CRH2}-N514Q/C602S and mLeptin were co-expressed in FreeStyle 293-F suspension cultures via PEI-mediated transient transfection in the presence of 20 μM kifunensine (Dextra Laboratories). The mLeptin: mLEP-R_{CRH2} complex was purified from the clarified conditioned medium via IMAC and SEC. The complex was incubated overnight incubation at room temperature with TEV protease and EndoH (1:50 and 1:50 w/w respectively) for cleavage of the His-tag and trimming of the N-linked glycans, respectively, followed by SEC as a final

polishing step using a Superdex 75 Increase column with HBS pH 7.4 as running buffer. The mLeptin:mLEP-R_{CRH2} complex was concentrated to 7.6 mg mL^{-1} and subjected to crystallization trials using a Mosquito liquid handling robot (TTP Labtech) in sitting drop format. Crystals were obtained in condition H1 of the BCS screen HT screen (0.04 M calcium chloride dihydrate, 0.04 M sodium formate, 0.1 M Tris pH 8.0, 25% PEG Smear Low). Crystals were cryo-protected with mother liquor supplemented with 20% PEG-400.

mLeptin:mLEP-R_{IgCRH2} complex

For the mLeptin:mLEP-R_{IgCRH2} crystal structure, the mLEP-R_{IgCRH2} receptor fragment (Uniprot ID P48356 residues 328-633; C602S) was expressed in FreeStyle 293-F suspension cultures supplemented with the Mannosidase I inhibitor Kifunensine (Dextra Laboratories) at a final concentration of 20 μM. mLEP-R_{IgCRH2} secreted to the conditioned medium was purified using IMAC and was incubated with TEV and EndoH (1:20 and 1:50 w/w respectively) for cleavage of the purification tag and trimming of the N-glycans, respectively. The efficiency of the digestions was validated by SDS-PAGE and Western blot analysis using the 6X His Tag Monoclonal Antibody DyLight™ 800 (Rockland). The receptor was incubated with 2-fold molar excess of tag-less mLeptin (Uniprot ID P41160, residues 22 – 167), refolded from *E. coli* inclusion bodies as described in *Vernooy et al., 2010* (ref[55]). The complex was concentrated to 6.1 mg ml^{-1} and injected onto a Superdex 200 increase in HBS. Fractions of the main peak, corresponding to a 6:6 complex as determined previously by SEC-MALLS, were concentrated to 4 mg ml^{-1} and subjected to crystallization trials using a Mosquito liquid handling robot (TTP Labtech) in sitting drop format with 100 nL protein mixed with 100 nL mother liquor in SwissSci 96-well triple drop plates and incubation at 20°C. Crystals were obtained overnight at 3.0 M Sodium formate, 0.1 M Tris pH 7.5 and at 1.0 M Ammonium sulfate, 0.1 M MES pH 6.5 of the ProPlex HT-96 screen (Molecular Dimensions). Crystals were cryoprotected in 4 M sodium formate + 10% (v/v) ethylene glycol prior to being cryocooled in liquid nitrogen.

mLEP-R_{FnIII}:VHH 4.80 complex

A codon-optimized cDNA fragment encoding the mLEP-R_{FnIII} receptor fragment (Uniprot ID P48356 residues 633 - 827) and carrying the C672S and N668Q/N698Q/N726Q mutations was cloned in the pHLsec vector[56] in frame with the vector's secretion signal. A stop codon was inserted before the vector's C-terminal His-tag. A cDNA fragment encoding the anti-mLEP-R_{FnIII} nanobody VHH-4.80 (ref. [57]) was also cloned in the pHLsec vector in frame with the vector's secretion signal and in frame with the C-terminal His-tag. mLEP-R_{FnIII} and VHH-4.80 were co-expressed in HEK293S MGAT1$^{-/-}$ suspension cultures[58] via PEI-mediated transient transfection. The mLEP-R_{FnIII}:VHH-4.80 complex was purified from the clarified conditioned medium via IMAC and following buffer exchange to HBS, the complex was incubated overnight at room temperature with EndoH using a protein target:EndoH ration of 1:30 (w/w). SEC was performed as a final polishing step using a Superdex 75 Increase column with HBS pH 7.4 as running buffer. The glycan-minimized mLEP-R_{FnIII}:VHH-4.80 complex was concentrated to 2.5 mg ml^{-1} and subjected to crystallization trials using a Mosquito crystallization robot in sitting drop format with 200 nL protein mixed with 100 nL mother liquor in SwissSci 96-well triple drop plates and incubation at 20°C. Crystals were grown in

the condition C4 of the BCS HT screen (0.2 M ammonium sulphate, 0.1 M sodium cacodylate pH 5.6 and 30% PEG Smear Medium) and cryoprotected with mother liquor supplemented with 30% (v/v) PEG-400.

Crystallographic structure determination

Diffraction data was collected at the P13 and P14 (PETRAIII, DESY, Hamburg, Germany) and Proxima2A (SOLEIL, Paris, France) beam lines. All data were integrated and scaled using XDS [59] and AIMLESS [60] and data quality was analyzed by phenix.xtriage [61]. Phases for the minimal Leptin:LEP-R_{CRH2} complexes were obtained by maximum-likelihood molecular replacement with PHASER [62] using the coordinates of human Leptin (pdb 1ax8) and the human LEP-R_{CRH2} fragment (pdb 3v6o). The determined structure of mLeptin:mLEP-R_{CRH2} was used as search model to solve the mLeptin:mLEP-R_{IgCRH2} complex structure. To solve the structure of the mLEP-R_{FnIII}:VHH-4.80 complex search models were prepared based on pdb 1OHQ and a structural predicted model for mLEP-R via AlphaFold (AF-P48356-F1-model_v1). Model (re)building was performed in Coot [63] and refinement of coordinates and atomic displacement parameters was performed in PHENIX [61] and autoBUSTER [64]. Model and map validation tools in Coot and the PHENIX suite were used throughout the work flow to guide improvement and to validate the quality of crystallographic models. Hydrophobic moment plots for leptin were generated according to the Eisenberg hydrophobicity-gradient scale[65].

Multi-Angle Laser Light Scattering (SEC-MALLS)

Protein samples of 100 µl were injected at the indicated concentrations onto a Superdex 200 increase 10/300 GL or a Superose 6 increase 10/300 GL column (Cytiva) pre-equilibrated in 20mM Hepes pH 7.4, 150 mM NaCl at a flow rate of 0.75 ml min^{-1}. The column was coupled online with a UV-detector (Shimadzu), a miniDawnTReos (Wyatt) Multi-angle laser light scattering (MALLS) detector and an Optilab T-Rex (Wyatt) refractometer. The refractive increment value (dn/dc) was 0.185 ml g^{-1}. Data was processed with the Astra v6.1.2.84 and v8.0.2.5 software. Band broadening was corrected for using reference measurements of BSA (Pierce). Glycosylated receptor complexes were subsequently subjected to protein conjugate analysis using a modifier refractive increment value (dn/dc) of 0.165 ml g^{-1}. The reported masses in the figures correspond to the weight average molar masses, as documented by the Astra platform. Numerical averaged molar masses and the corresponding standard deviations (SD) form all individual points across an analyzed peak are provided in the source data files of the corresponding figures.

Biolayer Interferometry (BLI)

All measurements of binding kinetics and dissociation constants were performed using an Octet Red 96 (Forté Bio) in kinetics buffer (PBS, 0.1% (w/v) BSA, 0.02% (v/v) Tween-20) at 25ºC. mLEP-R_{CRH2} or mLeptin, as indicated, were *in vitro* biotinylated using the EZ-Link™ NHS-PEG4-Biotinylation kit (Pierce) and desalted for removal of free biotin prior to immobilization on streptavidin-coated biosensors (Forté Bio) at 1.2 and 1.5 nm level respectively. The corresponding ligands, mLeptin and mLEP-R_{ECD} respectively, were prepared in two-fold dilution series in kinetics buffer. Parallel referencing with non-functionalized

biosensors into all ligand concentrations as well as into kinetics buffers was employed. Data analysis was performed using Octet Analysis Studio 12.2 (Forté Bio) and binding curves were exported to Excel (Microsoft) for plotting of curves. Reported rate and affinity constants correspond to average values of three and four independent replicates for mLeptin:mLEP-R_{CRH2} and mLeptin:mLEP-R_{ECD} respectively. Standard deviations are given.

Sedimentation velocity Analytical Ultracentrifugation (AUC)

The day prior to sedimentation velocity experiments the protein samples stored at -80ºC were thawed and aggregates were removed by SEC (Superdex 200 10/30 GL and Superdex 75 10/30 GL for LEP-R and Leptin samples, respectively), equilibrated in SEC buffer (20 mM HEPES pH 7.4, 150 mM NaCl). SV–AUC experiments were conducted in a ProteomeLab XL-I analytical ultracentrifuge (Beckman Coulter) at 25 °C. The samples were loaded into AUC cell assemblies with 12- or 3-mm charcoal-filled Epon double-sector centerpieces. The sample cells were loaded into an 8-hole An-50 Ti rotor for temperature equilibration for 2–3 h, followed by acceleration to full speed at 128,429.2 xg. Absorbance data at 290 nm (for concentrations at 40 μM), 280 nm (for concentrations in the range 1 to 20 μM) or 233 nm (for concentrations in the range 0.25 to 1 μM) were collected at 5-minute intervals for 15 h. The partial specific volumes of the proteins, buffer density and viscosity were calculated using the software SEDNTERP. Sedimentation data were time-corrected and modelled with diffusion-deconvoluted sedimentation coefficient distributions c(s) in SEDFIT 16.1c, with signal-average frictional ratio and meniscus position refined with nonlinear regression [66]. Maximum entropy regularization was applied at a confidence level of 68%. Sedimentation coefficient distributions were corrected to standard conditions (water at 20°C, s20,W). Weight-averaged s-values (sw) at each concentration were determined by integrating c(s) distributions over the s-range of 4 to 12 S. Constructed sw isotherm were fitted with a monomer-trimer self-association model using SEDPHAT 15.2b to calculate the dissociation constant [67]. The error in KD was estimated using the "Critical chi square for error surface projections" option in SEDPHAT with a confidence level of 95%. All plots were created in GUSSI [68]. Two independent repeats were performed.

Leptin biological activity assay

HEK293T cells (293tsA1609)[69] were transiently transfected with the mLEP-$R_{ALFA\text{-}tag}$ and hLEP-$R_{ALFA\text{-}tag}$ described in **Supplementary Table 2** and the pGL3-rPAPluc reporter construct containing the luciferase gene under control of the STAT3-inducible rat pancreatitis-associated protein-1 promoter [70]. HEK293T cells were seeded into a 6-well plate and cultured overnight in DMEM (Invitrogen) and 10% fetal bovine serum (GibCo) in 5% CO2 at 37 °C. Next day, cells were transfected with mLEP-$R_{ALFA\text{-}tag}$ or hLEP-$R_{ALFA\text{-}tag}$ and the (optional: STAT3-responsive luciferase reporter construct) pGL3-rPAPluc DNA construct using linear polyethylenimine. After an overnight incubation, cells were detached using cell dissociation agent (Invitrogen) and 2% of the cell suspension was distributed per well of a 96-well plate. Cells were stimulated for 18h with increasing concentrations of human or mouse Leptin and mutant variants respectively. Afterwards, cells were lysed and the luciferase activity was measured by chemiluminescence in a Glomax luminometer (Promega) using luciferase substrate as previously described in *Peelman et al., 2004* (ref [22]). Relative luciferase induction

represents the stimulation factor normalized by the activity obtained with non-stimulated cells. Mean values were calculated from triplicates measured in parallel. Error bars represent standard deviations. The data were fitted to a log agonist versus response curve using GraphPad Prism.

Single Molecule Total Internal Reflection Fluorescence Microscopy (smTIRFM)

For cell surface labelling, receptors were N-terminally fused to suitable tags using a pSems vector including the signal sequence of Igκ (pSems-leader). TpoR, mLEP-Ra, mLEP-Rb and mLEP-R_{22-866}-tFoldon were fused to the ALFA-tag [71]; mLEP-R_{22-860} was fused to non-fluorescent monomeric GFP (mXFP) [40]. HeLa cells (ACC 57, DSMZ Germany) were cultured and transiently transfected as previously described [72]. Labeling, washing, and subsequent imaging were performed after mounting the coverslips into custom-made incubation chambers with a volume of 1 ml. Cells were equilibrated in medium with FBS but lacking phenol red supplemented with an oxygen scavenger and a redox-active photoprotectant (0.5 mg/ml glucose oxidase [Sigma-Aldrich], 0.04 mg/mL catalase [Roche], 5% wt/vol glucose, 1 µM ascorbic acid, and 1 µM methylviologene) to minimize photobleaching.[37]

Selective cell surface receptor labeling was achieved by using anti-GFP and anti-ALFAtag nanobodies (NBs), which were site specifically labelled by maleimide chemistry via a single cysteine residue at their C-termini. NBs labeled with Cy3B (DOL; anti-GFP: 1.03; anti-ALFA: 1.06), ATTO 643 (DOL; anti-GFP: 1.0; anti-ALFA: 1.0) and DY-752 (DOL; anti-GFP: 0.99; anti-ALFA: 0.85) were added at concentrations of 1.5 nM each, at least 10 min before imaging. Coverslips were precoated with poly-l-lysine-graft-poly(ethylene glycol) to minimize unspecific binding of nanobodies and functionalized with an RGD peptide for efficient cell adhesion[73].

Single-molecule imaging was carried out by triple-color total internal reflection fluorescence microscopy using an inverted microscope (IX-83, Olympus) equipped with a spectral image splitter (Multisplit V2, CAIRN) and a back-illuminated sCMOs camera (Hamamatsu ORCA Fusion-BT). Fluorophores were excited by simultaneous illumination with a 561 nm laser (MPB Communications), a 642 nm laser (MPB Communications) and a 730 nm laser (LuxX 730-50, Omicron). Image stacks of 150 frames were recorded for each cell at a time resolution of 33 ms per frame. Ligands (10 nM Leptin, 10 nM $Leptin_{a2}$, 10 nM Tpo) and a tandem nanobody (3 nM LaG16 dimerized by a maleimide crosslinker) diluted in culture medium with FBS were incubated for 10 min before imaging. All imaging experiments were carried out at 23°C.

Triple-color time-lapse images were evaluated using an in-house developed MATLAB software (SLIMfast4C, https://zenodo.org/record/5712332)[37] as schematically depicted in **Extended Data Fig. 9a**. After channel registration based on calibration with fiducial markers, molecules were localized using the multi-target tracking algorithm [74]. Immobile emitters were filtered out by spatiotemporal cluster analysis [75]. For co-tracking, frame-by-frame co-localization within a cut-off radius of 100 nm was applied followed by tracking of co-localized emitters using the utrack algorithm [76]. Molecules co-diffusing for 10 frames or more were identified as co-localized. Relative levels of co-localization were determined based on the fraction of co-localized particles [77]. Diffusion properties were determined from pooled single trajectory using mean squared displacement analysis for all trajectories with a lifetime greater

than 10 frames. Diffusion constants were determined from the mean squared displacement by linear regression.

Small Angle X-ray Scattering (SAXS)

For mLeptin:mLEP-R_{ECD}, the IMAC and SEC-purified glycan-trimmed receptor fragment was incubated with 1.5-fold molar excess of TEV-digested mLeptin refolded from *E. coli* inclusion bodies and injected onto a Superdex 200 increase 10/300 GL column in HBS, to remove the excess of Leptin. Samples of the complex were then prepared in HBS in a concentration range of 0.5 to 40 µM and were flash-frozen in liquid nitrogen. Samples in the same concentration range were also prepared for the mLEP-R_{ECD} alone, starting from the same glycan-trimmed receptor fragment sample used for the complex.

For mLeptin:mLEP-$R_{ECD\text{-}tGCN4}$, His_6-mLeptin refolded form *E. coli* inclusion bodies was used as a bait to pull down the tag-less mLEP-$R_{ECD\text{-}tGCN4}$ from conditioned media of FreeStyle 293-F cultures supplemented with 20 µM Kifunensine using IMAC. The complex was subjected to two rounds of SEC (Superose 6 increase 10/300 GL) in HBS, with TEV and EndoH-digestion implemented before the last SEC. 1.5-fold molar excess of TEV-digested mLeptin was added to the complex prior to the last SEC to ensure full receptor occupancy. Samples of the complex were then prepared in HBS at 14 and 30 µM and were flash-frozen in liquid nitrogen. Prior to analysis, all samples were centrifuged at 13,000xg for 10min at 20ºC.

In-solution SAXS data were measured on the P12 beamline of EMBL at the Petra III storage ring (DESY, Hamburg) in batch mode in HBS (20 mM HEPES, 150 mM NaCl, pH 7.2) at 25ºC using the BECQUEREL v2.0 control software. The scattering data was collected in continuous flow mode using an automatic sample changer with 0.1 s exposure time per frame using 35 µL of sample and a flow rate of 10 µL/s resulting in 35 x 0.1s exposures. Scattering data was radially averaged and buffer subtracted using the automated SASFLOW pipeline[78]. Analysis of the radius of gyration and molecular weight were performed using Primus in the ATSAS suite [79].

Cryo-EM data collection, image processing, structure modeling and refinement.

mLeptin:mLEP-R_{ECD} complex

Prior to complex formation the N-terminal His-tag of refolded mouse Leptin was removed by an overnight TEV protease digest at room temperature using a target protein:protease ratio (w/w) of 50:1 followed by a polishing step via a Superdex 75 Increase SEC run. A 1.5 molar excess of mouse Leptin was then added to purified, N-terminally His-tagged mLEP-R_{ECD} produced from HEK293 FreeStyle cells in the presence of 20 µM kifunensine as described above, and the resulting complex was isolated via SEC using a HiLoad 16/600 Superdex 200 column with HBS as running buffer. Fractions corresponding to the mLeptin:mLEP-R_{ECD} complex were pooled, concentrated to 5 mg/mL, aliquoted, flash-frozen into liquid nitrogen and stored at -80 °C until further use. Immediately prior to cryo-EM grid preparation the mLeptin:mLEP-R_{ECD} complex was thawed and diluted to 0.2 mg/mL with HBS buffer and 4 µL sample was applied to a glow-discharged Quantifoil R 0.6/1 300 mesh golden grid coated with graphene (PUXANO), blotted for 1 s (blot force = 1) under 100% humidity at 22 °C and plunged into liquid ethane using an FEI Vitribot Mark IV. Grids were screened using an JEOL 1400 Plus (BECM, Brussels). Data collection was performed using a JEOL cryoARM 300

microscope equipped with a 6k X 4k GATAN K3 detector resulting in 7100 movies with a raw pixel size of 0.755 Å. Movies were motion corrected via MotionCor2 1.4.0 (ref. [80]) and had their contrast transfer functions (CTFs) determined via patch-based CTF estimation as implemented in cryoSPARC v3.3.2 (ref. [81]). Particles were extracted with a box size of 440 pixels with 2x binning. Initial high-resolution 2D classes were obtained via the blob picker function and reference-free 2D classification in cryoSPARC, These 2D classes were then used to seed template-based particle picking and neural network-based particle picking via Topaz 0.2.4 (ref. [82]). Junk particles were removed by multiple rounds of 2D classification. High-resolution 2D classes corresponding to an apparent intermediate mLeptin:mLEP-R complex were selected and used for ab initio reconstruction followed by homogeneous and non-uniform refinement in cryoSPARC, which resulted in an anisotropic cryo-EM map for an 1:2 mLeptin:mLEP-R complex ($FSC_{0.143}$ = 4.43Å with 28,296 particles). An atomic model for a 1:2 mLeptin:LEP-$R_{IgCRH2FnIII}$ complex was created based on the AlphaFold [28,83] prediction for mLEP-R_{ECD} (AF-P48356-F1-model_v1) and the determined mLeptin:mLEP-R_{IgCRH2} and mLEP-R_{FnIII} module crystal structures and fitted in the cryo-EM map via Chimera. The atomic model was further refined via real space refinement in Phenix against the sharpened cryo-EM map using rigid body refinement and coordinate refinement with reference restraints to the starting model and hydrogen-bonding restraints across the site II and site III mLeptin:mLEP-R interface regions.

The COSMIC2 webserver [84] was used to align projections of the trimeric mLeptin:mLEP-R_{IgCRH2} crystal structure, the 1:2 mLeptin:LEP-$R_{IgCRH2FnIII}$ cryo-EM model, and projections of a 1:1 mLeptin:mLEP-R_{ECD} model based on the AF2-model for mLEP-R_{ECD} and the mLeptin:mLEP-R_{CRH2} crystal structure with high-resolution 2D-classes obtained for the mLeptin:mLEP-R_{ECD} complex sample.

mLeptin:mLEP-$R_{ECD\text{-}tGCN4}$ complex

The mouse LEP-R ectodomain (mLEP-R_{ECD}, residues 1 to 839) fused to a C-terminal trimeric GCN4 (tGNC4) zipper tag via a 5XGGS linker region was secreted from suspension HEK293 FreeStyle cells (ThermoFisher) in the presence of 20 µM kifunensine (Dextra) via PEI-mediated transient transfection as described above. N-terminally His-tagged, refolded mouse Leptin was added to the clarified conditioned medium and the mLeptin:mLEP-$R_{ECD\text{-}tGCN4}$ complex was purified via IMAC and a Superose 6 Increase SEC-column with HBS as running buffer. Top fractions were aliquoted and stored at -80 °C until further use. 4 µl of mLeptin:mLEP-$R_{ECD\text{-}tGCN4}$ complex at 0.3 mg/mL was applied to a glow-discharged C-Flat 1.2/1.3 300 mesh copper grid (Protochips), blotted for 4.5 s under 99% humidity at 22 °C and plunged into liquid ethane using a GP2 Leica grid plunger. Grids were screened using an JEOL 1400 Plus miscroscope (BECM, Brussels). Data collection was performed using a Titan Krios microscope equipped with a 6k x 4k GATAN K3 BIOQANTUM (eBIC, Didcot) resulting in 13,544 movies with a raw pixel size of 0.829 Å.

Movies were processed via patch-based motion correction and CTF estimation as implemented in cryoSPARC v3.3.1. Particles were extracted with a box size of 448 pixels with 2x binning. Initial 2D classes were obtained by the blob picker function in cryoSPARC, followed by particle picking via TOPAZ as implemented in cryoSPARC. Junk particles were removed by multiple rounds of 2D classification and ab initio 3D classification resulting in a particle set of

141,157 particles. Ab initio 3D classification followed by homogeneous and non-uniform refinement resulted in two cryo-EM maps representing the 3:3 mLeptin:mLEP-R_{ECD} complex. One map displayed better density for the 3:3 mLeptin:mLEP-R_{IgCRH2} core region of the complex and was used for local refinement ($FSC_{0.143}$ resolution = 4.42 Å with 54,708 particles). In the second map for the 3:3 mLeptin:mLEP-R_{ECD} the membrane-proximal regions of the receptor legs are better defined ($FSC_{0.143}$ = 4.60 Å with 37,530 particles). An atomic starting model for the 3:3 mLeptin:LEP-R_{ECD} complex was created based on the AlphaFold prediction for mLEP-R_{ECD} and the determined 3:3 mLeptin:mLEP-R_{IgCRH2} and mLEP-R_{FnIII} module crystal structures and fitted in the cryo-EM map via Chimera. The atomic model was further refined via real space refinement in Phenix against the sharpened cryo-EM map using rigid body refinement and coordinate refinement with reference restraints to the starting model and hydrogen-bonding restraints across the site II and site III mLeptin:mLEPR interface regions. In the cryo-EM maps for the 3:3 mLeptin:LEP-R_{ECD} complex strong additional density was observed at all three site II LEP-R_{CRH2}:Leptin interface regions that we interpreted as a trapped Ni-ion coordinated by histidine residues in the LEP-R_{CRH2} module and the N-terminal His-tag present on mLeptin (as shown in Extended Data Fig. 6a).
To address the breakage of symmetry in the ring-like core region of the complex and possibly revolve the mLEP-R_{CRH2}:mLeptin:mLEP-$R_{CRH1\text{-}IgCRH2}$ subcomplex at higher resolution, the pseudo-C3 symmetric volume obtained via local refinement of the 3:3 mLeptin:mLEP-R_{tGCN4} core region ($FSC_{0.143}$ resolution = 4.42 Å with 54,708 particles) was aligned to the pseudo-C3 symmetry axis via the Volume Alignment Tool job in cryoSPARC. The associated particle set was re-extracted without binning (0.829 Å per pixel) and symmetry expanded around the C3 axis resulting in 163,914 particles. Using the molmap function in Chimera, a volume blurred to 25 Å around one mLEP-R_{CRH2}:mLeptin:mLEP-$R_{}$ subcomplex was generated, and transformed into a mask with the Volume Tools job in cryoSPARC (map threshold = 0.04, dilation radius = 8.3 Å and soft padding width = 24.9 Å). Local refinement was performed by limiting the rotation and shift search extent around the original consensus refinement poses to 5° and 5 Å, respectively, in combination with a gaussian prior over the pose/shift magnitudes (with SD_{ROT} = 15 Å and SD_{SHIFT} = 7 Å). The center of mass of the mask was used as a fulcrum point. This approach resulted in a cryo-EM map with an $FSC_{0.143}$ resolution of 4.02 Å in which the crystallographic model for the mLEP-R_{CRH2}:mLeptin:mLEP-$R_{}$ complex was fitted using Chimera and real-space refined in Phenix using reference restraints to the starting model. To enhance high-resolution features the cryo-EM map was sharpened with DeepEMhancer[85].

hLeptin:hLEP-$R_{ECD\text{-}tGCN4}$ complex

The human LEP-R ectodomain (hLEP-R_{ECD}, residues 1 to 839) fused to a C-terminal trimeric GCN4 (tGNC4) zipper tag via a 5XGGS linker region was co-transfected with N-terminally His-tagged human Leptin in suspension HEK293 FreeStyle cells (ThermoFisher) in the presence of 20 µM kifunensine (Dextra) via PEI-mediated transient transfection. The resulting hLeptin:hLEP-$R_{ECD\text{-}tGCN4}$ complex was purified via IMAC and a Superose 6 Increase SEC-column with HBS as running buffer. Top fractions were aliquoted and stored at -80 °C until further use. 4 µl of hLeptin:hLEP-$R_{ECD\text{-}tGCN4}$ complex at 0.3 mg.mL^{-1} was applied to a glow-discharged Quantifoil R 0.6/1 300 mesh golden grid coated with graphene (PUXANO), blotted

for 1 s (blot force = 1) under 100% humidity at 22 °C and plunged into liquid ethane using an FEI Vitribot Mark IV. Grids were screened using an JEOL 1400 Plus microscope (BECM, Brussels). Data collection was performed using a JEOL cryoARM 300 microscope equipped with a 6k X 4k GATAN K3 detector resulting in 13,755 movies with a raw pixel size of 0.76 Å (BECM, Brussels). Movies were processed via patch-based motion correction and CTF estimation as implemented in cryoSPARC v3.1.0. Particles were extracted with a box size of 560 pixels with 2x binning. Initial 2D-classes were obtained via template-based particle picking using 2D-classes representing top views for a mLeptin:mLEP-$R_{\Delta FnIII\text{-}tGCN4}$ complex lowpass filtered to 20 Å. The mLEP-$R_{\Delta FnIII\text{-}tGCN4}$ construct corresponds to a tGCN4-trimerized version of mLEP-R_{ECD} without the membrane-proximal FNIII-module. The cryo-EM dataset for the mLeptin:mLEP-$R_{\Delta FnIII\text{-}tGCN4}$ complex we collected suffered from severe preferred particle orientations limiting further analysis. The obtained 2D classes for the hLeptin:hLEP-$R_{ECD\text{-}tGCN4}$ complex were then used to seed template-based picking and neural network-based particle picking via Topaz 0.2.4. Junk particles were removed by multiple rounds of 2D classification resulting in a particle set of 206,218 particles. High-resolution 2D classes were selected for ab initio 3D classification followed by heterogeneous refinement and non-uniform refinement which resulted in a cryo-EM map that showed well-defined density for a 2:2 hLeptin:hLEP-R_{ECD} subcomplex (91,899 particles, $FSC_{0.143}$ = 5.62 Å). This particle set was further subclassified via ab initio 3D classification and heterogeneous refinement followed by non-uniform refinement which resulted in cryo-EM maps representing closed (29,899 particles, $FSC_{0.143}$ = 6.45 Å) and open (30,353 particles, $FSC_{0.143}$ = 6.84 Å) states of the 3:3 hLeptin:hLEP-R_{ECD} complex.

Starting models model for the 2:2 and 3:3 hLeptin:hLEP-R_{ECD} complexes were created based on the AlphaFold predictions for hLEP-R_{ECD} (AF-P48357-F1-model_v2) and hLeptin (AF-P41159-F1-model_v2), and the determined crystal structures for the mouse 3:3 Leptin:LEP-R_{IgCRH2} complex and human Leptin:LEP-R_{CRH2} complex and fitted in the cryo-EM maps via Chimera. Atomic models were further refined via real space refinement in Phenix against the sharpened cryo-EM maps using rigid body refinement and coordinate refinement with reference restraints to the starting model.

Cryo-EM images for the mLeptin:mLEP-R_{ECD} complex, mLeptin:mLEP-$R_{ECD\text{-}tGCN4}$ complex and hLeptin:hLEP-$R_{ECD\text{-}tGCN4}$ complex are provided in Supplementary Figures 3-5. Cryo-EM data collection, processing and refinement statistics are also summarized in **Table 2**. All maps are reconstructed in C1 symmetry. Potential duplicate particles were removed within a distance of 150 Å. Reported resolutions are based on the gold-standard Fourier shell correlation (FSC) of 0.143 criterion [86] and Fourier shell correlation curves were corrected for the effects of soft masking by high-resolution noise substitution [87]. Map to model correlations were calculated using phenix.mtriage using the independent half maps as input. Local resolution maps were computed using the blocres algorithm[88] as implemented in cryoSPARC with an FSC threshold of 0.5. All representations of cryo-EM density and structural models were prepared with ChimeraX [89] and PyMol [90].

In silico structure prediction

Structural models for 1:1 mLeptin:mLEP-R_{Ig} and 1:1 mLeptin:mLEP-R_{CRH2} complexes, and for hexameric Leptin:LEP-R_{IgCRH2} assemblies were predicted using the latest version 2.2 of AlphaFold-Multimer implemented through ColabFold [34,35]. AlphaFold2-ptm was used for the prediction of mLEP-R_{IgCRH2}. Predicted structural models were aligned to the 3:3 mLeptin:mLEP-R_{IgCRH2} crystal structure in Pymol.

Determination of disulfide bridges by mass spectrometry

Sample preparation: To 50 µL of mLEP-R_{ECD}, 5 µL of 1 M Tris-HCl pH 8.0 was added, followed by 5 µL of PNGase F (New England Biolabs, P0704L). The sample was incubated at 37°C for 3h to allow the de-N-glycosylation to proceed. Next, the sample was denatured by adding guanidine hydrochloride to a final concentration of 3M, and stored at room temperature for 20 min. A buffer exchange was performed using a ZebaTM spin desalting column (ThermoFisher Scientific, 89882), with 100 mM Tris-HCl pH 7.5 as destination buffer. Trypsin (Promega, V5117) was added at a 1:25 (w:w) protease/protein ratio, and the sample was incubated overnight at 37°C.

LC-MS: The tryptic digest was analyzed on LC-MS using a C18 column and with H2O, acetonitrile and formic acid as mobile phase constituents. The analysis was performed on a 1290 Infinity UHPLC system coupled to a 6540 Q-TOF mass spectrometer (both Agilent Technologies). The MS instrument was equipped with a AJS-ESI source and operated in positive electrospray ionization mode. The TOF was calibrated prior to the analysis and subsequently operated without utilizing reference masses. Data was collected in centroid mode at a rate of 3 spectra per s in the extended dynamic range mode (2 GHz). MS/MS experiments were performed using data-dependent acquisition (DDA). One survey MS measurement was complemented with 5 data-dependent MS/MS measurements. Doubly, triply and quadruply charged precursor ions were selected based on abundance. After being fragmented twice, a particular m/z value was excluded for 30 s. The quadrupole was operated at medium resolution and the collision energy varied based on m/z. Data acquisition was performed with MassHunter Data Acquisition software, while data processing was performed in MassHunter Qualitative Analysis with BioConfirm add-on (all from Agilent Technologies).

Materials availability

The HEK293S *MGAT1*$^{-/-}$ cell line and derivatives thereof cannot be freely distributed as some rights remain with the original authors.

Protein expression constructs generated in this study (as listed in **Supplementary Table 2**) are available via the BCCM/GeneCorner Plasmid Collection (http://bccm.belspo.be). In all cases, sequence numbering corresponds to the Uniprot annotated sequences, as indicated.

Data availability

Crystallographic coordinates and structure factors have been deposited in the Protein Data Bank (PDB), and cryo-EM maps and models have been deposited in the Electron Microscopy Data Bank (EMDB) and PDB data banks with accession codes listed in **Tables 1** and **2**. Briefly, the crystal structure of mLeptin:mLEP-R_{CRH2} is deposited under the accession code PDB 7z3p,

hLeptin:hLEP-R_{CRH2} under PDB 7z3q, mLeptin:mLEP-R_{IgCRH2} under PDB 7z3r, and mLEP-R_{FNIII}:VHH-4.80 under PDB 8av2. The cryo-EM map of the open 1:2 mLeptin:mLEP-R_{ECD} complex has been deposited under the accession codes EMD-15677 and PDB 8avb. The cryo-EM map of the closed 3:3 mLeptin:mLEP-R_{ECD}-$_{tGCN4}$ complex has been deposited under the accession codes EMD-15678 and PDB 8avc, after local refinement under accession codes EMD-15679 and PDB 8avd, and after local refinement and symmetry expansion under accession codes EMD-15899 and PDB 8b7q. The cryo-EM map of the open 2:2 hLeptin:hLEP-R_{ECD}-$_{tGCN4}$ complex has been deposited under the accession codes EMD-15680 and PDB 8ave, the closed 3:3 hLeptin:hLEP-R_{ECD}-$_{tGCN4}$ complex under EMD-15681 and PDB 8avf, and the open 3:3 hLeptin:hLEP-R_{ECD}-$_{tGCN4}$ complex under EMD-15683 and PDB 8avo.
Search models for molecular replacement were prepared using pdb 1ax8 (hLeptin), pdb 3v6o (hLEP-R_{CRH2} fragment), pdb 1OHQ (VHH model) and AF-P48356-F1-model_v1 (for mLEP-R_{FnIII}). Coordinates for the IL6 (pdb 1p9m) and GCSF (pdb 2d9q) receptor complexes were used for comparative analysis. Structural predictions via Alphafold were used to generate starting models for real-space cryo-EM refinement: mLEP-R (AF-P48356-F1-model_v1), hLeptin (AF-P41159-F1-model_v2), hLEP-R (AF-P48357-F1-model_v2).
TIRF microscopy data from localization and co-tracking analysis have been uploaded into the publicly available repository Zenodo together with representative raw imaging data and are available at https://doi.org/10.5281/zenodo.7419603. AUC data are publicly available at https://doi.org/10.5281/zenodo.7566572. All remaining data generated or analysed during this study are included in this published article (and its supplementary information files).

Methods References

55 Vernooy, J. H. *et al.* Leptin modulates innate and adaptive immune cell recruitment after cigarette smoke exposure in mice. *Journal of immunology (Baltimore, Md. : 1950)* **184**, 7169-7177, doi:10.4049/jimmunol.0900963 (2010).

56 Aricescu, A. R., Lu, W. & Jones, E. Y. A time- and cost-efficient system for high-level protein production in mammalian cells. *Acta Crystallogr D Biol Crystallogr* **62**, 1243-1250, doi:10.1107/S0907444906029799 (2006).

57 Zabeau, L. *et al.* A novel leptin receptor antagonist uncouples leptin's metabolic and immune functions. *Cell Mol Life Sci* **76**, 1201-1214, doi:10.1007/s00018-019-03004-9 (2019).

58 Reeves, P. J., Callewaert, N., Contreras, R. & Khorana, H. G. Structure and function in rhodopsin: high-level expression of rhodopsin with restricted and homogeneous N-glycosylation by a tetracycline-inducible N-acetylglucosaminyltransferase I-negative HEK293S stable mammalian cell line. *Proc Natl Acad Sci U S A* **99**, 13419-13424, doi:10.1073/pnas.212519299 (2002).

59 Kabsch, W. Xds. *Acta Crystallogr D Biol Crystallogr* **66**, 125-132, doi:10.1107/S0907444909047337 (2010).

60 Evans, P. R. & Murshudov, G. N. How good are my data and what is the resolution? *Acta Crystallogr D Biol Crystallogr* **69**, 1204-1214, doi:10.1107/S0907444913000061 (2013).

61 Liebschner, D. *et al.* Macromolecular structure determination using X-rays, neutrons and electrons: recent developments in Phenix. *Acta Crystallogr D Struct Biol* **75**, 861-877, doi:10.1107/S2059798319011471 (2019).

62 McCoy, A. J. *et al.* Phaser crystallographic software. *J Appl Crystallogr* **40**, 658-674, doi:10.1107/S0021889807021206 (2007).

63 Emsley, P. & Cowtan, K. Coot: model-building tools for molecular graphics. *Acta crystallographica. Section D, Biological crystallography* **60**, 2126-2132, doi:10.1107/S0907444904019158 (2004).

64 Bricogne G., B. E., Brandl M., Flensburg C., Keller P., Paciorek W., Roversi P, Sharff A., Smart O.S., Vonrhein C., Womack T.O. BUSTER version 2.10.4. *Cambridge, United Kingdom: Global Phasing Ltd.* (2017).

65 Eisenberg, D., Schwarz, E., Komaromy, M. & Wall, R. Analysis of membrane and surface protein sequences with the hydrophobic moment plot. *Journal of molecular biology* **179**, 125-142, doi:10.1016/0022-2836(84)90309-7 (1984).

66 Schuck, P. Size-distribution analysis of macromolecules by sedimentation velocity ultracentrifugation and lamm equation modeling. *Biophysical journal* **78**, 1606-1619, doi:10.1016/S0006-3495(00)76713-0 (2000).

67 Schuck, P. On the analysis of protein self-association by sedimentation velocity analytical ultracentrifugation. *Analytical biochemistry* **320**, 104-124, doi:10.1016/s0003-2697(03)00289-6 (2003).

68 Brautigam, C. A. Calculations and Publication-Quality Illustrations for Analytical Ultracentrifugation Data. *Methods in enzymology* **562**, 109-133, doi:10.1016/bs.mie.2015.05.001 (2015).

69 DuBridge, R. B. *et al.* Analysis of mutation in human cells by using an Epstein-Barr virus shuttle system. *Mol Cell Biol* **7**, 379-387, doi:10.1128/mcb.7.1.379-387.1987 (1987).

70 Eyckerman, S. *et al.* Analysis of Tyr to Phe and fa/fa leptin receptor mutations in the PC12 cell line. *European cytokine network* **10**, 549-556 (1999).

71 Götzke, H. *et al.* The ALFA-tag is a highly versatile tool for nanobody-based bioscience applications. *Nature communications* **10**, 4403, doi:10.1038/s41467-019-12301-7 (2019).

72 Wilmes, S. *et al.* Receptor dimerization dynamics as a regulatory valve for plasticity of type I interferon signaling. *J Cell Biol* **209**, 579-593, doi:10.1083/jcb.201412049 (2015).

73 You, C., Richter, C. P., Löchte, S., Wilmes, S. & Piehler, J. Dynamic Submicroscopic Signaling Zones Revealed by Pair Correlation Tracking and Localization Microscopy. *Analytical Chemistry* **86**, 8593-8602, doi:10.1021/ac501127r (2014).

74 Serge, A., Bertaux, N., Rigneault, H. & Marguet, D. Dynamic multiple-target tracing to probe spatiotemporal cartography of cell membranes. *Nature methods* **5**, 687-694, doi:10.1038/nmeth.1233 (2008).

75 Niewidok, B. *et al.* Single-molecule imaging reveals dynamic biphasic partition of RNA-binding proteins in stress granules. *The Journal of cell biology* **217**, 1303-1318, doi:10.1083/jcb.201709007 (2018).

76 Jaqaman, K. *et al.* Robust single-particle tracking in live-cell time-lapse sequences. *Nature methods* **5**, 695-702, doi:10.1038/nmeth.1237 (2008).

77 Sotolongo Bellón, J. *et al.* Four-color single-molecule imaging with engineered tags resolves the molecular architecture of signaling complexes in the plasma membrane. *Cell Reports Methods* **2**, 100165, doi:https://doi.org/10.1016/j.crmeth.2022.100165 (2022).

78 Blanchet, C. E. *et al.* Versatile sample environments and automation for biological solution X-ray scattering experiments at the P12 beamline (PETRA III, DESY). *J Appl Crystallogr* **48**, 431-443, doi:10.1107/S160057671500254X (2015).

79 Manalastas-Cantos, K. *et al.* ATSAS 3.0: expanded functionality and new tools for small-angle scattering data analysis. *J Appl Crystallogr* **54**, 343-355, doi:10.1107/S1600576720013412 (2021).

80 Zheng, S. Q. *et al.* MotionCor2: anisotropic correction of beam-induced motion for improved cryo-electron microscopy. *Nat Methods* **14**, 331-332, doi:10.1038/nmeth.4193 (2017).

81 Punjani, A., Rubinstein, J. L., Fleet, D. J. & Brubaker, M. A. cryoSPARC: algorithms for rapid unsupervised cryo-EM structure determination. *Nat Methods* **14**, 290-296, doi:10.1038/nmeth.4169 (2017).

82 Bepler, T. *et al.* Positive-unlabeled convolutional neural networks for particle picking in cryo-electron micrographs. *Nat Methods* **16**, 1153-1160, doi:10.1038/s41592-019-0575-8 (2019).

83 Jumper, J. *et al.* Highly accurate protein structure prediction with AlphaFold. *Nature* **596**, 583-589, doi:10.1038/s41586-021-03819-2 (2021).

84 Cianfrocco MA, W. M., Youn C, Wagner R, Leschziner AE. COSMIC²: A Science Gateway for Cryo-Electron Microscopy Structure Determination. *Practice & Experience in Advanced Research Computing. New Orleans, LA July 9-13*, doi:https://doi.org/10.1145/3093338.3093390 (2017).

85 Sanchez-Garcia, R. *et al.* DeepEMhancer: a deep learning solution for cryo-EM volume post-processing. *Communications biology* **4**, 1-8 (2021).

86 Rosenthal, P. B. & Henderson, R. Optimal determination of particle orientation, absolute hand, and contrast loss in single-particle electron cryomicroscopy. *Journal of molecular biology* **333**, 721-745 (2003).

87 Chen, S. *et al.* High-resolution noise substitution to measure overfitting and validate resolution in 3D structure determination by single particle electron cryomicroscopy. *Ultramicroscopy* **135**, 24-35, doi:10.1016/j.ultramic.2013.06.004 (2013).

88 Cardone, G., Heymann, J. B. & Steven, A. C. One number does not fit all: mapping local variations in resolution in cryo-EM reconstructions. *Journal of structural biology* **184**, 226-236 (2013).

89 Pettersen, E. F. *et al.* UCSF ChimeraX: Structure visualization for researchers, educators, and developers. *Protein Science* **30**, 70-82 (2021).

90 Schrödinger. The PyMOL Molecular Graphics System, Version 2.0.

91 Peelman, F., Zabeau, L., Moharana, K., Savvides, S. N. & Tavernier, J. 20 years of leptin: insights into signaling assemblies of the leptin receptor. *The Journal of endocrinology* **223**, T9-23, doi:10.1530/JOE-14-0264 (2014).

92 Boulanger, M. J., Chow, D. C., Brevnova, E. E. & Garcia, K. C. Hexameric structure and assembly of the interleukin-6/IL-6 alpha-receptor/gp130 complex. *Science (New York, N.Y.)* **300**, 2101-2104, doi:10.1126/science.1083901 (2003).

93 Tamada, T. *et al.* Homodimeric cross-over structure of the human granulocyte colony-stimulating factor (GCSF) receptor signaling complex. *Proceedings of the National Academy of Sciences of the United States of America* **103**, 3135-3140, doi:10.1073/pnas.0511264103 (2006).

94 Amemiya, C. T. *et al.* The African coelacanth genome provides insights into tetrapod evolution. *Nature* **496**, 311-316, doi:10.1038/nature12027 (2013).

95 Londraville, R. L., Prokop, J. W., Duff, R. J., Liu, Q. & Tuttle, M. On the Molecular Evolution of Leptin, Leptin Receptor, and Endospanin. *Frontiers in endocrinology* **8**, 58, doi:10.3389/fendo.2017.00058 (2017).

Extended Data

Mechanism of receptor assembly via the pleiotropic adipokine Leptin

Alexandra Tsirigotaki[1,2], Ann Dansercoer[1,2], Koen H.G. Verschueren[1,2], Iva Marković[1,2], Christoph Pollmann[3], Maximillian Hafer[3], Jan Felix[1,2], Catherine Birck[4], Wouter Van Putte[5], Dominiek Catteeuw[6,7,#], Jan Tavernier[6,7,‡], J. Fernando Bazan[2,8], Jacob Piehler[3], Savvas N. Savvides[1,2*] & Kenneth Verstraete[1,2*]

[1] Unit for Structural Biology, Department of Biochemistry and Microbiology, Ghent University, Ghent, Belgium.
[2] Unit for Structural Biology, VIB-UGent Center for Inflammation Research, Ghent, Belgium.
[3] Department of Biology/Chemistry and Center of Cellular Nanoanalytics, Osnabrück University, Osnabrück, Germany.
[4] Integrated Structural Biology Platform, Centre for Integrative Biology (CBI), Institut de Génétique et de Biologie Moléculaire et Cellulaire (IGBMC), CNRS UMR 7104, INSERM U1258, University of Strasbourg, Illkirch, France.
[5] PUXANO, PXN BioLabs. BlueChem Incubator, Antwerp, Belgium.
[6] VIB-UGent Center for Medical Biotechnology, Ghent, Belgium.
[7] Department of Biomolecular Medicine, Ghent University, Ghent, Belgium.
[8] ħ Bioconsulting llc, Stillwater, MN, USA.
[#] Current address: Department of Biochemistry and Microbiology, Ghent University, Ghent, Belgium.
[‡] Current address: Orionis Biosciences, Ghent, Belgium.
* Corresponding authors: e-mail to savvas.savvides@ugent.be, kenneth.verstraete@ugent.be.

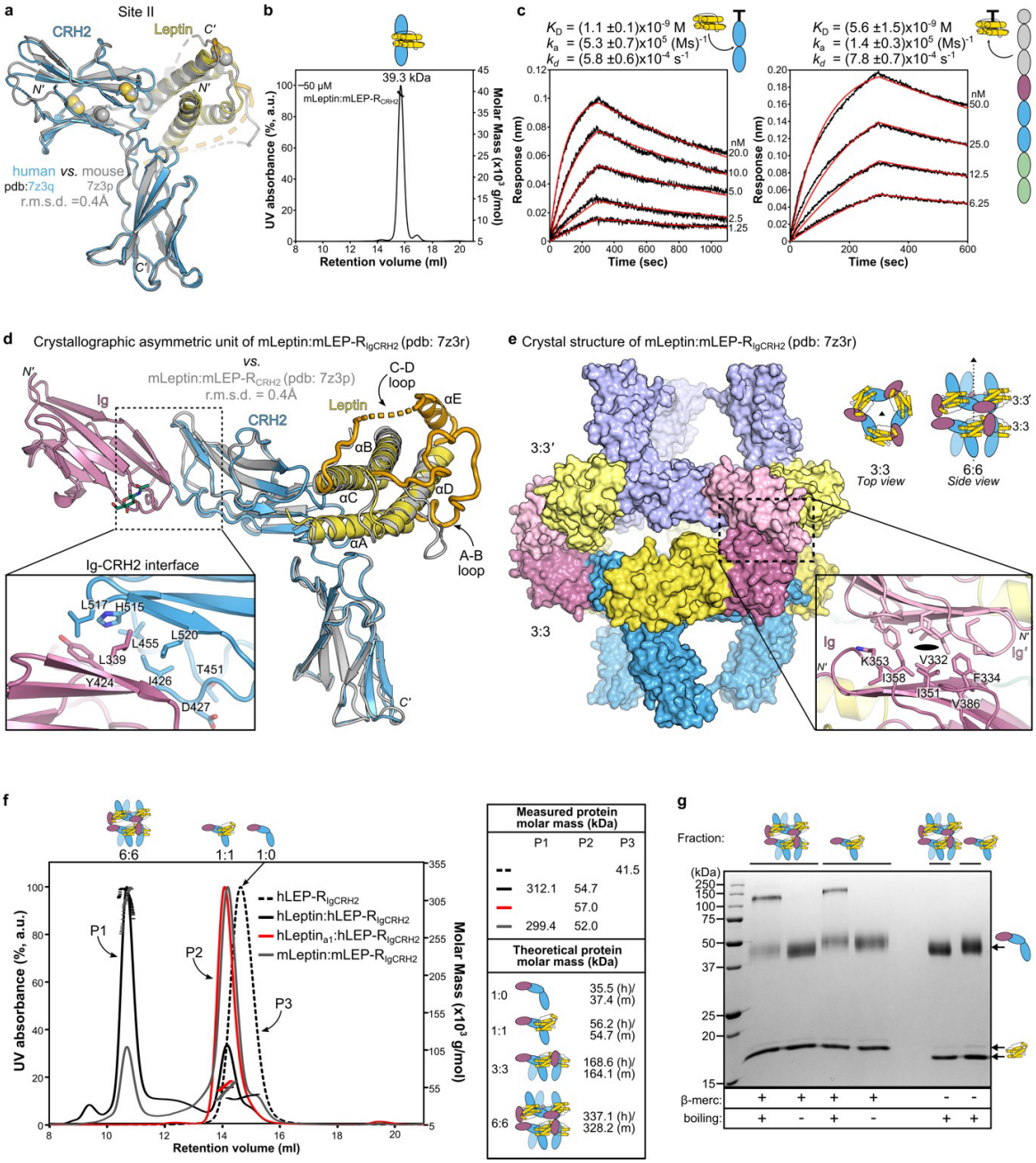

Extended Data Fig. 1: Structural and biophysical characterization of the Leptin:LEP-R assembly. a, a-c, Characterization of the minimal Leptin:LEP-R recognition complex. **a,** Structural superposition of the glycan-trimmed hLeptin:hLEP-R_{CRH2} complex (LEP-R_{CRH2} fragment 428-635 N516Q/C604S in blue; Leptin in yellow) with the mouse complex (colored in gray). The structure of the individual components and the interaction interface thereof is highly similar between the two homologues, consistent with their high sequence identity (83.2% for Leptin, 86.9% for LEP-R_{CRH2}, **Supplementary Fig. 1**). (r.m.s.d.: root mean square deviation of alignment, 161 Cα atoms) **b,** Molar mass determination of the glycan-trimmed mLeptin:mLEP-R_{CRH2} complex using Size Exclusion Chromatography coupled with Multi-Angle Laser Light Scattering (SEC-MALLS). The complex (50 µM) was resolved in a Superdex 200 increase column pre-equilibrated in HBS buffer (20 mM HEPES pH 7.4, 150 mM NaCl). The measured mass (39.3 kDa) approximates the theoretical of 40.3 kDa for 1:1 stoichiometry. *(n=1)* **c,** Biolayer interferometry (BLI) sensograms of the mouse Leptin:LEP-R interaction. Left: mLeptin was titrated, as indicated on the side, against the in vitro biotinylated mLEP-

R_{CRH2} fragment immobilized on Streptavidin sensors *(n = 4)*. Right: mLEP-R_{ECD} was titrated against in vitro biotinylated mLeptin *(n = 3)*. Comparison of the kinetic rates and derived affinities suggest that the high-affinity Leptin:LEP-R interaction is attributed to the Leptin:LEP-R_{CRH2} interface, in agreement with previous studies [1]. **d-g,** Characterization of the mLeptin:LEP-R_{IgCRH2} oligomeric assembly. **d,** The asymmetric unit of the glycan-trimmed mLeptin:mLEP-R_{IgCRH2} crystal structure resolved at 2.9Å (coloured as in Fig. 1a) superimposed to the mLeptin:mLEP-R_{CRH2} structure (grey) (r.m.s.d. of alignment =0.4Å , 257 Cα atoms). Interacting residues at the Ig-CRH2 interface are highlighted in the insert. A glycan chain (green sticks) was resolved at position Asn393 of the LEP-R_{Ig} domain. **e,** The oligomeric assembly of mLeptin:mLEP-R_{IgCRH2} (left) derived from the 3- and 2-fold crystallographic symmetry operations as detailed on the right (space group H 3 2). Symmetry axis are indicated by a triangle and an oval respectively. The assembly comprised of a 3:3 mLeptin:mLEP-R_{IgCRH2} stoichiometric complex through site II and site III contacts, and an artifactual head-to-head dimerization thereof, resulting in a 6:6 complex. The head-to-head dimer associates purely by mirroring Ig-Ig' contacts at an exposed hydrophobic patch shown in the insert. The LEP-R N-terminal domain is expected to disrupt this interface (N-termini indicated). **f,** In solution molar mass determination of LEP-R_{IgCRH2} and complexes thereof with Leptin and the Leptin antagonist a1 (^{140}ST^{141}/AA) [2,3] using SEC-MALLS (Superdex 200 increase column). Protein molar masses are plotted after protein conjugate analysis of the glycosylated complexes. Experimentally determined and theoretical masses are given on the right. h: human; m: mouse complexes. *n=1*. **g,** SDS-PAGE (17%) of isolated 6:6 and 1:1 Leptin:LEP-R_{IgCRH2} complexes under different sample preparation conditions. Multimeric artifacts are observed only with the combination of reduction and boiling, raising awareness for sample preparation for determining stoichiometry from SDS-PAGE. Leptin migrates slower under reducing conditions. (β-merc: β-mercaptoethanol)

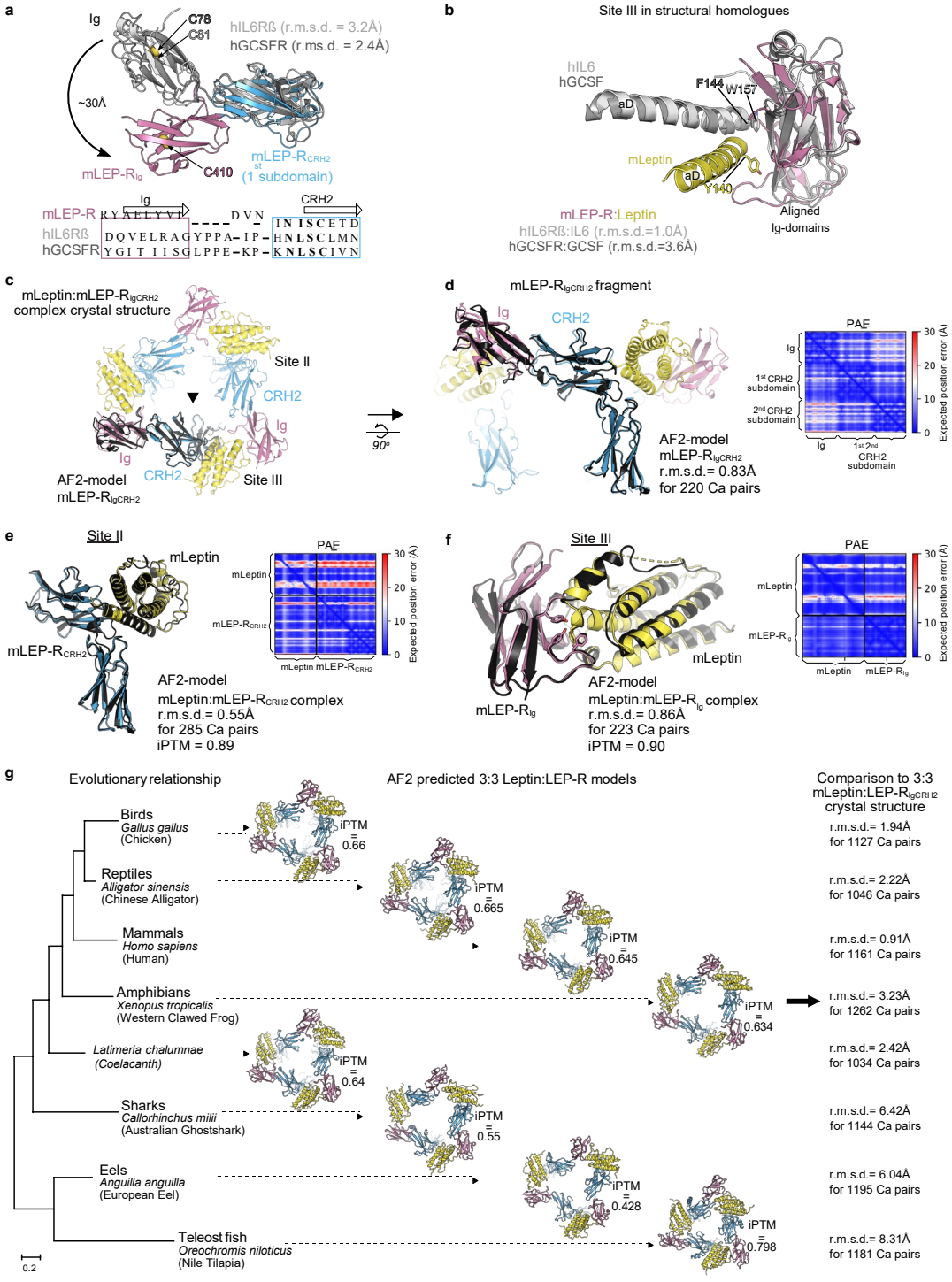

Extended Data Fig. 2: Evolutionary and co-evolutionary features of LEP-R$_{IgCRH2}$ and its interaction interfaces with Leptin. a, Structural superposition (top) and sequence alignment (bottom) of the LEP-R$_{IgCRH2}$ domains with those of human gp130 (IL6Rβ) [4] and GCSFR [5] in their cytokine-bound state (pdb: 1p9m, 2d9q respectively). After alignment at the first subdomain of the CRH2 module (r.m.s.d. indicated; 75 and 60 Cα atoms respectively), the shift distance was determined between the highly conserved cysteine residues of the Ig motif, as indicated. Structure-based sequence alignment was performed using UCSF Chimera and shows a shorter linker between the Ig and CRH2 domains for LEP-R relatively to its structural homologues. **b,** Structural superposition of the site III interface in evolutionary relatives. For visualization purposes only the α-helix D is shown for mLeptin, hIL6 and

hGCSF, featuring the aromatic blueprint of site III in sticks. IL6Rβ:IL6 and GCSFR:GCSF were aligned to the Ig domain of mLeptin:LEP-R_{IgCRH2} (r.m.s.d. indicated; 41 and 59 Cα atoms respectively). **c-f,** Structural superposition of the crystallographically-distilled mLeptin:mLEP-R_{IgCRH2} assembly with AlphaFold models, as indicated, accompanied with predicted Aligned Error plots (PAE) of each prediction. AlphaFold2-ptm was used for the prediction of mLEP-R_{IgCRH2} (panels c-d) and AlphaFold-Multimer (version 2.2) for the prediction of the mLeptin:mLEP-R_{IgCRH2} interaction interfaces (panels e-f). **g,** Evolutionary conservation of the Leptin:LEP-R_{IgCRH2} hexameric assembly across the animal phylogenetic spectrum, tested by AlphaFold-Multimer (version 2.2, with associated ipTM scores) [6,7] with orthologous 3:3 pairings of Leptin and LEP-R sequences harvested from UniProt. Drawing the branching of jawed vertebrates from the coelacanth phylogenetic tree [8], birds are represented by the chicken *G. gallus* Leptin:LEP-R complex (respectively UniProt codes O42164 and Q9I8V6), reptiles by the alligator *A. sinensis* (A0A1U8DFZ0 and A0A3Q0H8E2), mammals by human *H. sapiens* (P41159 and P48357), amphibians by *X. tropicalis* (A0A803KEF7 and F6RVW6), lobe-finned fishes by the living fossil *Coelacanth L. chalumnae* (H3AP27 and H3AG22), cartilaginous fishes by the Australian ghostshark *C. milii* (A0A4W3H871 and V9KNM1), and ray-finned fishes by the eel *A. anguilla* (A0A0C7AV37 and A0A0C7AV33) and tilapia *O. niloticus* (I3KCE8 and A0A067Z8Z1). Sequence evolutionary relationships were based on LEP_R orthologues and were adapted from Londraville et al., 2017 [9]. Complexes were visualized and superposed to the X-ray structure of mLeptin:mLEP-R_{IgCRH2} by PyMOL 2.3.4 (www.pymol.org) with listed r.m.s.d fit to the 3:3 complex.

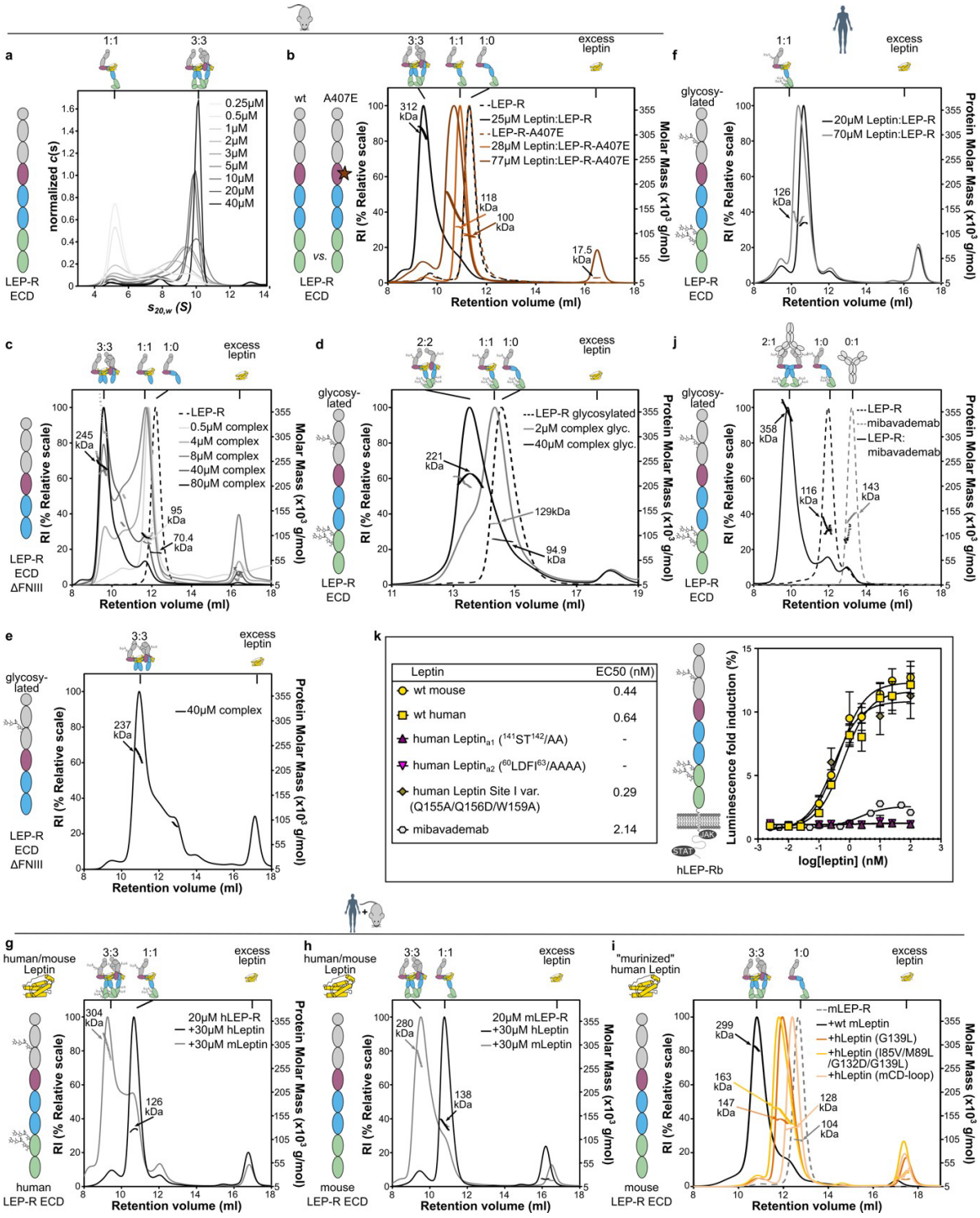

Extended Data Fig. 3: Biophysical and functional characterization of LEP-R complexes. a-e, Biophysical analysis of mouse Leptin:LEP-R_{ECD} in solution. **a,** Sedimentation coefficient distributions c(s) for different concentrations of glycan-trimmed mLeptin:mLEP-R_{ECD}. **b,** SEC-MALLS analysis (Superdex 200 increase column) of glycan-trimmed wild type mLEP-R_{ECD} and mLEP-R_{ECD}-A407 mutant and their complexes with mLeptin. Similar results were obtained from at least 3 independent repetitions. **c and e,** SEC-MALLS analysis (Superdex 200 increase column) of glycan-trimmed (panel c) or glycosylated (panel e) mLEP-$R_{ECD\text{-}\Delta FNIII}$ and their complexes with mLeptin. Similar results were obtained from *n=2* at selected similar concentrations for panel c, *n=3* for panel e. **d,** SEC-MALLS analysis (Superose 6 increase column) of glycosylated mLEP-R_{ECD} and its complexes with mLeptin, as a function of complex concentration. Similar results were obtained from at least *n=2* independent

experiments at a range of concentrations. **f, j, k,** Characterization of human LEP-R complexes. **f,** SEC-MALLS analysis (Superdex 200 increase column) of glycosylated hLEP-R_{ECD} and its complexes with hLeptin. Similar results were obtained from *n=2* independent experiments at selected concentrations. **j,** SEC-MALLS analysis (Superdex 200 increase column) of glycosylated hLEP-R_{ECD} and its complexes with the agonistic antibody mibavademab[10]. *n=1.* **k,** Activation of hLEP-Rb by Leptin and variants, as well as by the agonistic antibody mibavademab, probed by a STAT3-responsive luciferase reporter in HEK293T cells. *n=3* independent experiments with 3 technical replicates each. Here, mean values and standard deviations from a representative independent experiment are shown. **g, h, i,** Interspecies cross-reactivity probed with SEC-MALLS (Superdex 200 increase column). *n=1.* **g,** Complexes of hLEP-R_{ECD} with mouse and human Leptin. **h,** Complexes of glycan-trimmed mLEP-R_{ECD} with mouse and human Leptin. **i,** Complexes of glycan-trimmed mLEP-R_{ECD} with "murinized" human Leptin. Specifically, residues close to the Site III interface that differ between mouse and human Leptin (**Supplementary Fig. 1a**) were mutated on hLeptin to the corresponding of the mouse homologue (i.e. CD-loop residues 118-129; G139L; I85V/M89L/G132D/G139L).

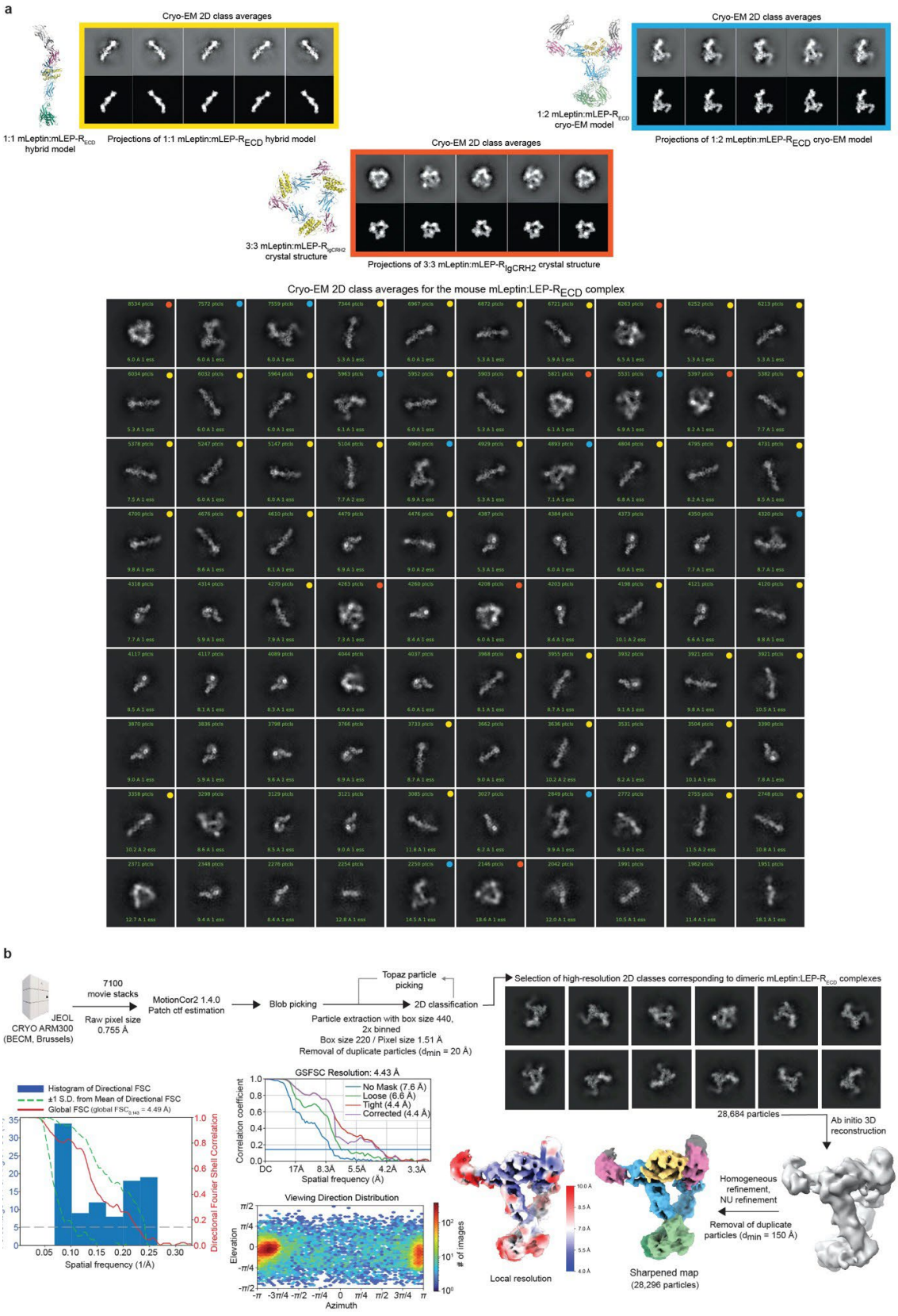

Extended Data Fig. 4: Cryo-EM analysis of mLep:mLEP-R$_{ECD}$ complexes. a. The COSMIC[2] webserver was used to align projections of the trimeric mLeptin:mLEP-R$_{IgCRH2}$ crystal structure, the 1:2

mLeptin:LEP-$R_{IgCRH2FnIII}$ cryo-EM model, and projections of a 1:1 mLeptin:mLEP-R_{ECD} model (based on the Alphafold2-model for mLEP-R_{ECD} and the mLeptin:mLEP-R_{CRH2} crystal structure) with high-resolution 2D-classes obtained for the mLeptin:mLEP-R_{ECD} complex sample. In the gallery 2D cryo-EM classes matching projections are indicated with a colored dot. **b**, Cryo-EM workflow towards the reconstruction of the 1:2 mLeptin:LEP-R_{ECD} complex. We note that 3D reconstruction of the remaining two observed states was hindered due to preferred orientation.

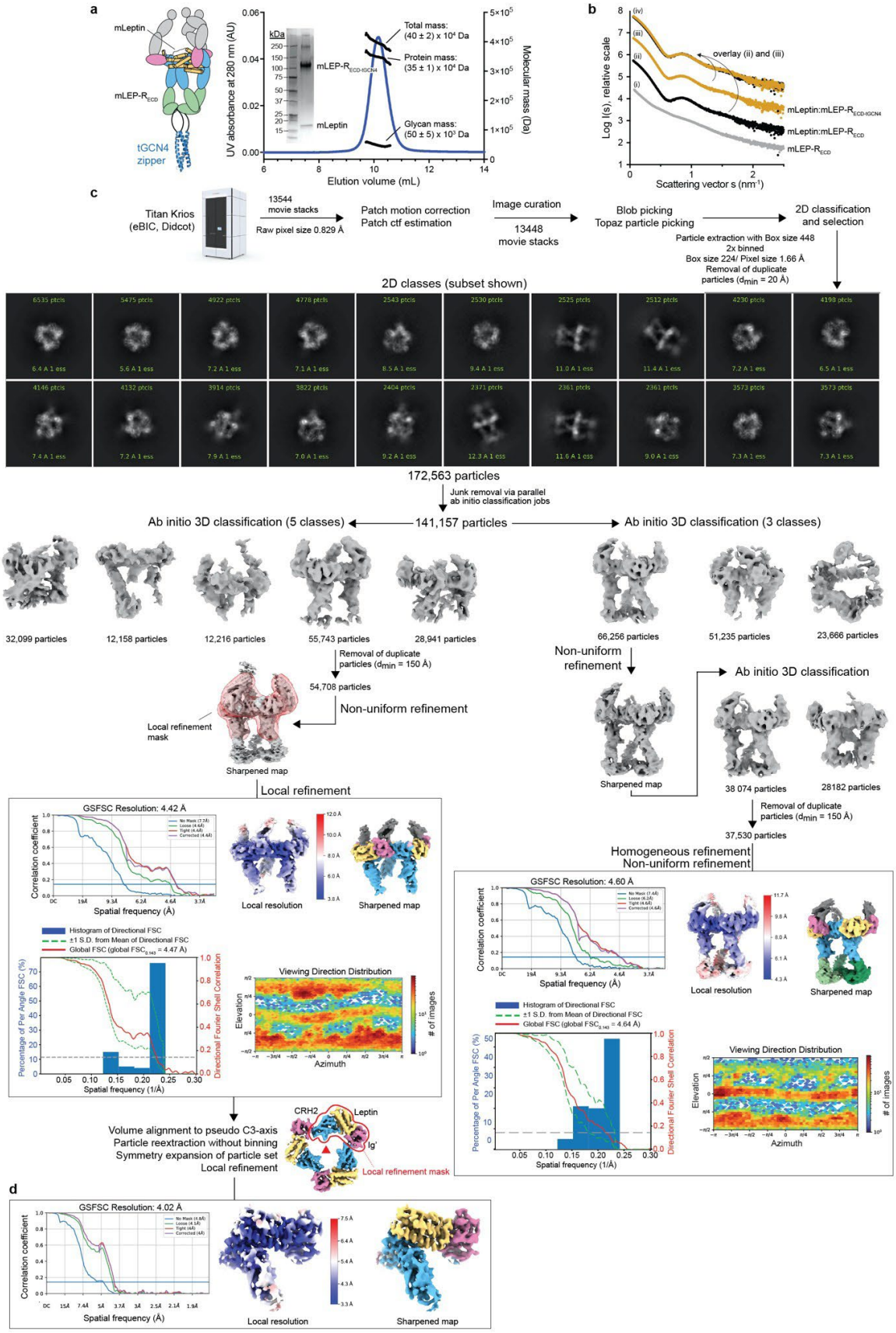

Extended Data Fig. 5: Cryo-EM data analysis workflow for the mLeptin:mLEP-R$_{tGCN4}$ complex. **a,** SEC-MALLS analysis of the glycosylated mLeptin:mLEP-R$_{ECD-tGCN4}$ complex. The SEC-elution

profile is plotted as the ultraviolet absorbance at 280 nm (left Y-axis) in function of elution volume. The total, protein and glycan molecular mass (right Y-axis) as determined by MALLS are reported as the average molecular mass (and s.d.) across the elution peak. Number of samples for mLeptin:mLEP-$R_{ECD\text{-}tGCN4}$ analyzed: *n=1.* **b,** SAXS scattering curves of EndoH-treated samples for mLEP-R_{ECD} and mLeptin:mLEP-R_{ECD} complexes plotted as the scattered intensity in function of scattering vector $s = 4\pi\sin\theta/\lambda$. *(i)* mLEP-$R_{ECD}$ (grey), (*ii*) non-stabilized mLeptin:mLEP-R_{ECD} complex (black), (*iii*) stabilized mLeptin:mLEP-$R_{ECD\text{-}tGCN4}$ complex (yellow), *(iv)* scaled and overlayed scattering profiles for mLeptin:mLEP-R_{ECD} and mLeptin:mLEP-$R_{ECD\text{-}tGCN4}$. Similar results were obtained from *n=2* independent experiments for mLeptin:mLEP-R_{ECD}. For the rest *n=1*. **c.** Cryo-EM data processing workflow in cryoSPARC for the glycosylated mLeptin:mLEP-RECD-$_{ECD\text{-}tGCN4}$ complex. NU: non-uniform refinement.

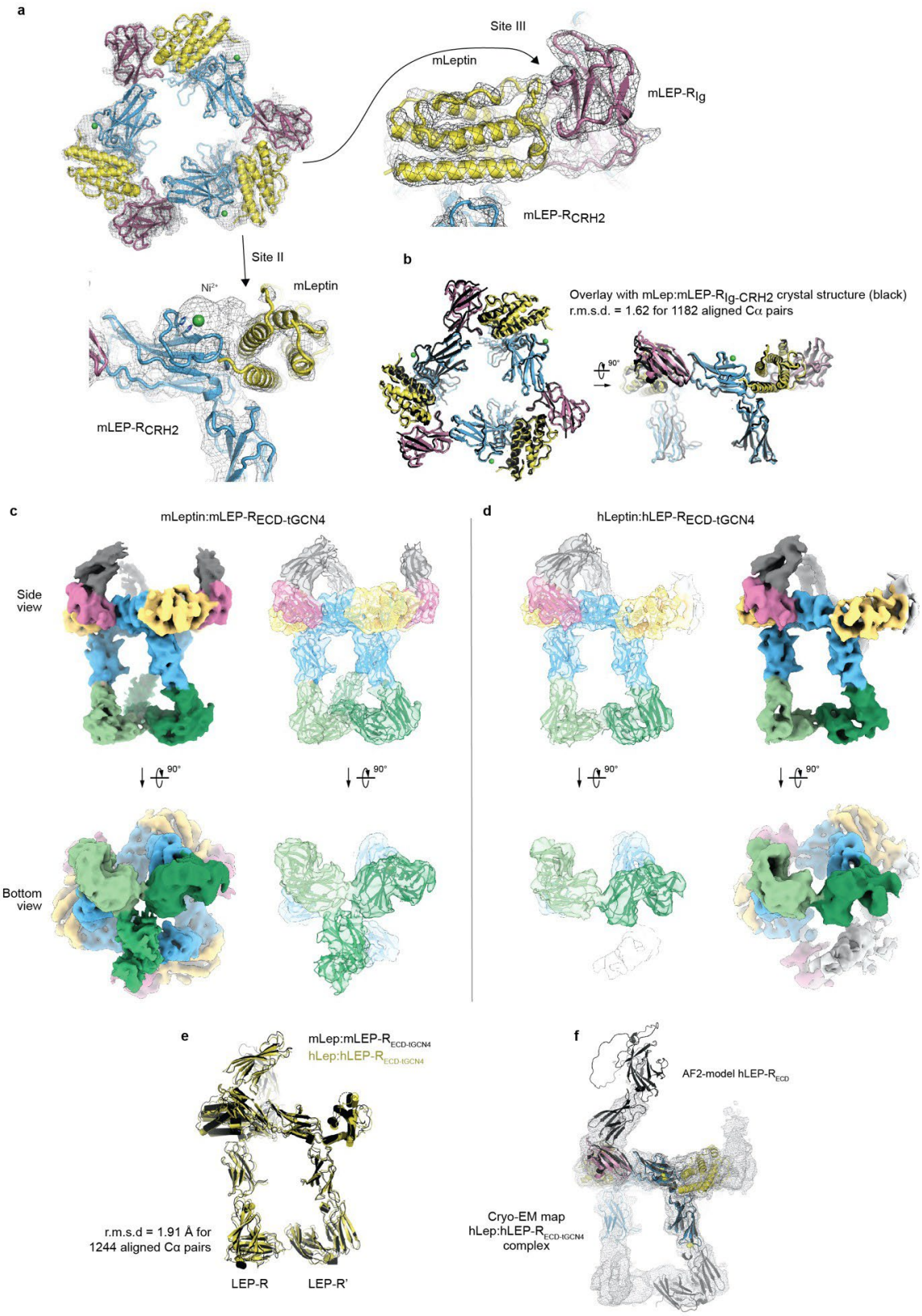

Extended Data Fig. 6: Comparative analysis between mouse and human Leptin:LEP-R complex structures as derived from Cryo-EM and X-ray crystallographic analysis. a, Real-space refined atomic model for the trimeric mLeptin:mLEP-R_{IgCRH2} core region overlayed with the sharpened cryo-

EM map in C1 symmetry for the mLeptin:mLEP-$R_{ECD\text{-}tGCN4}$ complex following local map refinement. The cryo-EM map is contoured at 0.313 V. In the cryo-EM map strong additional density is observed at all three LEP-R_{CRH2}:Leptin interface regions (site II) that likely corresponds to a trapped Ni-ion coordinated by histidine residues in the LEP-R_{CRH2} module and the N-terminal His-tag present on mLeptin. **b,** Structural superposition of the crystallographically-distilled 3:3 mLeptin:mLEP-R_{IgCRH2} assembly (black) with the real-space refined mLeptin:mLEP-R_{IgCRH2} assembly via cryo-EM. **c-d,** Cryo-EM maps and fitted atomic models for the mouse and human Leptin:LEP-$R_{ECD\text{-}tGCN4}$ complexes. The sharpened cryo-EM maps are colored per zone with Leptin in yellow, the CRH1 module in grey, the Ig domain in magenta, the CRH2 module in blue and the FnIII module in green. The fitted atomic model models are shown as a cartoon overlayed with the cryo-EM maps as a transparent volume. The mouse and human cryo-EM maps are contoured at 0.178 V and 0.550 V, respectively. **e**, Structural superposition of the real-space refined atomic models for the mouse and human Leptin:LEP-$R_{ECD\text{-}tGCN4}$ complexes. **f**, Structural superposition of the real-space refined model for the hLeptin:hLEP-R_{IgCRH2} core with the structural prediction for hLEP-R_{ECD} via AlphaFold2 overlayed with the sharpened cryo-EM map for the hLeptin:hLEP-$R_{ECD\text{-}tGCN4}$ complex.

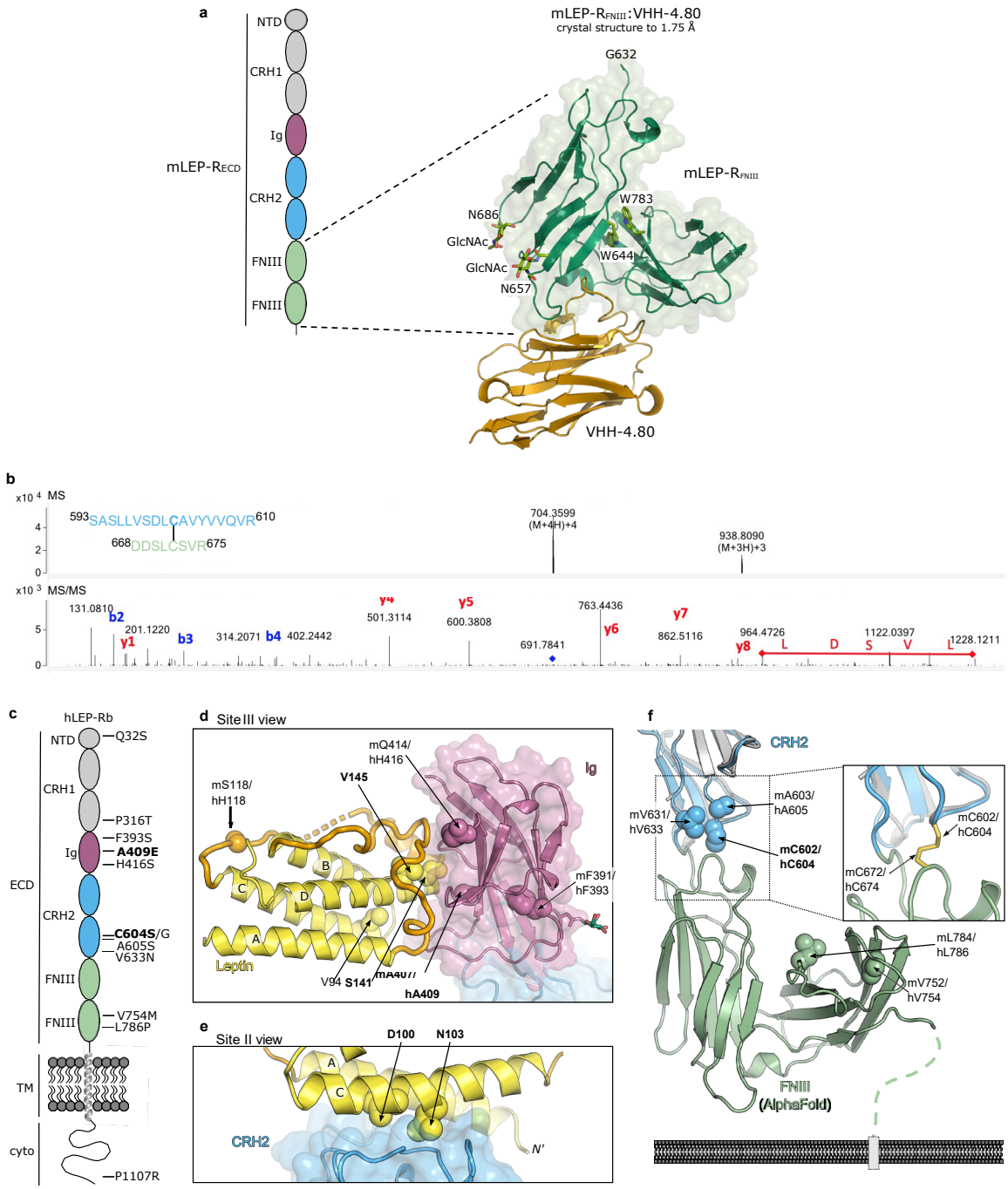

Extended Data Fig. 7: Structural insights into the mLEP-R$_{FNIII}$ conformation and map of naturally occurring mutations likely related to obesity on the Leptin:receptor assembly. a, Cartoon representation of the determined crystal structure of for mLEP-R$_{FnIII}$:VHH-4.80 complex. Evolutionary conserved Trp across the interdomain interface and crystallographically observed N-linked glycosylation sites are shown as sticks. **b,** Mass spectrometric confirmation of the disulfide bridge between residues Cys602-Cys672 of the CRH2 and FNIII domains respectively in mLEP-R$_{ECD}$. The MS (top) and MS/MS spectra (bottom) are shown for the disulfide-linked peptides that are indicated on the left. **c-f**, Map of naturally occurring mutations likely related to obesity on the Leptin:receptor assembly. **c**, Domain distribution of missense variants identified in the human LEP-R gene of obese individuals (**Supplementary Table 1**), that have no currently known effect on protein secretion and

stability. Functionally validated pathogenic mutations are highlighted in bold. **d-e,** Localization of mutations in the LEP and LEP-R genes (**Supplementary Table 1**) in the assembly. Mutated residues are shown as spheres. Functionally validated pathogenic mutations are highlighted in bold. **f,** Structural superposition of the crystallographically-resolved hLEP-R_{CRH2} domain (gray) with the AlphaFold model of hLEP-R (r.m.s.d.=0.669Å, 171 Cα atoms). Residues found in variants likely related to obesity are annotated. A disulfide bridge is predicted to be formed between the CRH2 and FNIII domains (Cys604-Cys674), as shown in the insert. Both residues are functionally important [11,12]. The disulfide bridge was confirmed by peptide mapping for mLEP-R_{ECD}, as shown in panel b. Cysteine 602 (604 in human) was mutated to serine in FNIII-deletion permutations of LEP-R in this study to prevent artificial disulfide-linked clusters.

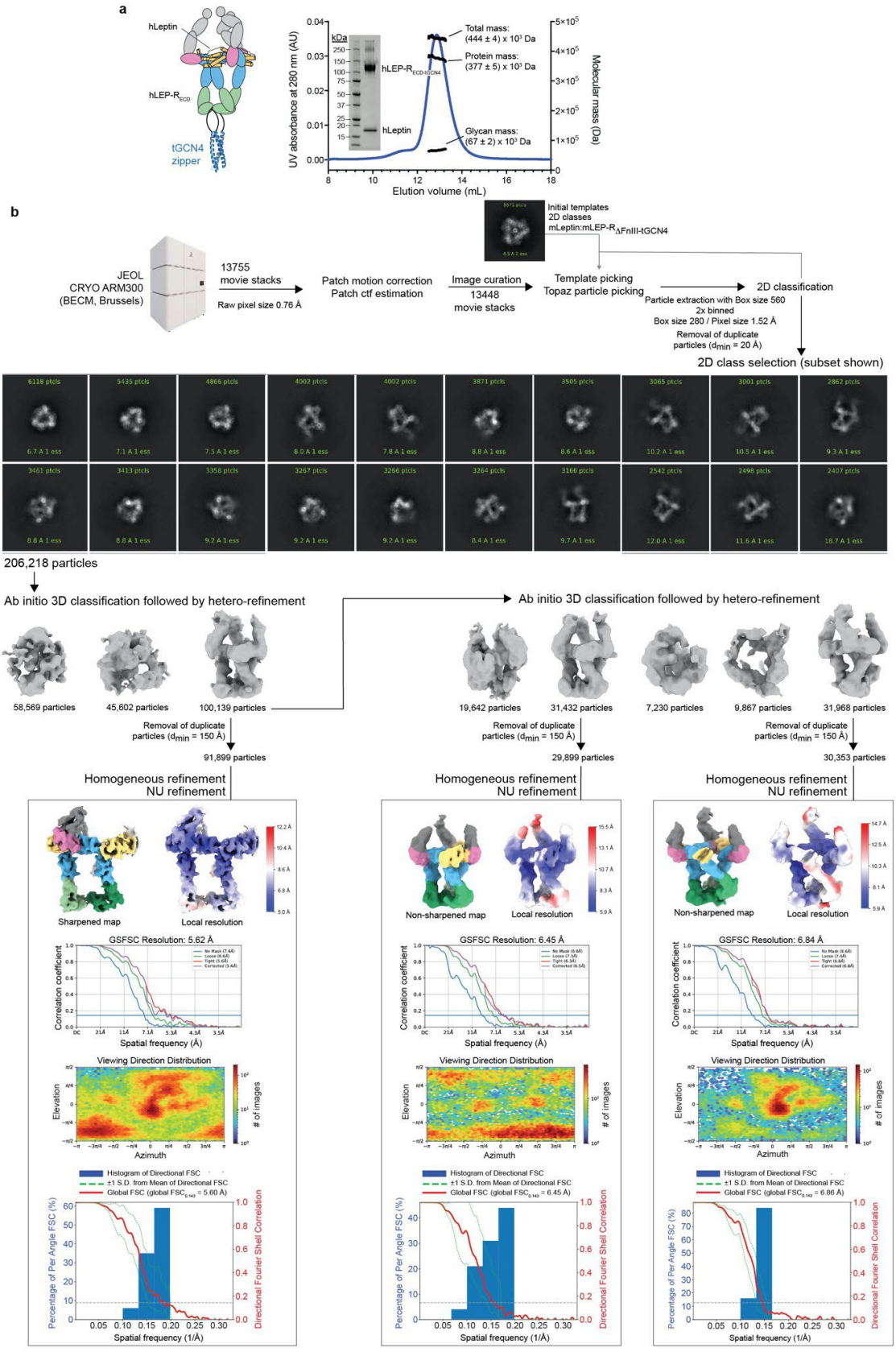

Extended Data Fig. 8: Cryo-EM data analysis workflow for the hLeptin:hLEP-R$_{tGCN4}$ complex. **a,** SEC-MALLS analysis of the glycosylated hLeptin:hLEP-R$_{ECD-tGCN4}$ complex. The SEC-elution

profile is plotted as the ultraviolet absorbance at 280 nm (left Y-axis) in function of elution volume. The total, protein and glycan molecular mass (right Y-axis) as determined by MALLS are reported as the average molecular mass (and s.d.) across the elution peak. Number of samples for hLeptin:hLEP-$R_{ECD\text{-}tGCN4}$ analyzed: *n=1*. **b,** Cryo-EM data processing workflow in cryoSPARC for the glycosylated hLeptin:hLEP-$R_{ECD\text{-}tGCN4}$ complex. NU: non-uniform refinement.

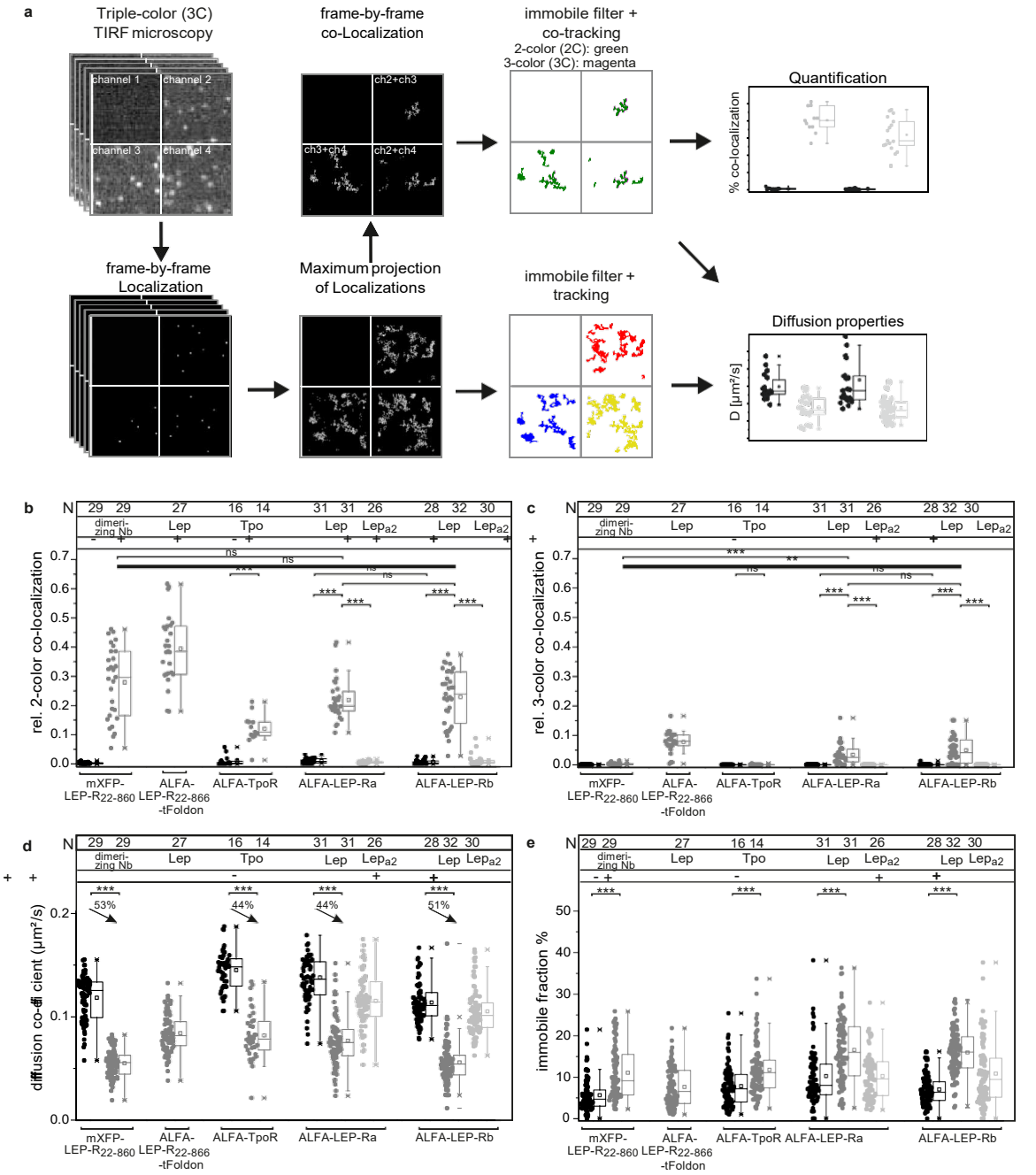

Extended Data Fig. 9: Receptor co-localization at the cell surface probed by smTIRFM. a, Schematic overview of single molecule tracking and data evaluation. **b,** Dual-color (2C) co-tracking. **c,** Triple-color (3C) co-tracking. **d,** Diffusion properties; arrows indicate percentage of diffusional decrease **e,** fraction of immobilized emitters. For **b-e,** the number of cells (N) examined over n=2 independent experiments for all LepR experiments, and n=1 control experiment for TpoR, is indicated in the top row. Statistical differences were calculated with two-tailed two-sample Kolmogorov-Smirnov tests (**P ≤ 0.01, ***P ≤ 0.001; ns: not significant). Exact P-values for each comparison are given in the source data file of **Fig. 6**. Box and whisker plots show the five number summaries of the data: minimum, first quartile, median, third quartile, and maximum values. Outliers are indicated with an asterisk.

Captions for Supplementary Videos:

Supplementary Video 1: mLep:mLEP-Rb assembly in living cells
Co-localization of mLEP-Rb in the absence (left) and presence of ligand (middle: 2-color co-localization; right: 3-color co-localization, 10 nM mLeptin, 10 min). green, red and blue signals correspond to receptors labeled with ^{Cy3B}NB, ^{Atto643}NB, and ^{Dy752}NB, respectively. Out-of-focus immobile signals observed in the presence of mLeptin can be explained by membrane-proximal endosomes. Acquisition frame rate: 33 Hz, Playback: real time.

Supplementary Video 2: mLep:mLEP-RΔ866-tFoldon assembly in living cells
Co-localization of mLEP-RΔ866-tFoldon in presence of ligand (left: 2-color co-localization; right: 3-color co-localization, 10 nM mLeptin, 10 min). green, red and blue signals correspond to receptors labeled with ^{Cy3B}NB, ^{Atto643}NB, and ^{Dy752}NB, respectively. Acquisition frame rate: 33 Hz, Playback: real time.

Supplementary Information

Table of contents:

Supplementary Figures:

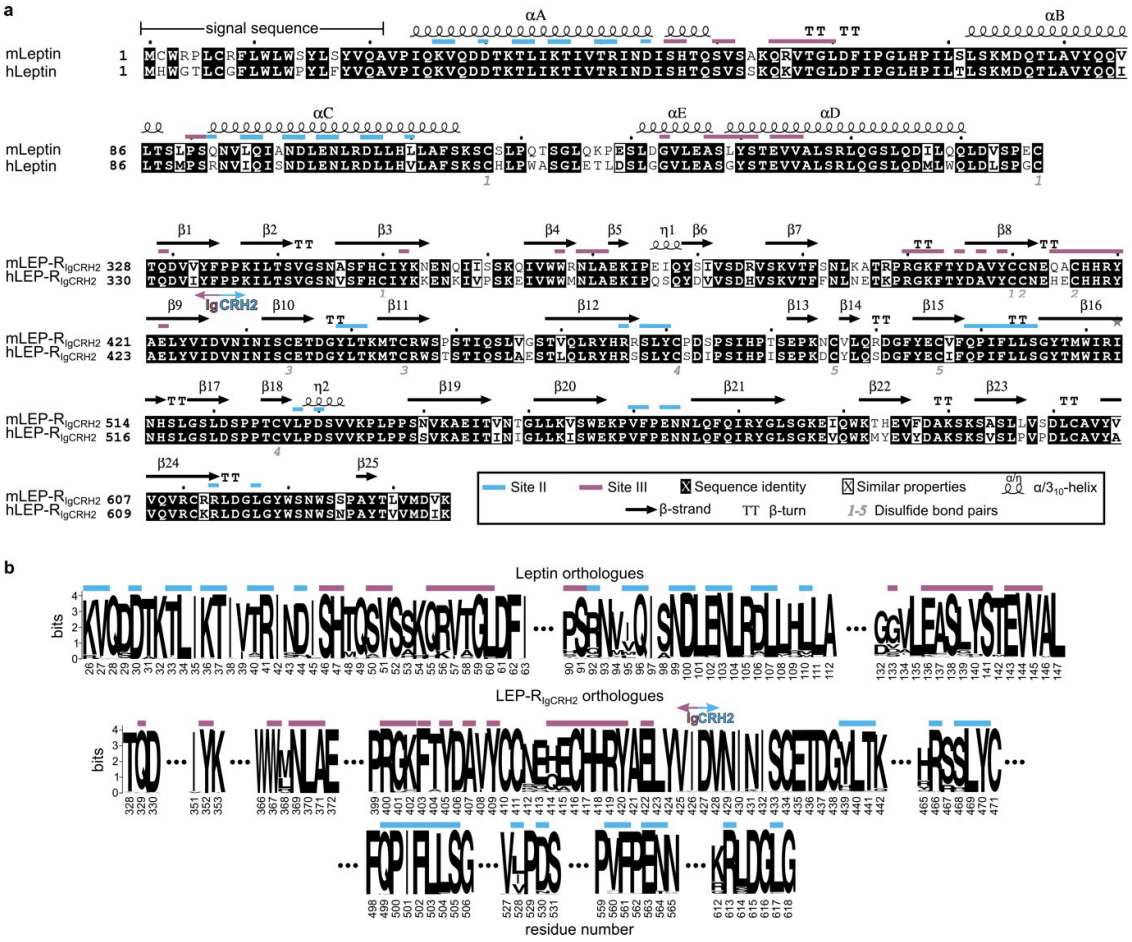

Supplementary Fig. 1: Sequence conservation of Leptin and mLEP-R$_{IgCRH2}$. a, Structurally annotated sequence alignment of mouse with human Leptin (top) and LEP-R$_{IgCRH2}$ fragment (bottom) using ClustalOmega and the ESPript server (http://espript.ibcp.fr/). Site II and III interface residues are highlighted accordingly. Secondary structure elements and disulfide bonds were derived from the crystal structure of the mLeptin:mLEP-R$_{IgCRH2}$ complex determined in this study. **b,** Conservation of the site II and III interface in Leptin and LEP-R orthologues in mammals. Sequence logos were generated using the Weblogo server (http://weblogo.berkeley.edu/logo.cgi) after ClustalOmega multiple sequence alignment of 82 and 73 Leptin and LEP-R orthologues respectively, derived from the Ensembl database (https://www.ensembl.org/index.html). Not fully sequenced orthologues and those not initiating with a Methionine residue were excluded. Interface residues are highlighted as in panel a.

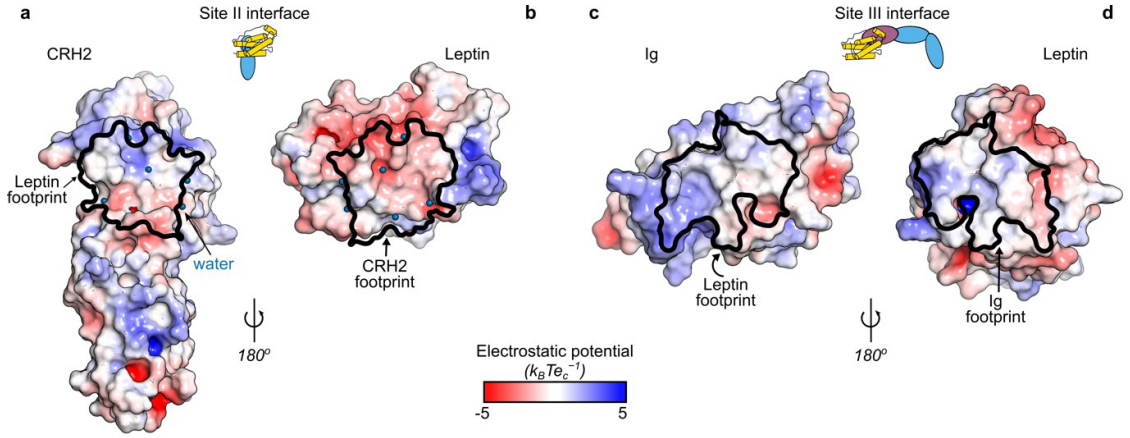

e

f

mLeptin:mLEP-R_{CRH2} (PDB: 7z3p)
Interaction site II

LEP-R_{CRH2} Chain B	Leptin Chain A	Bridging water Chain W	Distance (Å)
Salt bridges			
ARG 466[NH2]	GLU 102[OE2]		3.6
Hydrogren bonds			
TYR 439[O]	ARG 41[NH1]		3.2
LEU 440[O]	ARG 41[NH1]		3.1
LEU 440[O]	ARG 41[NH2]		3.0
SER 468[O]	ASN 103[ND2]		3.6
TYR 470[OH]	ASP 30[OD2]		2.6
ILE 501[N]	GLN 96[OE1]		3.0
ILE 501[O]	GLN 96[NE2]		2.9
ILE 501[O]	ASN 99[ND2]		3.2
LEU 503[N]	ASN 103[OD1]		3.3
LEU 504[N]	ASN 103[OD1]		3.0
SER 505[OG]	ASN 103[ND2]		3.3
GLU 563[OE2]	THR 40[OG1]		2.6
SER 468[O]	ASP 106[OD2]	HOH 4	2.7 / 2.5
//	ASN 103[ND2]	//	2.8
//	GLU 102[O]	//	3.6
GLU 563[N]	THR 37[OG1]	HOH 9	2.9 / 2.8
ASP 530[OD2]	LYS 26[NZ]	HOH 12	2.6 / 2.9
ARG 613[NH2]	//	//	3.1
ARG 613[NH1]	//	//	3.2
LEU 503[N]	ASP 100[OD1]	HOH 20	2.9 / 2.6
//	ASN 103[OD2]	//	2.8
TYR 439[O]	ARG 41[NH1]	HOH 28	2.9 / 2.9
THR 441[O]	GLN 96[OE1]	HOH 29	2.7 / 2.6
van der Waals contacts (numerical order)			
THR 441	LYS 26		
LEU 469	VAL 27		
GLN 499	THR 33		
PRO 500	LEU 34		
PHE 502	LYS 36		
LEU 528	THR 37		
ASP 530	ASP 44		
VAL 560	GLN 92		
PHE 561	LEU 95		
ASN 564	ASP 100		
ARG 613	ASP 106		
LEU 617	LEU 107		
	LEU 110		

mLeptin:mLEP-R_{IgCRH2} (PDB: 7z3r)
Interaction site III

LEP-R_{IgCRH2} Chain B	Leptin Chain A	Distance (Å)
Salt bridges		
Hydrogren bonds		
TYR 352[OH]	THR 58[OG1]	3.9
ASN 369[O]	TYR 140[OH]	3.8
TYR 409[OH]	SER 141[OG]	2.7
GLN 414[O]	GLN 55[NE2]	2.9
CYS 416[N]	ARG 56[O]	3.5
CYS 416[O]	THR 58[N]	2.9
CYS 416[O]	THR 58[OG1]	3.2
HIS418[N]	THR 58[O]	3.3
HIS 418[ND1]	SER 138[OG]	2.8
HIS 418[O]	SER 141[OG]	2.7
TYR 420[OH]	LEU 139[N]	3.2
TYR 420[OH]	TYR 140[N]	3.0
van der Waals contacts (numerical order)		
GLN 329	SER 46	
TRP 367	HIS 47	
LEU 370	SER 50	
ALA 371	VAL 51	
ARG 400	VAL 57	
GLY 401	GLY 59	
LYS 402	LEU 60	
PHE 403	PRO 90	
TYR 405	SER 91	
ALA 407	VAL 134	
ALA 415	ALA 137	
HIS 417	GLU 143	
ARG 419	VAL 144	
	VAL 145	

Supplementary Fig. 2: Analysis of the site II and III mLeptin:mLEP-R interfaces. a-b, Site II interface footprint on mLEP-R_{CRH2} (a) and mLeptin (b) mapped on an electrostatic potential-gradient surface representation of the individual components of the mLeptin:mLEP-R_{CRH2} complex. **c-d,** Site III interface footprint on mLEP-R_{Ig} (c) and mLeptin (d), as in a-b, in the mLeptin:mLEP-R_{IgCRH2} assembly. **e-f,** Site II (e) and Site III (f) interacting residues in the mLeptin:mLEP-$R_{(Ig)CRH2}$ complexes as determined by the PISA server (https://www.ebi.ac.uk/msd-srv/prot_int/pistart.html) and manual validation.

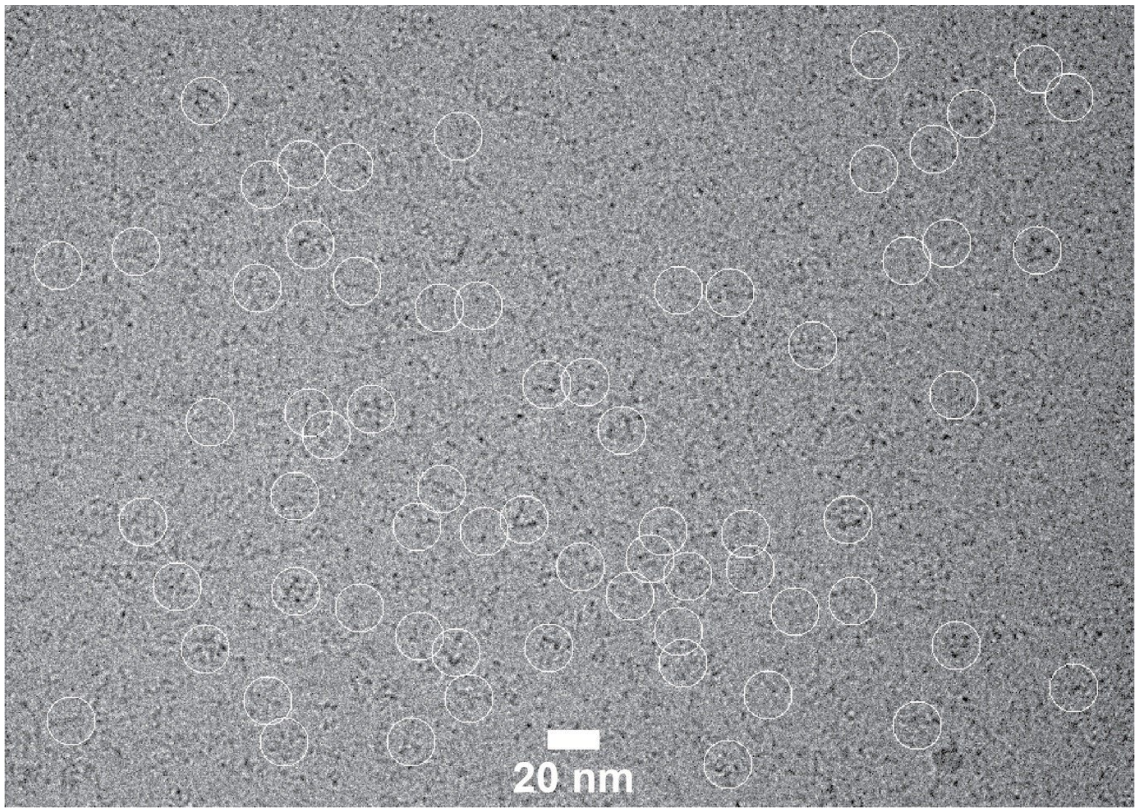

Supplementary Fig. 3: Cryo-EM image for the mLeptin:mLEP-R_{ECD} complex. Picked particles are encircled. The bottom scale bar is 20 nm.

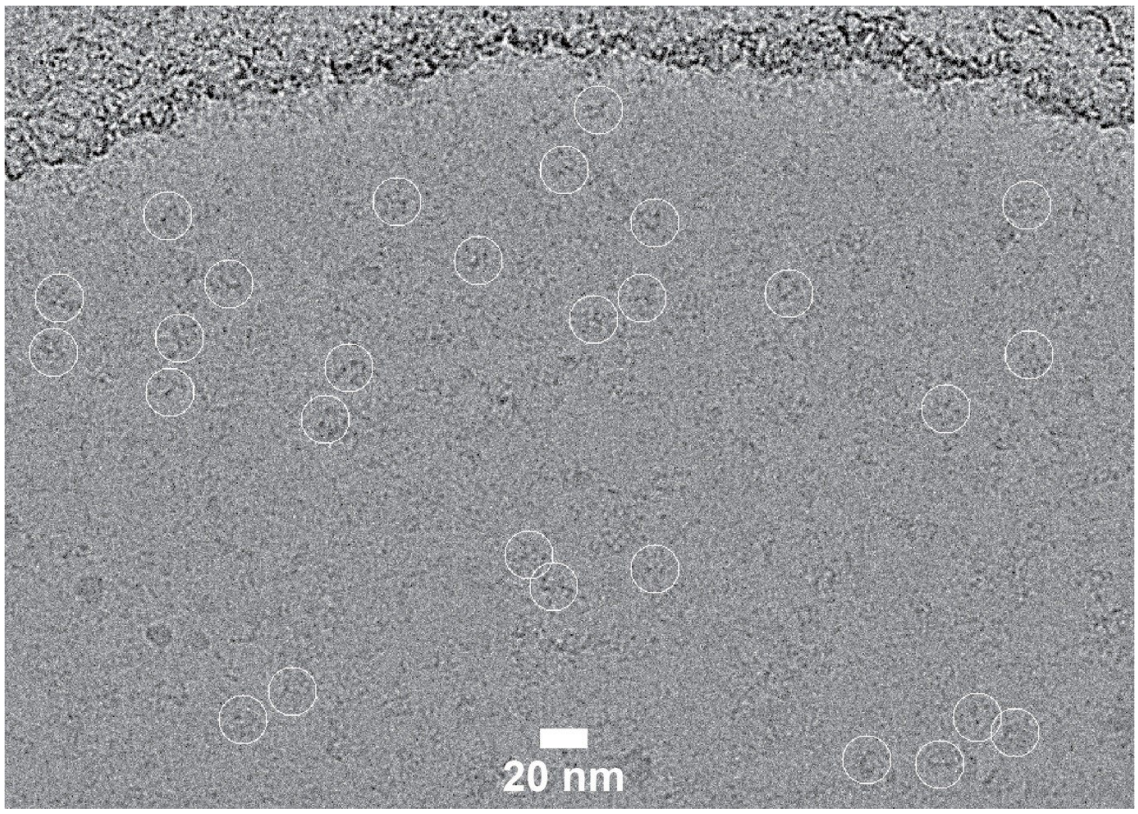

Supplementary Fig. 4: Cryo-EM image for the stabilized mLeptin:mLEP-$R_{ECD\text{-}tGCN4}$ complex. Picked particles are encircled. The bottom scale bar is 20 nm.

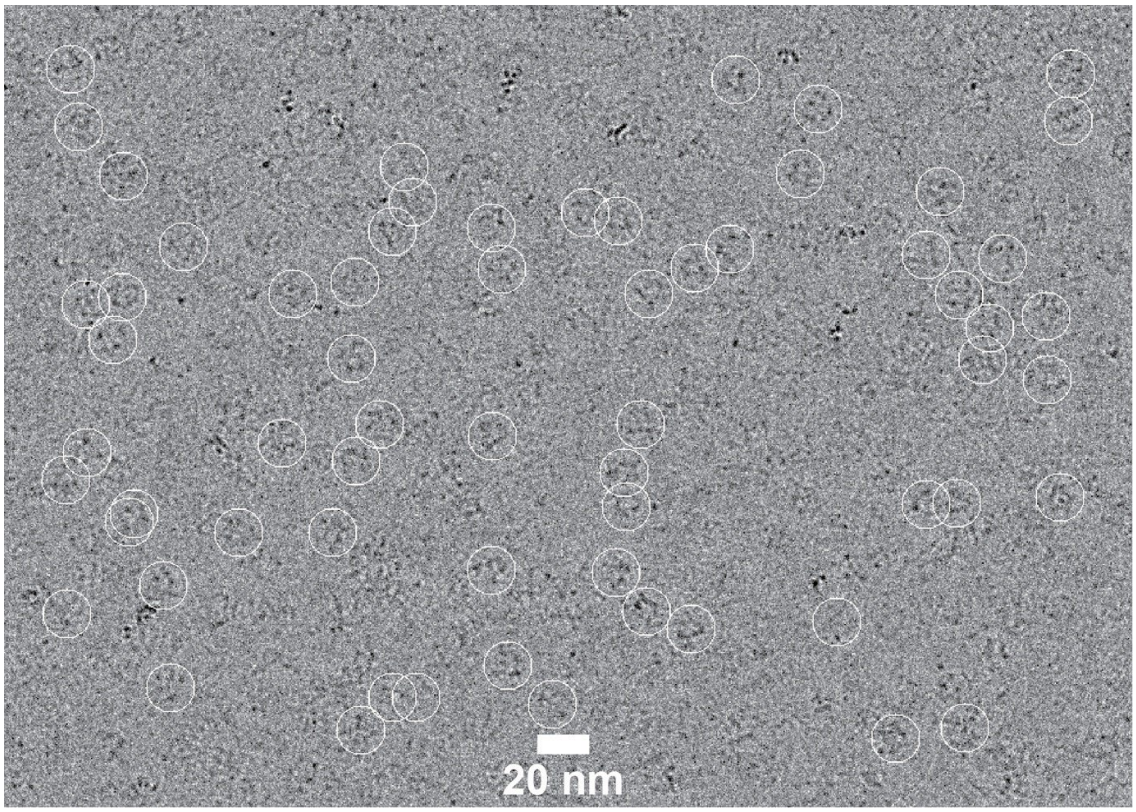

Supplementary Fig. 5: Cryo-EM image for the stabilized hLeptin:hLEP-R$_{ECD\text{-}tGCN4}$ complex. Picked particles are encircled. The bottom scale bar is 20 nm.

Supplementary Tables:

Supplementary Table 1| Missense mutations in obese individuals with no apparent/currently known effect in protein secretion and stability. Pathogenic mutations with known impaired expression/secretion/stability [13-15] were excluded from this list and were recently detailed in *refs*[16,17]. As functional validation of most mutations is yet to be provided, the *in silico* prediction of the pathogenicity level using Sorting Intolerant From Tolerant (SIFT) [18] program is given.

Organism	Protein variant	Secretion/ surface exposure	Binding	SIFT pathogenicity	Residue conservation	Reference
Leptin						
Human	F17L[a]	yes	n.d.	tolerated	no	[19]
	V94M	n.d.	n.d.	tolerated	moderately	[20]
	D100Y	yes	no	deleterious	yes	[21]
	N103K	yes	no	deleterious	yes	[22,23]
	H118L	n.d.	n.d.	deleterious	no	[24]
	S141C[b]	n.d.	n.d.		yes	[25]
Mouse	V145E	yes	yes		yes	[26]
LEP-R						
Human	Q4H[a]	n.d.	n.d.	deleterious	yes	[27]
	R32S	n.d.	n.d.	tolerated	yes	[20]
	P316T	n.d.	n.d.	deleterious	moderately	[28]
	F393S	n.d.	n.d.	deleterious	yes	[20]
	A409E	yes[14]	yes[14]	deleterious	yes	[29]
	H416S	n.d.	n.d.	tolerated	moderately (H/R/Q)	[20]
	C604S[c]/G	n.d. /n.d.	n.d. /n.d.	deleterious/ deleterious	yes	[30,31]
	A605S	n.d.	n.d.	deleterious	yes	[20]
	V633N	n.d.	n.d.	deleterious	yes	[32]
	V754M	n.d.	n.d.	deleterious	yes	[20]
	L786P	n.d.	n.d.	deleterious	yes	[31]
	P1107R	n.d.	n.d.	tolerated	no	[20]

[a] Mutation located in signal sequence.

[b] Although, to our knowledge, the particular mutation has not been functionally investigated, the essential role of the residue in signaling has been confirmed by the double mutation ^{141}ST^{142}/AA (ref[3,33]).

[c] Variant was significantly impaired in signaling [11] in the mouse homologue (Cys602). This was attributed to disruption of the potential Cys602-Cys672 disulfide bridge between the CRH2 and FNIII domains [11,34]. The pairing residue Cys672 was also found to be important for signaling [12]. The Cys602-Cys672 (Cys604-Cys674 in human) disulfide bridge is predicted to be formed in the Alphafold models of LEP-R (**Extended Data Fig. 7f**), and was experimentally confirmed in this study (**Extended Data Fig. 7b**).

Supplementary Table 2| List of protein expression constructs used in this study. In all cases, sequence numbering corresponds to the Uniprot annotated sequences, as indicated.

Protein (segment)	Gene corner accession code	Construct	Expression system	Application
Mouse LEP-R_{CRH2} (426-633; N514Q/C602S)	LMBP 13462	594_pCAGGS_ss_His_TEV_mCHR2*	FreeStyle™ 293-F	X-ray crystallography (mLeptin:mLEP-R_{CRH2} assembly), SEC-MALS (Ext. Data Fig. 1b)
Mouse Leptin wt (22-167)	LMBP 13463	586_pTwist_ss_His_mLEP	FreeStyle™ 293-F	X-ray crystallography (mLeptin:mLEP-R_{CRH2} assembly), SEC-MALS (Ext. Data Fig. 1f)
Human LEP-R_{CRH2} (428-635; N516Q/C604S)	LMBP 13464	591_pCAGGS_ss_His_TEV_hCHR2*	FreeStyle™ 293-F	X-ray crystallography (hLeptin:hLEP-R_{CRH2} assembly), SEC-MALS
Human Leptin wt (22-167)	LMBP 13465	556_pTwist_ss_His_TEV_hLeptin	FreeStyle™ 293-F	X-ray crystallography (hLeptin:hLEP-R_{CRH2} assembly), SEC-MALS (Ext. Data Fig. 1f, 8a), SDS-PAGE (Ext. Data Fig. 1g), Cryo-EM (hLeptin:hLEP-$R_{ECD\text{-}tGCN4}$ assembly)
Mouse LEP-R_{IgCRH2} (328-633; C602S)	LMBP 13466	582_pCAGGS_ss_His_TEV_mIgCHR2*	FreeStyle™ 293-F	X-ray crystallography (mLeptin:mLEP-R_{IgCRH2} assembly), SEC-MALS (Ext. Data Fig. 1f)
Mouse Leptin wt (21-167)	LMBP 13467	681_pET11d_mLeptin	*E. coli* (refolding)	X-ray crystallography (mLeptin:mLEP-R_{IgCRH2} assembly), SEC-MALS (Ext. Data Fig. 3b,d,g,h), BLI (Ext. Data Fig. 1c), Cryo-EM (mLeptin:mLEP-$RECD_{\text{-}\Delta FNII\text{-}tGCN4}$ assembly; for initial templates in Ext. Data Fig. 8b)
Human LEP-R_{IgCRH2} (330-635; C604S)	LMBP 13468	581_pCAGGS_ss_His_TEV_hIgCHR2*	FreeStyle™ 293-F	SEC-MALS (Ext. Data Fig. 1f), SDS-PAGE (Ext. Data Fig. 1g)
Mouse Leptin wt (22-167)	LMBP 13469	774_pET15b_His_TEV_mLEP_WT	*E. coli* (refolding)	Cryo-EM and SAXS (mLeptin:mLEP-R_{ECD} and mLeptin:mLEP-$R_{ECD\text{-}tGCN4}$ assemblies), SEC-MALS (Fig. 3a, Ext. Data Fig. 1b, Ext. Data Fig. 3d,e,i, Ext. Data Fig. 5a), AUC (Fig. 3b-c, Ext. Data Fig. 3a), Signaling (Fig. 3d, Ext. Data Fig. 3k)
Mouse LEP-R_{CRH2} (426-633; C602S)	LMBP 13470	569_pCAGGS_ss_HIS_TEV_mCHR2*	FreeStyle™ 293-F	BLI (Ext. Data Fig. 1c)
Mouse LEP-R_{ECD} (22-839)	LMBP 13471	635_pCAGGS_ss_HIS_Caspase3site_mLepR	FreeStyle™ 293-F	BLI (Ext. Data Fig. 1c), AUC (Fig. 3b-c, Ext. Data Fig. 3a), SEC-MALS (Fig. 2a, Ext. Data Fig. 6b,d,h,i), MS Disulfide mapping (Ext. Data Fig. 7b), Cryo-EM and SAXS (mLEP-R_{ECD} and mLeptin:mLEP-R_{ECD} assembly)
Human $Leptin_{a1}$ (22-167; S141A/T142A)	LMBP 13472	598_pTwist_ss_His_TEV_hLEPa1	FreeStyle™ 293-F	SEC-MALS (Ext. Data Fig. 1f)
Mouse $Leptin_{a1}$ (22-167; S141A/T142A)	LMBP 13473	775_pET15b_His_TEV_mLEPa1_S141A-T142A	*E. coli* (refolding)	SEC-MALS (Fig. 3a), Signaling (Fig. 3d)
Mouse $Leptin_{a2}$ (22-167; ^{60}LDFI^{63}/AAAA)	LMBP 13474	776_pET15b_His_TEV_mLEPa2_LDFI/AAAA	*E. coli* (refolding)	SEC-MALS (Fig. 3a), AUC (Fig. 3b), Signaling (Fig. 3d)
Mouse Leptin site I variant (22-167; Q155A/D156A/Q159A)	LMBP 13475	777_pET15b_His_TEV_mLEPsiteI Q155A/D156A/Q159A	*E. coli* (refolding)	SEC-MALS (Fig. 3a), Signaling (Fig. 3d)
Human Leptin wt (22-167)	LMBP 13476	787_pET15b_His_TEV_hLEP_WT	*E. coli* (refolding)	Signaling (Fig. 3d, Ext. Data Fig. 3k)
Mouse LEP-Rb (22-1162)	LMBP 13477	708_pSems_ss_ALFAtag_HAtag_3xGGS_mLEP-Rb	HEK293T	Signaling (Fig. 3d), smTIRFM

Mouse LEP-$R_{ECD\text{-}A407E}$ (22-839; A407E)	LMBP 13478	739_pCAGGS_ss_HIS_Caspase3site_mLepR_A407E	FreeStyle™ 293-F	SEC-MALS (Ext. Data Fig. 3b)
Mouse LEP-$R_{ECD\text{-}\Delta FNIII}$ (22-633; C602S)	LMBP 13479	632_pCAGGS_ss_HIS_Caspase3site_mIgCHR1IgCHR2*	FreeStyle™ 293-F	SEC-MALS (Ext. Data Fig. 3c,e)
Human LEP-R_{ECD} (22-839)	LMBP 13480	611_pCAGGS_ss_HIS_Caspase3site_hLepR	FreeStyle™ 293-F	SEC-MALS (Ext. Data Fig. 3f,g,j)
Mibavademab Heavy Chain	LMBP 13481	797_pTwist_ss_11510H_mibavademab	FreeStyle™ 293-F	SEC-MALS (Ext. Data Fig. 3j), Signaling (Ext. Data Fig. 3k)
Mibavademab Light Chain	LMBP 13482	798_pTwist_ss_11510L_mibavademab	FreeStyle™ 293-F	SEC-MALS (Ext. Data Fig. 3j), Signaling (Ext. Data Fig. 3k)
Human Leptin wt (22-167)	LMBP 13483	725_pET20b_ss_His_Caspase3site_hLEP	*E. coli* (secreted)	SEC-MALS (Ext. Data Fig. 3f,g,h)
“Murinized” Human Leptin (22-167; G139L)	LMBP 13484	786_pET15b_His_TEV_hLEP_G139L	*E. coli* (refolding)	SEC-MALS (Ext. Data Fig. 3i)
"Murinized" Human Leptin (22-167; G139L/I85V/M68L/G132D)	LMBP 13485	800_pET15b_His_TEV_hLEP_G139L/I85V/M68L/G132D	*E. coli* (refolding)	SEC-MALS (Ext. Data Fig. 3i)
"Murinized" Human Leptin mCD-loop (22-167; H118S/W121Q/A122T/E126Q/T127K/ L128P/D129E)	LMBP 13486	801_pET15b_His_TEV_hLEP_mCDloop	*E. coli* (refolding)	SEC-MALS (Ext. Data Fig. 3i)
Human LEP-Rb (22-1165)	LMBP 13487	707_pSems_ss_ALFAtag_HAtag_3xGGS_hLEP-Rb	HEK293T	Signaling (Ext. Data Fig. 3k)
Human $Leptin_{a1}$ (22-167; S141A/T142A)	LMBP 13488	788_pET15b_His_TEV_hLEP_S141-T142A	*E. coli* (refolding)	Signaling (Ext. Data Fig. 3k)
Human $Leptin_{a2}$ (22-167; ^{60}LDFI^{63}/AAAA)	LMBP 13489	789_pET15b_His_TEV_hLEP_60AAAA63	*E. coli* (refolding)	Signaling (Ext. Data Fig. 3k)
Human Leptin site I variant (22-167; Q155A/D156A/W159A)	LMBP 13490	793_pET15b_His_TEV_hLEPsiteI_Q155A_D156A_W159A	*E. coli* (refolding)	Signaling (Ext. Data Fig. 3k)
Mouse LEP-$R_{ECD\text{-}tGCN4}$ (22-839)	LMBP 13491	715_pTwist_ss_mLEP-R_5xGGS_tGCN4	FreeStyle™ 293-F	Cryo-EM and SAXS (mLeptin:mLEP-$R_{ECD\text{-}tGCN4}$ assembly), SEC-MALS (Ext. Data Fig. 5a)
Human LEP-$R_{ECD\text{-}tGCN4}$ (22-839)	LMBP 13492	713_pTwist_ss_hLEP-R_5xGGS_tGCN4	FreeStyle™ 293-F	Cryo-EM (hLeptin:hLEP-$R_{ECD\text{-}tGCN4}$ assembly), SEC-MALS (Ext. Data Fig. 8a)
Mouse LEP-$R_{ECD\text{-}\Delta FNIII\text{-}tGCN4}$ (22-633; C602S)	LMBP 13493	726_pCAGGS_ss_HIS_Caspase3site_mIgCHR1IgCHR2*_ 5xGGS_tGCN4	FreeStyle™ 293-F	Cryo-EM (mLeptin:mLEP-$R_{ECD\text{-}\Delta FNII\text{-}tGCN4}$ assembly; for initial templates in Ext. Data Fig. 8b)
mLEP-R_{FNIII}	LMBP 13673	863_pHLsec_mLEPR-FNIII-N668Q N726Q	HEK293S MGAT1$^{-/-}$	X-ray crystallography (LEP-R_{FNIII}:VHH4.80)
Nanobody VHH4.80	LMBP 13674	834_pHLsec_anti-mLEP-R-VHH-4.80-His	HEK293S MGAT1$^{-/-}$	X-ray crystallography (LEP-R_{FNIII}:VHH4.80)
mLEP-$R_{\text{-}mXFP}$ (22-860)	LMBP 13679	pSems-leader-mXFP-mLEP-R (22-860)	HeLa	smTIRFM
mLEP-Rb_{ALFA} (22-1165)	LMBP 13477	708_pSems-leader-ALFAtag-mLEP-Rb	HeLa	smTIRFM
mLEP-Ra_{ALFA} (22-896)	LMBP 13678	858_pSems-leader-ALFAtag-mLEP-Ra	HeLa	smTIRFM
mLEP-R (22-866)-3xGGS-$Foldon_{ALFA}$	LMBP 13676	856_pSems-leader-ALFAtag-mLEP-R (22-866)-3xGGS-Foldon	HeLa	smTIRFM
mLEP-$R_{\text{-}ALFA}$ (22-866)	LMBP 13675	856_pSems-leader-ALFAtag-mLEP-R (22-866)-3xGGS-Foldon	HeLa	smTIRFM
$hTpoR_{ALFA}$	LMBP 13680	pSems-leader-ALFAtag-hTpoR	HeLa	smTIRFM

Supplementary references

1 Peelman, F., Zabeau, L., Moharana, K., Savvides, S. N. & Tavernier, J. 20 years of leptin: insights into signaling assemblies of the leptin receptor. *The Journal of endocrinology* **223**, T9-23, doi:10.1530/JOE-14-0264 (2014).

2 Niv-Spector, L. *et al.* Identification of the hydrophobic strand in the A-B loop of leptin as major binding site III: implications for large-scale preparation of potent recombinant human and ovine leptin antagonists. *The Biochemical journal* **391**, 221-230, doi:10.1042/BJ20050457 (2005).

3 Peelman, F. *et al.* Mapping of the leptin binding sites and design of a leptin antagonist. *The Journal of biological chemistry* **279**, 41038-41046, doi:10.1074/jbc.M404962200 (2004).

4 Boulanger, M. J., Chow, D. C., Brevnova, E. E. & Garcia, K. C. Hexameric structure and assembly of the interleukin-6/IL-6 alpha-receptor/gp130 complex. *Science (New York, N.Y.)* **300**, 2101-2104, doi:10.1126/science.1083901 (2003).

5 Tamada, T. *et al.* Homodimeric cross-over structure of the human granulocyte colony-stimulating factor (GCSF) receptor signaling complex. *Proceedings of the National Academy of Sciences of the United States of America* **103**, 3135-3140, doi:10.1073/pnas.0511264103 (2006).

6 Evans, R. *et al.* Protein complex prediction with AlphaFold-Multimer. *bioRxiv, preprint* doi:10.1101/2021.10.04.463034 (2022).

7 Mirdita, M. *et al.* ColabFold: making protein folding accessible to all. *Nature methods* **19**, 679-682, doi:10.1038/s41592-022-01488-1 (2022).

8 Amemiya, C. T. *et al.* The African coelacanth genome provides insights into tetrapod evolution. *Nature* **496**, 311-316, doi:10.1038/nature12027 (2013).

9 Londraville, R. L., Prokop, J. W., Duff, R. J., Liu, Q. & Tuttle, M. On the Molecular Evolution of Leptin, Leptin Receptor, and Endospanin. *Frontiers in endocrinology* **8**, 58, doi:10.3389/fendo.2017.00058 (2017).

10 Gromada, J. S., P.; Altarejos, J.; Murphy, A. J. A leptin receptor agonist antibody for use in treating a metabolic dysfunction or hypoleptinemia. (2019).

11 Moharana, K. *et al.* Structural and mechanistic paradigm of leptin receptor activation revealed by complexes with wild-type and antagonist leptins. *Structure (London, England : 1993)* **22**, 866-877, doi:10.1016/j.str.2014.04.012 (2014).

12 Zabeau, L. *et al.* Leptin receptor activation depends on critical cysteine residues in its fibronectin type III subdomains. *The Journal of biological chemistry* **280**, 22632-22640, doi:10.1074/jbc.M413308200 (2005).

13 Voigtmann, F. *et al.* Identification of a novel leptin receptor (LEPR) variant and proof of functional relevance directing treatment decisions in patients with morbid obesity. *Metabolism: clinical and experimental* **116**, 154438, doi:10.1016/j.metabol.2020.154438 (2021).

14 Kimber, W. *et al.* Functional characterization of naturally occurring pathogenic mutations in the human leptin receptor. *Endocrinology* **149**, 6043-6052, doi:10.1210/en.2008-0544 (2008).

15 Haglund, E. *et al.* Uncovering the molecular mechanisms behind disease-associated leptin variants. *The Journal of biological chemistry* **293**, 12919-12933, doi:10.1074/jbc.RA118.003957 (2018).

16 Koerber-Rosso, I. *et al.* A fresh look to the phenotype in mono-allelic likely pathogenic variants of the leptin and the leptin receptor gene. *Molecular and cellular pediatrics* **8**, 10, doi:10.1186/s40348-021-00119-7 (2021).

17 Salum, K. C. R. *et al.* When Leptin Is Not There: A Review of What Nonsyndromic Monogenic Obesity Cases Tell Us and the Benefits of Exogenous Leptin. *Frontiers in endocrinology* **12**, 722441, doi:10.3389/fendo.2021.722441 (2021).
18 Ng, P. C. & Henikoff, S. SIFT: Predicting amino acid changes that affect protein function. *Nucleic acids research* **31**, 3812-3814, doi:10.1093/nar/gkg509 (2003).
19 Echwald, S. M. *et al.* Identification of two novel missense mutations in the human OB gene. *International journal of obesity and related metabolic disorders : journal of the International Association for the Study of Obesity* **21**, 321-326, doi:10.1038/sj.ijo.0800408 (1997).
20 Nordang, G. B. N. *et al.* Next-generation sequencing of the monogenic obesity genes LEP, LEPR, MC4R, PCSK1 and POMC in a Norwegian cohort of patients with morbid obesity and normal weight controls. *Molecular genetics and metabolism* **121**, 51-56, doi:10.1016/j.ymgme.2017.03.007 (2017).
21 Wabitsch, M. *et al.* Biologically inactive leptin and early-onset extreme obesity. *The New England journal of medicine* **372**, 48-54, doi:10.1056/NEJMoa1406653 (2015).
22 Wabitsch, M. *et al.* Measurement of immunofunctional leptin to detect and monitor patients with functional leptin deficiency. *European journal of endocrinology* **176**, 315-322, doi:10.1530/EJE-16-0821 (2017).
23 Mazen, I., El-Gammal, M., Abdel-Hamid, M. & Amr, K. A novel homozygous missense mutation of the leptin gene (N103K) in an obese Egyptian patient. *Molecular genetics and metabolism* **97**, 305-308, doi:10.1016/j.ymgme.2009.04.002 (2009).
24 Zhao, Y. *et al.* A novel mutation in leptin gene is associated with severe obesity in Chinese individuals. *BioMed research international* **2014**, 912052, doi:10.1155/2014/912052 (2014).
25 Chekhranova, M. K., Karpova, S. K., Iatsyshina, S. B. & Pankov Iu, A. [A new mutation c.422C>G (p.S141C) in homo- and heterozygous forms of the human leptin gene]. *Bioorganicheskaia khimiia* **34**, 854-856, doi:10.1134/s1068162008060198 (2008).
26 Hong, C. J. *et al.* ENU mutagenesis identifies mice with morbid obesity and severe hyperinsulinemia caused by a novel mutation in leptin. *PloS one* **5**, e15333, doi:10.1371/journal.pone.0015333 (2010).
27 Akinci, A. *et al.* Novel Mutations in Obesity-related Genes in Turkish Children with Non-syndromic Early Onset Severe Obesity: A Multicentre Study. *Journal of clinical research in pediatric endocrinology* **11**, 341-349, doi:10.4274/jcrpe.galenos.2019.2019.0021 (2019).
28 Mazen, I., El-Gammal, M., Abdel-Hamid, M., Farooqi, I. S. & Amr, K. Homozygosity for a novel missense mutation in the leptin receptor gene (P316T) in two Egyptian cousins with severe early onset obesity. *Molecular genetics and metabolism* **102**, 461-464, doi:10.1016/j.ymgme.2010.12.013 (2011).
29 Farooqi, I. S. *et al.* Clinical and molecular genetic spectrum of congenital deficiency of the leptin receptor. *The New England journal of medicine* **356**, 237-247, doi:10.1056/NEJMoa063988 (2007).
30 Saeed, S. *et al.* Genetic variants in LEP, LEPR, and MC4R explain 30% of severe obesity in children from a consanguineous population. *Obesity (Silver Spring, Md.)* **23**, 1687-1695, doi:10.1002/oby.21142 (2015).
31 Huvenne, H. *et al.* Seven novel deleterious LEPR mutations found in early-onset obesity: a DeltaExon6-8 shared by subjects from Reunion Island, France, suggests a founder effect. *The Journal of clinical endocrinology and metabolism* **100**, E757-766, doi:10.1210/jc.2015-1036 (2015).

32 Branson, R. *et al.* Binge eating as a major phenotype of melanocortin 4 receptor gene mutations. *The New England journal of medicine* **348**, 1096-1103, doi:10.1056/NEJMoa021971 (2003).
33 Niv-Spector, L. *et al.* Mapping leptin-interacting sites in recombinant leptin-binding domain (LBD) subcloned from chicken leptin receptor. *The Biochemical journal* **390**, 475-484, doi:10.1042/BJ20050233 (2005).
34 Carpenter, B. *et al.* Structure of the human obesity receptor leptin-binding domain reveals the mechanism of leptin antagonism by a monoclonal antibody. *Structure (London, England : 1993)* **20**, 487-497, doi:10.1016/j.str.2012.01.019 (2012).